Master Thesis in Geographical Information Science nr 162

Usability of Sentinel-1 C-band VV and VH SAR data for the detection of flooded oil palm

Image credit: Hai *et al.* (2001)

Sarah Sienaert

2023
Department of
Physical Geography and Ecosystem Science
Lund University
Sölvegatan 12
S-223 62 Lund
Sweden

Sarah Sienaert (2023). Usability of Sentinel-1 C-band VV and VH SAR data for the detection of flooded oil palm.

Master degree thesis, 30 credits in Geographical Information Science

Department of Physical Geography and Ecosystem Science, Lund University

Usability of Sentinel-1 C-band VV and VH SAR data for the detection of flooded oil palm

Sarah Sienaert

Master degree thesis, 30 credits in Geographical Information Science

Principal Supervisor:

Iris van Duren

ITC, Faculty of Geo-Information Science and Earth Observation,

University of Twente

Co-supervisor:

David Tenenbaum

Department of Physical Geography and Ecosystem Science, Lund University

ACKNOWLEDGEMENTS

To Iris van Duren: This thesis was markedly improved by the wisdom and guidance you shared with me. Thank you for the patience and flexibility you demonstrated from its inception to its completion.

To David Tenenbaum and Louise van Leeuwen: Thank you for the advice and support you gave so generously throughout the degree.

To Yousif Ali Hussin: Thank you for sharing your technical expertise in radar remote sensing, your insights were invaluable.

To my family and especially my husband, Alex: thank you for your tireless support and encouragement. This accomplishment is your accomplishment.

ABSTRACT

Flooding in oil palm plantations in Southeast Asia is a common problem. The oil palm's habitable range is restricted to lowland equatorial areas, and the high rainfall and degraded landscapes associated with oil palm cultivation leaves oil palm prone to inundation. Waterlogged roots can diminish yields and increase palm mortality leading to significant financial losses for the oil palm industry. Oil palm expansion is associated with environmental degradation and high carbon emissions; when expansion occurs in flood-prone areas a high environmental cost is paid for little or no economic gain. Climate change is expected to bring about more variable and extreme rainfall events with more frequent flooding in Southeast Asia, therefore the problem of inundation in oil palm plantations is set to worsen.

Few studies have applied remote sensing technology to the problem of inundation in oil palm plantations. To the best of the author's knowledge, this is the first study to report the backscatter characteristics of flooded oil palm. In addition, this study aims to contribute to the under-developed research areas of mapping smallholder management systems and young oil palm.

This study tested the ability of Sentinel-1 C-band VV and VH data to detect the presence/absence of flooding in oil palm stands of all growth stages in a study area in Jambi Province, Indonesia. Smallholdings were the predominant production system although industrial holdings were also present. Classes were defined to represent the growth stages of oil palm in flooded and non-flooded conditions, and the backscatter characteristics and separability of the classes were determined.

C-band successfully detected the presence of flooding in very young oil palm, but not in older oil palm. As the canopy began to close, the C-band signal reached a saturation point so that the backscatter profiles of older oil palm in flooded and non-flooded conditions were indistinguishable. Even in very young oil palm, where C-band was successful in detecting flooding, overlap existed in the backscatter responses in flooded and non-flooded conditions due to residual speckle noise in the data and a wide spread in the backscatter values caused by a complex backscatter return from the target. A less complex study setting may permit a more effective reduction of residual speckle noise, which would improve C-band's ability to identify flooding in open canopy oil palm.

TABLE OF CONTENTS

LIST OF ABBREVIATIONS

BMKG	*Badan Meteorologi, Klimatologi, dan Geofisika* (Meteorological, Climatological, and Geophysical Agency of Indonesia)
BNPB	*Badan Nasional Penanggulangan Bencana* (Indonesia's National Board for Disaster Management)
CRR	Chain Reaction Research
DEM	Digital Elevation Model
DJP	*Direktorat Jenderal Perkebunan* (Directorate General of Estate Crops)
ESA	European Space Agency
ESRI	Environmental Systems Research Institute
GIS	Geographic Information System
GRDH	Ground Range Detected High Resolution
HH	Horizontal transmit, horizontal receive
HV	Horizontal transmit, vertical receive
IW	Interferometric Wide
KML	Keyhole Markup Language
NDI	Normalised Difference Image
NISAR	NASA/Indian Space Research Organization SAR
RSPO	Roundtable on Sustainable Palm Oil
RUS	Research and User Support
S1TBX	Sentinel-1 Toolbox
SAR	Synthetic Aperture Radar
SKMJ	*Stasiun Klimatologi Muaro Jambi* (weather station in Jambi Province)
SMST	*Stasiun Meteorologi Sultan Thaha* (weather station in Jambi Province)
SNAP	Sentinel Application Platform
SRTM	Shuttle Radar Topography Mission
SWIR	Shortwave Infrared
TIFF	Tag Image File Format
USGS	U.S. Geological Survey
VH	Vertical transmit, horizontal receive
VV	Vertical transmit, vertical receive
WGS	World Geodetic System

LIST OF TABLES

LIST OF FIGURES

1. INTRODUCTION

The oil palm (*Elaeis guineensis*) provides the world's cheapest and highest-yielding vegetable oil (Vijay et al., 2016). Demand for palm oil and its derivatives as edible oil, biofuel, and ingredients in personal care products, cosmetics, and cleaning products has led to the rampant expansion of oil palm in the tropics (Phalan et al., 2013; Vijay et al., 2016). Today, annual global production of palm oil is 77 million tonnes (USDA, 2022) and it is expected to reach 120–156 million tonnes by 2050 (Corley, 2009). Indonesia and Malaysia are responsible for 59% and 25% of global palm oil production, respectively (USDA, 2022), and have planted areas of 16.24 Mha (Gaveau et al., 2022) and 5.9 Mha (MPOC, 2020), respectively. Another 12–19 Mha of oil palm is expected to be planted globally by 2050 (Pohl et al., 2015; Mohd Najib et al., 2020).

The oil palm's habitable range is restricted to lowland equatorial areas, which are home to forest ecosystems of considerable value for their endemism, biodiversity, carbon storage, and provision of ecosystem services (Abram et al., 2014; Vijay et al., 2016). More than half of Indonesia's cultivated area in oil palm has replaced forests (Koh & Wilcove, 2008; Vijay et al., 2016). Of the forest that was lost in Indonesia between 2000 and 2019, 32% (3.09 Mha) was ultimately replaced by oil palm (Gaveau et al., 2022).

1.1. Flooding in oil palm plantations

The degraded landscapes associated with oil palm cultivation coupled with the high rainfall common to the oil palm's habitable range pose a major flood risk to oil palm plantations (Chong et al., 2017). Surface waterlogging and localised flooding in oil palm plantations in Southeast Asia is a common occurrence (Hai et al., 2001; Lee & Ong, 2006; Marti, 2008; Ahamad et al., 2011; USDA, 2015; Tarigan, 2016; Woittiez et al., 2017; Merten et al., 2020, Abubakar et al., 2021). Many oil palm plantations, especially those on flatter terrain, have experienced prolonged saturation at the end of the rainy season, with water extending across hundreds of acres and to a depth of a few meters (Lee & Ong, 2006). Inundation can persist from several days to more than a few months (Lee & Ong, 2006; Woittiez et al., 2017).

The optimal water table depth for oil palm cultivation is 0.60–0.75 m below the land surface (Mantel et al., 2007). Oil palm can tolerate periods of saturation less than two weeks in duration so long as the water is oxygen-rich and not stagnant (Mantel et al., 2007). Ideally, drainage systems should not allow saturated conditions in oil palm stands to exceed three days (Mantel et al., 2007) as the impaired respiratory function of waterlogged roots diminishes physiological processes and productivity (Woittiez et al., 2017). Inundation can cause death in juvenile palms and reduced yields in mature palms (Henson et al., 2008).

Furthermore, flood events hinder operational processes by impeding access to oil palm stands and severely compromising maintenance activities (e.g., fertilisation), harvesting schedules, and the transportation of produce (Merten et al., 2020; Yamamoto et al., 2021).

Flood events have caused substantial financial losses for the oil palm industry (Abram et al., 2014). For example, floods in the Lower Kinabatangan floodplains of Sabah, Malaysia, in 1996 and 2000 caused the mortality of 1,900 ha and 5,000 ha of young oil palm, respectively, and an economic loss of MYR 4.4 million and MYR 10 million, respectively (Hai et al., 2001). In December 2014, heavy rainfall in Peninsular West Malaysia caused lowland flooding in 184,000 ha of oil palm (USDA, 2015). This reduced palm oil production by 230,000 tonnes compared to December 2013 and continued to suppress production in 2015 (USDA, 2015). More intense monsoon rainfall and more frequent flooding events caused by climate change in Southeast Asia (Hijoka et al., 2014; Loo et al., 2015; Heitmann et al., 2017; Kelley & Prabowo, 2019; Abubakar et al., 2021) are likely to exacerbate the problem. Plantations cease to be economically viable even at the stage of impaired drainage, thus oil palm companies may abandon plantations well before they reach a flooded stage (Sumarga et al., 2016; Abubakar et al., 2021).

Multiple factors contribute to an increased risk of flooding in oil palm environments (Merten et al., 2020). Oil palm plantations are associated with severe soil degradation and erosion (Guilliame et al., 2015, 2016), which can cause low soil water infiltration rates (Tarigan et al., 2018; Merten et al., 2020). This, coupled with the low evapotranspiration rates that are characteristic of young oil palms, may increase

surface run-off (Tarigan et al., 2018; Merten et al., 2020). Meanwhile, the flow of soil into rivers reduces the depth of riverbeds, while the land use conversion of upland areas to rubber and oil palm increases the streamflow (Merten et al., 2020).

Furthermore, oil palm expansion increasingly occurs at the expense of peatlands (Miettinen et al., 2012a, 2012b; Carlson et al., 2013; Pittman et al., 2013; Sumarga et al., 2016). Indonesia is estimated to have between 14.9 Mha and 20.9 Mha of peatland (the wide range of this estimate is primarily due to a lack of reliable data on the extent of peatland in Papua province) (Warren et al., 2017). Furthermore, Warren et al. (2017) estimate that Indonesia's peatland contains 30% more carbon than the country's entire forest biomass. An estimated 2.0–2.5 Mha of peatland has been converted to oil palm in Indonesia (Page et al., 2011; Miettinen et al., 2016; Osaki et al., 2016). However, oil palm concessions encompass a much larger area (6.63 Mha) of peatland, much of which is unplanted or degraded (RSPO, 2017; CRR, 2021). According to the most conservative estimate of Miettinen et al. (2012a), 6 Mha of Indonesia's peatland will be converted to oil palm by 2030.

Indonesia's peatland largely resides less than 20 m above sea level (Page et al., 2011). Due to its very high (90%) water content, peatland is drained for oil palm cultivation, causing it to subside by 1.0–1.5 m following drainage (Sumarga et al., 2016). This subsidence continues by a further 3–5 cm/year (Sumarga et al., 2016) and increasingly prolongs the inundation period (Merten et al., 2020). Soil compaction (e.g., through heavy machinery use) also lowers the surface and reduces the infiltration rate, leading to increased surface runoff and reduced groundwater recharge (Hooijer et al., 2015; Dislich et al., 2017; Merten et al., 2020).

Fire is the traditional means of clearing land in Indonesia and, despite laws prohibiting its use in land clearance, its use persists (Pittman et al., 2013; Dislich et al., 2017; Noojipady et al., 2017; Adrianto et al., 2020; Edwards et al., 2020). Drained peatland, and especially fire-degraded peatland, is closely linked to surface flooding (Page et al., 2009). In fact, some fire-degraded peatland in Indonesia is subject to near year-round flooding (Wösten et al., 2006b). The susceptibility to flooding of fire-degraded peatland is a result of several factors: the low transpiration rate of cleared land, which leads to deeper and longer-lasting surface water during the rainy season; the oxidation and

combustion of peat, which lowers the peat surface (subsidence); and the diminished water storage capacity of burnt peat (Page et al., 2009; Merten et al., 2020).

In addition to flood-susceptible peatlands, oil palm cultivation extends into wetlands and riverine floodplains of tropical lowland forests (Abram et al., 2014; Kelley & Prabowo, 2019; Merten et al., 2020). Junk et al. (1989, p. 112) define floodplains as "areas that are periodically inundated by the lateral overflow of rivers or lakes, and/or by direct precipitation or groundwater". In riverine floodplains of Southeast Asia, the inundation may be daily and tidal, such as in mangrove forests, or annual, where forests are seasonally flooded during the rainy season (Abram et al., 2014). Although the regular lateral exchange of water between rivers and wetlands or rivers and floodplains may abate flood events, the degradation of the soil's physical properties by oil palm cultivation means the expansion of plantations into wetlands and floodplains can disrupt their ecohydrological functioning (Merten et al., 2020).

Several studies (e.g., Jelsma et al., 2017; Kelley & Prabowo, 2019; Schoneveld et al., 2019; Merten et al., 2020) report that it is private companies, political elites, external investors, and more affluent farmers who are especially likely to cultivate floodplains, wetlands, and peatlands as they can support more industrialised land management operations (Merten et al., 2020). Flood events have spurred smallholders, who used to cultivate riparian zones for food crops or for oil palm, to sell or lease their land to commercial parties (Kelley & Prabowo, 2019; Merten et al., 2020).

In Indonesia, approximately 40% (6.08 Mha) of the cultivated area in oil palm is under smallholder production (DJP, 2021) and this is expected to increase to 60% by 2030 (Saragih, 2017). The Roundtable on Sustainable Palm Oil (RSPO) define smallholders as "farmers who grow oil palm, alongside with subsistence crops, where the family provides the majority of labour and the farm provides the principal source of income, and the planted oil palm area is less than 50 hectares" (RSPO, 2018).

For many independent smallholders, yields are diminished by the inability to implement proper drainage systems to prevent waterlogging, particularly in peatland areas (Woittiez et al., 2017). Although the RSPO has an Independent Smallholder Standard (RSPO, 2019), smallholders are subject to fewer regulations, are challenging

to capture in traceability systems, and are frequently lacking the capacity or incentives to comply with sustainability norms (Schoneveld et al., 2019). This is in contrast to commercial plantations, which increasingly comply with international sustainability standards (Schoneveld et al., 2019). With competition for land in non-peat soils and non-forested areas high among commercial plantations, smallholders are increasingly pushed into ecologically sensitive landscapes (Schoneveld et al., 2019).

Flood control measures (e.g., drainage channels, levees, pumping stations, retention basins) can be implemented in oil palm areas that are prone to waterlogging and flooding (Sumarga et al., 2016), but they are complex, extremely costly, and often ineffective (Hai et al., 2001; Lee & Ong, 2006; Abram et al., 2014; Sumarga et al., 2016). In peatland, where flood control measures are especially necessary (Jelsma et al., 2017), an extensive network of dykes is required (Sumarga et al., 2016). The dykes are prone to subsidence and, in prolonged dry spells, to cracking, necessitating a continuous and expensive maintenance program (Sumarga et al., 2016). Pumping is an inefficient method of flood control, but it may be used to remove excess water once low surface gradients impede gravity drainage (Sumarga et al., 2016). Yet the cost of pumping often proves prohibitive when compared to the revenue generated from oil palm production (Sumarga et al., 2016).

Moreover, the establishment of drainage or flood control infrastructure can redistribute floodwaters at a local level, giving rise to new social conflicts (Merten et al., 2020). Water infrastructure introduced by oil palm companies in wetland areas to reduce the impact of flooding on their plantations has been blamed for worsening the duration and depth of flooding on smallholder plantations situated adjacent to or downstream of the infrastructure (Merten et al., 2020). This leads to an inequitable distribution of flood damages in oil palm settings (Merten et al., 2020).

Palm oil yields have been stagnant for several years and to meet production demands the oil palm industry has focused on the expansion of planted area (USDA, 2012; Murphy, 2014; Pirker et al., 2016; Woittiez et al., 2017), but the expansion has largely occurred in marginal areas, such as peatlands, riparian zones, and degraded soils (Guilliame et al., 2016). For example, in contrast to Sumatra, Borneo still possesses abundant land available for oil palm development, however the primary source of new land for oil

palm cultivation is peatland (Schoneveld et al., 2019). As land in Indonesia becomes increasingly scarce, the expansion of oil palm into marginal areas risks exacerbating environmental and social problems (Noor et al., 2017; Schoneveld et al., 2019). Furthermore, the remaining tropical forest that resides in high altitude areas is under increasing pressure as warming temperatures in high elevation areas expand the suitable area for oil palm cultivation and lowland areas suffer an increase in flood risk (Yamamoto et al., 2021).

The accurate detection of flooding in both industrial holdings and smallholdings of oil palm is necessary to build an understanding of the extent, frequency, and severity of flooding in oil palm plantations, which has important implications for spatial planning, land management practices, and policy in the oil palm sector. Under-productive stands that are taken out of production have the potential to undergo rehabilitation to restore the ecosystem, social, and/or economic functions of the peatland and forest landscapes that they replaced (Abram et al., 2014; Nawir et al., 2016; Dislich et al., 2017). In addition, managing the flood risk faced by existing oil palm plantations in lowland areas will help prevent future deforestation in upland areas (Yamamoto et al., 2021).

1.2. Remote sensing applications for flooding in oil palm plantations

The extraction of flooded vegetation for flood monitoring is still a novel field compared to the more common application of wetland monitoring (Tsyganskaya et al., 2018b). Compared to the detection of open flood waters, there is a dearth of research on flooded surfaces beneath vegetation (Tsyganskaya et al., 2018b; Shen et al., 2019). This obscures the true extent of flooding, which can have a significant impact on human lives, property, and agricultural productivity (Tsyganskaya et al., 2018b).

In a review of remote sensing applications in oil palm studies, Chong et al. (2017) call for remote sensing to play a role in addressing the flood risk faced by oil palm plantations. So far, the application of remote sensing technology in oil palm studies has largely focused on land cover classification, change detection, pest and disease detection, and the estimation of physical plantation parameters such as tree counts, stand age, above ground biomass, and yield (Chong et al., 2017). Studies have reported challenges in detecting smallholder stands (Koh et al., 2011; Gunarso et al.,

2013; Gutiérrez-Vélez & DeFries, 2013; Yayusman & Nagasawa, 2015; Lee et al., 2016; Miettinen et al., 2016; Torbick et al., 2016; Descals et al., 2019), newly-planted or immature (open-canopy) stands (Koh et al., 2011; Li et al., 2015; Miettinen et al., 2015, 2016; Lazecky et al., 2018; Descals et al., 2019), and degraded stands (Santos & Messina, 2008; Gutiérrez-Vélez & DeFries, 2013).

Smallholder, newly-planted, immature, and degraded stands contain heterogeneous ground cover, which may make them spectrally and structurally indistinct from other land cover types and inhibit their detection (Gutiérrez-Vélez & DeFries, 2013). Consequently, the extent of oil palm land cover is frequently under-estimated (Li et al., 2015; Miettinen et al., 2015; Mohd Najib et al., 2020). Moreover, the cycle of planting, growing, and clear-felling creates a continually evolving patch work of plantations of different ages (Rosenqvist, 1996). It is important that oil palm mapping captures these intermediate growth stages (Rosenqvist, 1996). Several studies (e.g., Gutiérrez-Vélez & DeFries, 2013; Yayusman & Nagasawa, 2015; Lee et al., 2016) have named the reliable detection of immature and smallholder oil palm as an important objective for future research.

Very few studies have applied remote sensing technology to study inundation in oil palm stands, with those that have focusing on the development of hydrological models (Wösten et al., 2006a) and spatial and economic analyses (Abram et al., 2014; Sumarga et al., 2016). To the best of the author's knowledge, only one study (Yamamoto et al., 2021) has attempted to use remote sensing technology to identify inundation in an oil palm environment.

Yamamoto et al. (2021) assessed the flooding vulnerability of young (< 3 years old) and mature oil palm in the Batanghari River Basin in Indonesia by overlaying a maximum flood extent map with an oil palm distribution map. They surmised that oil palm classified as young in 2015 should be classified as mature in 2018 if it had avoided impaired growth due to flooding in the intervening period. The authors created a "during flood" image by compositing a series of wet season images derived from Sentinel-1 C-band synthetic aperture radar (SAR) data acquired between December 2016 and April 2017. They also created a "before flood" image by compositing a series of dry season images acquired in August 2016. They divided the

VV (vertical transmit, vertical receive) backscatter of the "during flood" image by the VV backscatter of the "before flood" image and used a threshold to define the flood extent. Cloud-free composites of Sentinel-2 data, combined with Sentinel-1 data, were used to create the distribution maps of young and mature oil palm in 2015 and 2018.

The authors reported that in the "during flood" image, young oil palm comprised 79% of the flooded oil palm. They also reported that just 6% of the flooded young oil palm 'survived' to 2018, in contrast to 52% of the flooded mature oil palm. However, the findings of the Yamamoto et al. study must be interpreted with caution. Although the 2015 oil palm distribution map was validated, the 2018 map was not. Therefore, the accuracy of the reported land use changes, including the changes in the proportion of young and mature oil palm between 2015 and 2018 is unknown. In addition, the flood extent was not validated, therefore the accuracy of the distribution and proportion of flooded and non-flooded oil palm is unknown. The limited penetration capability of the C-band signal in vegetation canopies means the flood extent map was derived primarily from the backscatter of open water surfaces and standing water underneath young oil palm. The true maximum extent of flooding in the study area is likely to cover a greater area and include a greater proportion of mature oil palm than was reported in the study.

To produce a map of flooded oil palm, Yamamoto et al. (2021) produced separate intermediate outputs of oil palm land cover and the presence of water then overlaid the outputs to produce a final map of flooded oil palm in their study area. They did not attempt to directly identify oil palm in flooded and non-flooded conditions. To the best of the author's knowledge, no studies have attempted to assess the ability of Sentinel-1 C-band VV and VH (vertical transmit, horizontal receive) data to detect the presence/absence of flooding in oil palm stands during an actual flood event.

1.2.1. SAR vs. optical approaches

The remote sensors used for oil palm mapping and monitoring primarily collect SAR data or optical data. Sensors of optical and SAR data collect different but complementary information. Optical sensors measure spectral reflectance between the visible and shortwave infrared (SWIR) domain of the electromagnetic spectrum, while

SAR sensors transmit microwave energy and receive the return signal as backscatter. The reflection of optical energy depends on the leaf structure, pigmentation, and moisture of the vegetation, while the backscatter of microwave energy depends on the size, density, orientation, and moisture content of the vegetation relative to the radar wavelength (Joshi et al., 2016).

Optical imagery possesses several disadvantages to SAR data for studying oil palm environments. Oil palm stands rapidly develop a closed canopy that is difficult to distinguish spectrally and structurally from other land cover types, especially forest and secondary vegetation (Santos & Messina, 2008; Gutiérrez-Vélez & DeFries, 2013; Tan et al., 2013; Miettinen et al., 2015; Mohd Najib et al., 2020; Xu et al., 2021). It is highly challenging to identify oil palm stands using optical imagery with a spatial resolution of 10–30 m; rather, very high (< 1 m) spatial resolution optical imagery is required (Miettinen & Liew, 2011; Miettinen et al., 2015). The quality of optical imagery is also affected by haze and smoke, which is a common occurrence in South-East Asia due to pollution caused in part by the oil palm industry burning plantation waste (Pohl et al., 2015; Pohl & Loong, 2016).

Optical sensors are unable to penetrate clouds, and the persistent cloud cover that is typical in the tropics makes the acquisition of cloud-free imagery in oil-palm growing areas highly challenging (Santos & Messina, 2008; Cheng et al., 2016; Torbick et al., 2016). In fact, it takes between one and seven years to obtain a cloud-free image (Pittman et al., 2013; Pohl & Loong, 2016). Persistent cloud cover is also characteristic of flood events (Martinis et al., 2017) and flood events may come and go without the acquisition of a single cloud-free optical image (Clement et al., 2017). In contrast, the active sensors of SAR systems can operate day and night and under all weather conditions (Plank et al., 2017).

The principal deficiency of optical sensors in studies of flooded vegetation is their inability to penetrate vegetation canopies, thus standing water underneath a canopy remains undetected (Pham-Duc et al., 2017; Tsyganskaya et al., 2018b). In contrast to optical systems, SAR systems use longer wavelengths of the electromagnetic spectrum, enabling them to penetrate clouds and vegetation canopies to detect a flooded land surface underneath (Tsyganskaya et al., 2018b).

In general, SAR systems comprising longer wavelengths (L-band [λ=23.6 cm] and P-band [λ=70 cm]) and co-polarised sensors (HH [horizontal transmit, horizontal receive] and VV) penetrate deeper into vegetation canopies than those comprising shorter wavelengths (C-band [λ=5.6 cm] and X-band [λ=3.1 cm]) and cross-polarised sensors (HV [horizontal transmit, vertical receive] and VH) (Tsyganskaya et al., 2018b). However, many factors determine the penetration depth of a SAR signal and a detailed overview of the scattering mechanisms observed in flooded vegetation is provided in Appendix A. In 2024, the European Space Agency (ESA) will launch "Biomass"—the first space-borne P-band SAR—which will enable even greater canopy penetration and flood-detection capabilities in forested areas.

There are several challenges associated with SAR image analysis and interpretation, especially in relation to flooded vegetation (Tsyganskaya et al., 2018b). Due to the side-looking nature of SAR systems, geometric distortions (radar shadow, overlaying, and foreshortening) can occur in hilly regions. The effect is exacerbated by steep terrain and small look angles, but it may be mitigated with geometric correction (Tsyganskaya et al., 2018b). Speckle is intrinsic to SAR imagery and it appears as a salt-and-pepper pattern (Singh & Shree, 2016). Speckle is noise caused by the random interference of the return signals generated from a multitude of ground scatterers (Lee et al., 1994; Singh & Shree, 2016). Speckle impedes image interpretation and reduces classification accuracy (Lee et al., 1994; Singh & Shree, 2016), but it may be suppressed with the application of filters. Furthermore, scattering mechanisms are determined by the characteristics of the sensor and the target, which adds complexity to the interpretation of SAR imagery.

Studies have demonstrated the ability of SAR data to distinguish oil palm from other land cover types using SAR backscatter (Rosenqvist, 1996; Miettinen & Liew, 2011; Morel et al., 2011; Li et al., 2015; Miettinen et al., 2015; Kee et al., 2018; Lazecky et al., 2018; Ballester-Berman & Rastoll-Gimenez, 2021), SAR backscatter and SAR texture information (Santos & Messina, 2008; Rakwatin et al., 2012; Laurin et al., 2013; Yayusman & Nagasawa, 2015; Torbick et al., 2016; Descals et al., 2019; Mohd Najib et al., 2020), or a combination of SAR data and optical data (comprising one or more of spectral characteristics, vegetation indices, and texture variables) (Santos & Messina, 2008; Koh et al., 2011; Gutiérrez-Vélez & DeFries, 2013; Laurin et al., 2013;

Tan et al., 2013; Yayusman & Nagasawa, 2015; Cheng et al., 2016; Torbick et al., 2016; De Alban et al., 2018; Descals et al., 2019; Nomura et al., 2019; Poortinga et al., 2019; Mohd Najib et al., 2020; Xu et al., 2021). Other applications of SAR data in oil palm environments include studies of stand age (Carolita et al., 2019), moisture content (soil and palm), aboveground biomass, and tree height (Pohl & Loong, 2016).

In a review of characteristics and approaches to detect flooded vegetation using SAR technology, the authors call for the development of approaches to detect flooded vegetation from "various and complex environments" (Tsyganskaya et al., 2018b, p. 2255). SAR sensors not only hold many advantages over optical sensors for the detection of flooded vegetation (Tsyganskaya et al., 2018b), but their use in the heterogeneous and complex environment of an oil palm plantation is significantly under-developed (Teng et al., 2015; Pohl et al., 2015; Pohl & Loong, 2016). According to Ballester-Berman and Rastoll-Gimenez (2021, p. 3) "further investigation must be carried out to understand C-band backscattering signatures from [oil palm] monoculture plantations".

The vegetation biomass (structure and density) that sits above ground or above water exerts a considerable effect on the scattering mechanisms of the SAR signal (Tsyganskaya et al., 2018b). In general, backscatter increases with increasing biomass until a saturation point is reached where the volume scattering from the canopy completely obscures the double bounce effect so that water underneath a canopy is no longer detected (Tsyganskaya et al., 2018b). Sensor characteristics and environmental conditions determine the point of saturation (Tsyganskaya et al., 2018b). (More detailed information on the influence of target characteristics on the scattering mechanisms of flooded vegetation is provided in Appendix A.)

The strong influence of biomass on backscatter, coupled with the under-representation of juvenile/open-canopy oil palm in remote sensing studies, means it is important to account for all the different growth stages of oil palm in a plantation so that the full extent of flooding in an oil palm stand may be determined.

Hitherto, Sentinel-1 has been the primary source of freely available SAR data, therefore Sentinel-1 C-band data is the focus of this study. Despite the relatively short wavelength

of C-band, it is hoped that the cavernous space underneath an oil palm canopy (Figure 1) facilitates the use of C-band data in studies of flooding in oil palm stands.

Image credit: https://commons.wikimedia.org/wiki/File:Oilpalm_malaysia.jpg

Figure 1: The 'hollow' space underneath an oil palm canopy.

1.3. Problem statement

Inundation in oil palm stands causes reduced yields in mature palms and mortality in young palms and interferes with operational processes. This reduces a plantation's economic viability and may lead to its abandonment. When this occurs, a high environmental price has been paid to cultivate oil palm for little or no economic gain. Improving our understanding of flood occurrences in oil palm plantations is essential for effective land use planning and conservation. This will inform decision-makers in the oil palm industry and policy-makers in government of the sensitivity of certain landscapes to oil palm cultivation so that the expansion of oil palm into flood-prone areas may be avoided and existing under-productive stands may be taken out of production and rehabilitated. SAR represents a valuable tool in flood assessments due

to its ability to see through the cloud cover that is associated with flood events. It can also penetrate vegetation canopies to detect standing water underneath a canopy. It is not yet known if Sentinel-1 C-band VV and VH data can detect the presence/absence of flooding in oil palm stands.

1.4. Objectives

The overall objective of this study is to examine the capability of Sentinel-1 C-band VV and VH SAR data to detect the presence/absence of flooding in oil palm. The specific objective is to determine the backscatter characteristics and separability of different growth stages of oil palm in flooded and non-flooded conditions.

1.5. Research questions

1. What are the backscatter characteristics of the different oil palm growth stages in flooded and non-flooded conditions in the VV and VH polarisations?

2. What is the separability of the backscatter profiles of the different oil palm growth stages in flooded and non-flooded conditions in the VV and VH polarisations?

3. To what extent does the backscatter of derived bands improve the separability of the backscatter profiles of the different oil palm growth stages in flooded and non-flooded conditions?

4. To what extent does a time series of standardised backscatter improve the separability of the backscatter profiles of the different growth stages in flooded and non-flooded conditions?

5. To what extent can Sentinel-1 C-band VV and VH data detect flooding in oil palm plantations?

2. DATA AND METHODS

2.1. Study area

In the absence of field data, very high spatial resolution optical data may be used as reference data. As a free and open source of very high spatial resolution optical data, Google Earth was used to perform a visual search for standing water in oil palm stands on the islands of Sumatra and Kalimantan, which are home to the major oil palm growing provinces in Indonesia.

A Google Earth image acquired on 26 November 2016 in a sub-area of Jambi Province on Sumatra Island was selected for the study area based on the following criteria: 1) the visible presence of general flooding (e.g., burst river banks, flooded residential areas); 2) the visible presence of standing water within oil palm stands; 3) overlapping coverage of the area by a Sentinel-1 scene acquired on 23 November 2016 (i.e., coincident to within ± 3 days of the Google Earth image); 4) the presence of a variety of growth stages of oil palm; 5) a database of imagery available in the 'time slider' feature of Google Earth (useful for comparing the appearance of oil palm land cover over multiple acquisition dates under flooded and non-flooded conditions); 6) support from the rainfall record of heavy rainfall in the area in the days/weeks preceding the acquisition of the Google Earth and Sentinel-1 scenes.

As the Google Earth image captured over the general region of the study area comprised both low- and high-resolution imagery, a precise boundary for the study area was defined by digitising the extent of the high-resolution Google Earth imagery acquired on 26 November 2016 (Figure 2).

Jambi province's two main weather stations reside within the study area: *Stasiun Klimatologi Muaro Jambi* (SKMJ) and *Stasiun Meteorologi Sultan Thaha* (SMST). According to the Meteorological, Climatological, and Geophysical Agency of Indonesia, BMKG (*Badan Meteorologi, Klimatologi, dan Geofisika*), both stations recorded the year's highest daily rainfall in the days preceding the image acquisitions: SMST recorded 63.3 mm of rainfall on 5 November 2016 and SKMJ recorded 99.4 mm of

rainfall on 16 November 2016. In the 22 days preceding the acquisition of the Sentinel-1 scene, SKMJ recorded 476 mm of rainfall—a total that includes 6 days of missing data, thus the actual rainfall total is likely to be even higher.

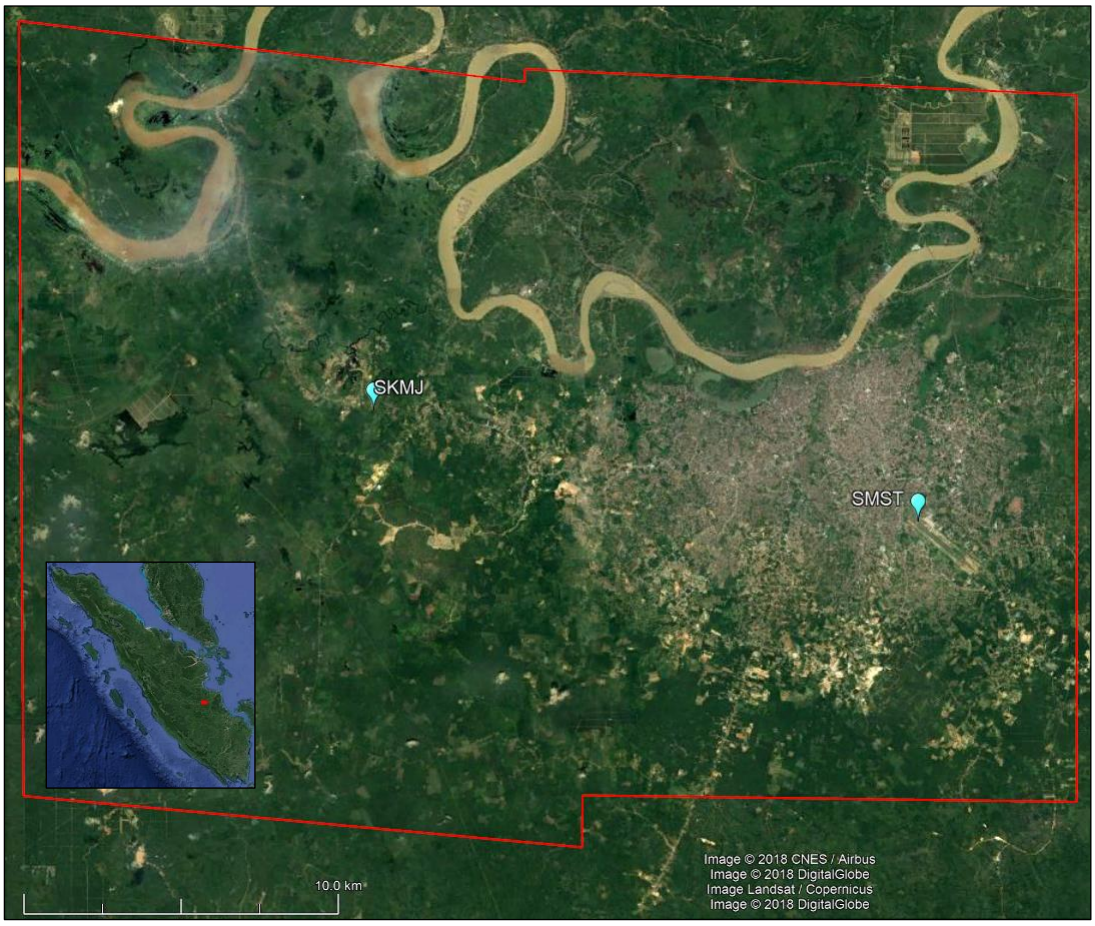

Image credit: Google Earth

Figure 2: The study area in Jambi Province on Sumatra Island, Indonesia (red outline), including the location of two weather stations, SKMJ and SMST. Inset: the study area (red polygon) on Sumatra Island.

The study area extends from 103°22’ E to 103°41’ E and from 1°29’ S to 1°43’ S and captures an area of ~792 km^2, including a section of the Batanghari River and Jambi City. Oil palm is widespread in the study area and smallholdings are the predominant production system although industrial holdings are also present. The terrain is relatively flat and elevation peaks at 87 m.

Jambi Province has undergone rapid land use change with 1 million ha of forest converted to other land cover types between 1990 and 2013 (Tarigan et al., 2016).

During this period, oil palm replaced 360,000 ha of forest (Tarigan et al., 2016). Although peatland is widespread in Jambi Province, it resides mostly outside of the study area (Nurdiana et al., 2016).

The climate in Jambi Province is humid tropical with an average maximum and minimum temperature of 33 °C and 29 °C, respectively (Brown, 2004). It receives abundant rainfall throughout the year, with annual rainfall averaging 2466 mm and ranging from 1306 mm to 3412 mm (Wösten et al., 2006a). The driest months are June-August (Comeau et al., 2013). Evapotranspiration is steady throughout the year and averages 1300 mm per year (Wösten et al., 2006a).

Indonesia's National Board for Disaster Management, BNPB (*Badan Nasional Penanggulangan Bencana*), reported 36 flood events in Jambi Province in 2020 (BNPB, 2021). In the future, the Batanghari River Basin, which is home to Jambi Province's longest river, will experience flooded areas 2.3 times the size of historical flooded areas, and the maximum flood depth will increase from 3.7 m to 4.8 m (Yamamoto et al., 2021). Remaining upland tropical forest in the Batanghari River Basin is under increasing pressure as warming temperatures expand the suitable area for oil palm cultivation into high elevation areas while existing plantations in the basin are increasingly vulnerable to flooding (Yamamoto et al., 2021).

2.2. Data

2.2.1. Sentinel-1 SAR data

The Sentinel-1 data used in this study comprised both a time series and a single date flood scene acquired on 23 November 2016. The time series comprised seven scenes acquired between 26 July 2016 and 17 December 2016, including the flood scene (Table 1).

Table 1: Acquisition dates of the Sentinel-1 scenes.

No.	Acquisition date
1	26 July 2016
2	19 August 2016
3	12 September 2016
4	06 October 2016
5	30 October 2016
6	23 November 2016[1]
7	17 December 2016

[1] Flood scene

The dual-polarisation (VV and VH) data were collected from the Sentinel-1A C-band sensor in Interferometric Wide (IW) swath mode (the primary mode for terrestrial applications) at a geometric resolution of 5 x 20 m. The swath width is 250 km and comprises three sub-swaths and an incidence angle range of 29.1°–46.0°. The data were delivered as a Level-1 Ground Range Detected High Resolution (GRDH) multi-looked product with 10 x 10 m pixel spacing (Table 2). The data are freely available from ESA's Copernicus Open Access Hub (https://scihub.copernicus.eu/dhus/#/home).

To ensure an identical acquisition geometry among scenes, only scenes in the same (ascending) orbit (relative orbit number 171) were downloaded. Although additional scenes in the same ascending orbit were available to download, which would have reduced the revisit time from 24 days to 12 days, the additional scenes contained single-polarisation (VV) data only. As different polarisations contribute different information for the detection of flooded vegetation (Tsyganskaya et al., 2018b), only scenes comprising dual-polarisation (VV and VH) data were used.

Table 2: Characteristics of the Sentinel-1 scenes.

Characteristic	Value
Instrument	Sentinel-1A
Band (wavelength)	C-band (5.6 cm)
Frequency	5.405 GHz
Mode	Interferometric Wide (IW) swath
Polarisation	VV and VH
Resolution	20 x 22 m (ground range and azimuth)
Pixel spacing	10 x 10 m
Incidence angle	30.7°–45.9°[2]
Pass direction	Ascending
Relative orbit	171
Product	Level-1 GRDH (Ground Range Detected, High Resolution)

[2] The near- and far-range incidence angles within the boundary of the study area are 36.2° and 38.5°, respectively.

2.2.2. Google Earth optical imagery

This study used a single scene of very high spatial resolution (< 1 m) Google Earth optical data acquired on 26 November 2016 over the study area. The scene is coincident to within ± 3 days of the Sentinel-1 flood scene acquired on 23 November 2016. The scene provided the reference data for the visual interpretation and manual digitisation of oil palm land cover, and it informed the location of training areas to identify the backscatter characteristics of the different growth stages of oil palm in flooded and non-flooded conditions. Google Earth imagery is freely available through the Google Earth Pro app (https://www.google.com/earth/desktop/).

2.2.3. Ancillary data

A Shuttle Radar Topography Mission (SRTM) digital elevation model (DEM) provided elevation data to exclude areas >30 m in elevation (and therefore unlikely to experience flooding) during the creation of the oil palm land cover mask. The data are freely available from U.S. Geological Survey's (USGS's) EarthExplorer tool (https://earthexplorer.usgs.gov/).

BMKG provided daily rainfall data to support the presence of flooding in the study area in the days/weeks preceding the Google Earth and Sentinel-1 flood scene dates (http://dataonline.bmkg.go.id/).

2.3. Methods

2.3.1. Methodological flowchart

The research methodology (Figure 3) was designed to test whether Sentinel-1 data can detect flooding in oil palm plantations by first examining the backscatter characteristics and separability of different growth stages of oil palm in flooded and non-flooded conditions (herein referred to as the oil palm classes). It comprised five main components: data pre-processing, mapping of oil palm land cover, extraction of training samples for the oil palm classes, examination of backscatter characteristics of the oil palm classes, and a separability analysis. The separability analysis was threefold. To begin, the separability of the backscatter profiles of the oil palm classes on the flood date in the VV and VH polarisations was assessed. Then, the potential for improving the separability using derived bands and a time series was explored.

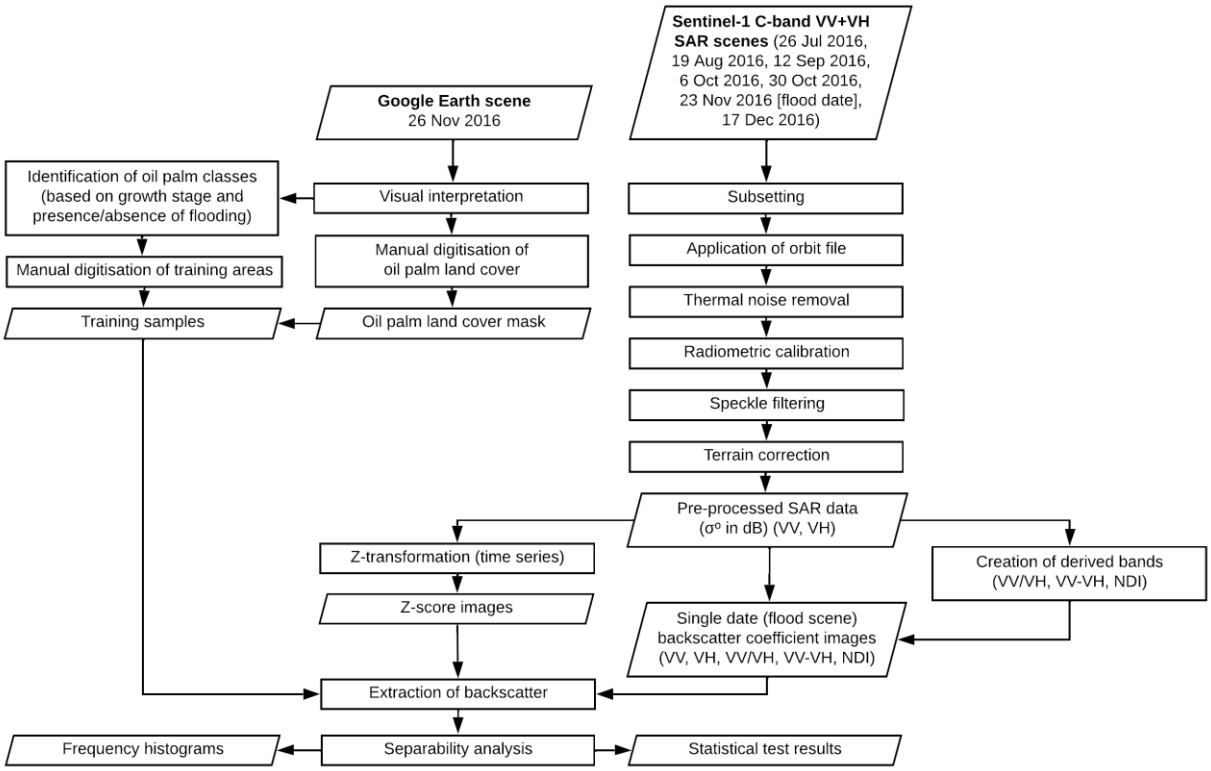

Figure 3: Methodological flowchart.

2.3.2. Pre-processing of Sentinel-1 SAR data

The pre-processing of the seven Sentinel-1 scenes was performed in ESA's SNAP (Sentinel Application Platform) software using the Sentinel-1 Toolbox (S1TBX) module and the Batch Processing tool. Pre-processing was carried out in accordance with the steps described in the training materials published by the Research and User Support for Sentinel core products (RUS) service (Serco Italia SPA, 2018). For a detailed description of the steps involved in the Sentinel-1 GRDH pre-processing workflow refer to Filipponi (2019). The Graph Builder tool was used to specify the main steps and their order of processing (Figure 4).

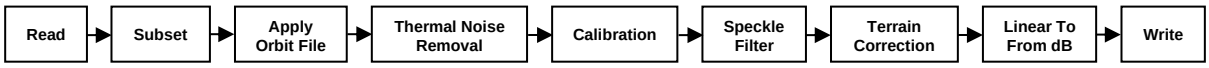

Figure 4: The pre-processing steps for batch processing are first specified in SNAP's Graph Builder tool.

To optimise the pre-processing and storage of data, first the scenes were subset to an area close to the study area boundary to exclude superfluous data from outside the study area boundary. A precise orbit file was applied and thermal noise was removed. The scene was radiometrically calibrated to derive backscatter coefficient values (sigma nought). Calibration in SNAP compensates for the influence of incidence angle on backscatter intensity, although the difference in the near- and far-range incidence angles covering the study area was small. Speckle noise was suppressed through the application of the simple Lee 5x5 speckle filter (Lee, 1980). The adoption of a larger window size during speckle filtering was limited by the numerous smallholder parcels in the study area resulting in a small target area. Geometric distortions were corrected with Range Doppler terrain correction using a SRTM DEM downloaded automatically by the SNAP software. Lastly, sigma nought values were converted to decibel using a logarithmic transformation. The output of the pre-processing in SNAP was an image of VV or VH backscatter coefficient values ($\sigma 0$ in decibels [dB]) in a geographic coordinate system (WGS84) for the flood date and for each date in the time series (an image of the output for the flood date is presented in Appendix B, Figure B1).

To prepare for the time series analysis, and to ensure precise pixel alignment, the scenes were co-registered and combined into a layer stack. The flood scene was used as the master to which the other scenes were slaved. The layer stack was cropped to the precise study area boundary. Finally, the layer stack underwent a visual verification to confirm the precise pixel alignment among the bands in the layer stack.

For visualisation purposes, a false colour composite of the flood scene was created by repeating the above method. Data were kept in sigma nought to create a standard RGB image: R = VV; G = VH; B = VV/VH (Figure 5).

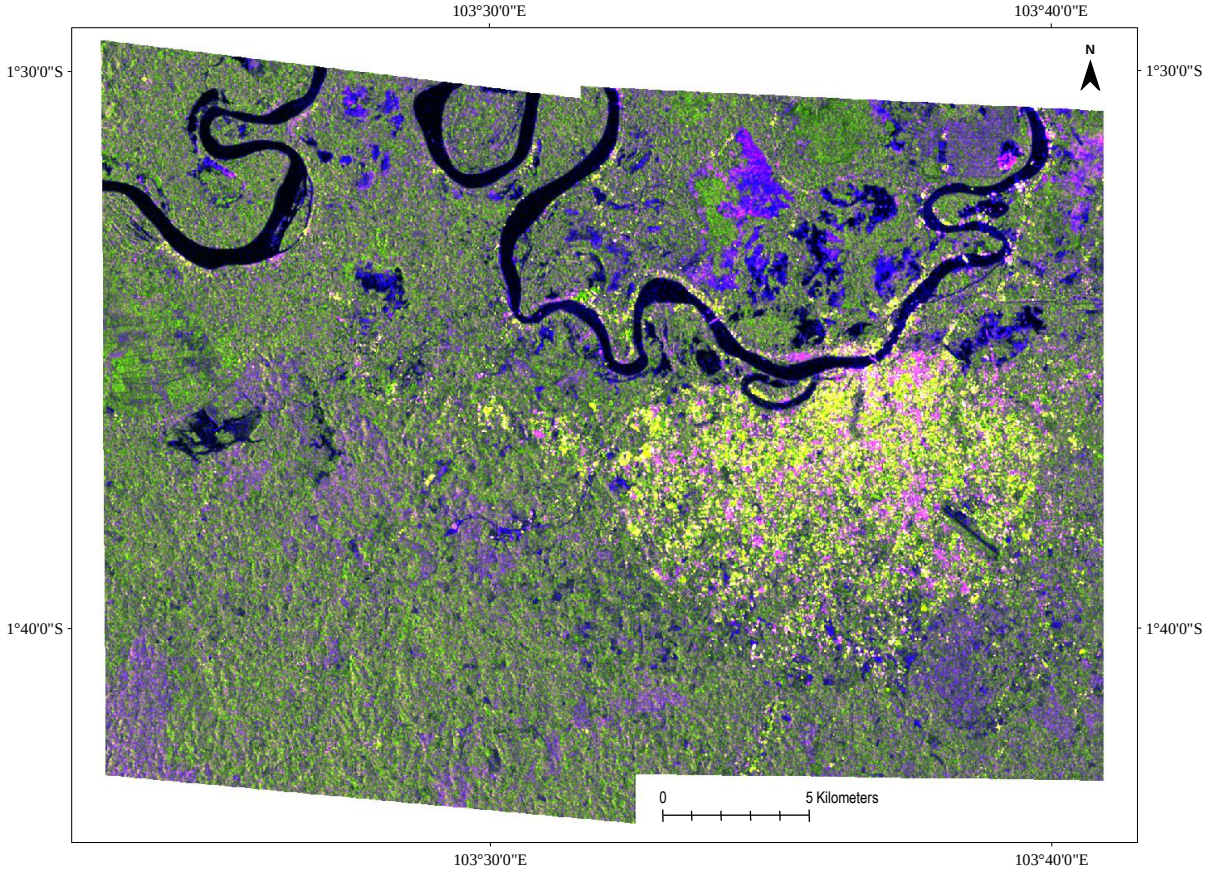

Figure 5: A standard colour composite (R = VV; G = VH; B = VV/VH) of the Sentinel-1 scene over the study area on the flood date in which the Batanghari River appears a dark navy blue, forest is shaded green, oil palm appears purple, Jambi City is marked by bright yellows, greens and pinks, and areas of open water appear navy/royal blue.

2.3.3. Mapping of oil palm land cover

A mask of oil palm land cover was created from the visual interpretation and manual digitisation of oil palm in the study area. Areas >30 m in elevation were excluded from

the digitisation process. The mask informed the location of training areas for the generation of backscatter profiles for the oil palm classes by excluding non-oil palm land cover and oil palm that is less vulnerable to flooding. If the separability analysis revealed sufficient separation among the oil palm classes to perform an image classification, the mask would also be used to restrict the image classification to areas of oil palm land cover only to reduce misclassifications with other land cover types.

Exclusion of areas > 30 m in elevation

An SRTM 1-Arc second (30 m) Global (void-filled) DEM product covering the study area was downloaded in GeoTIFF format (in WGS84) from https://earthexplorer.usgs.gov/ (Entity ID: SRTM1S02E103V3).

In ESRI's ArcGIS Desktop 10.5.1, the Google Earth KML file (in WGS84) of the study area boundary was converted to shapefile. The DEM was clipped to the study area boundary, and the DEM was exported to TIFF format.

Using ArcGIS's spatial analyst function, the DEM was reclassified using two natural break (Jenks) classes: 1 = areas ≤ 30 m in elevation; 2 = areas > 30 m in elevation).

To remove isolated pixels and small groups of pixels, the raster was reclassified using a region group operation. This operation created numerous regions from the isolated pixels and groups of pixels. The field calculator was used to assign a value of 1 or 2 to a new field in the attribute table. Values were assigned to regions based on the value of the pixels in the wider area surrounding each region.

The raster was reclassified using the new attribute field as the reclass field. The raster was reclassified again to convert pixels with a value of '1' to NoData, while pixels with a value of '2' remain unchanged.

Using ArcGIS's convert raster to polygon function, the raster was converted to shapefile. The shapefile was converted to KML for importing into Google Earth. Converting the raster to shapefile before converting it to KML preserves the sharpness of the pixel edges in Google Earth.

The output was a temporary mask for use in Google Earth that obscured areas >30 m in elevation. Only visible areas (areas ≤30 m in elevation) were included in the visual interpretation and manual digitisation of oil palm land cover.

Visual interpretation and manual digitisation of oil palm land cover

A grid was created in ArcGIS and imported into Google Earth to reduce the study area to a series of small manageable areas that aided the visual interpretation process and reduced the chances of missing areas of oil palm land cover. The grid comprised 25 cells across by 24 cells down with each cell covering approximately 1.47 km^2. Cells were analysed systematically, moving from left to right across the columns of cells and moving down each cell in a column before starting a new column.

The visual interpretation and manual digitisation process was carried out in Google Earth. All oil palm land cover ≥5000 m^2 (0.5 ha) in area was digitised. The outer extent of oil palm land cover was digitised (no distinction was made for the different growth stages that may exist within a continuous area of oil palm).

Oil palm is easily identifiable in high-resolution Google Earth imagery due to its distinctive star-shaped crown and planting pattern. The standard planting scheme utilises a triangular pattern with 9-meter spacing between palms, which is designed to boost yield and optimise sunlight infiltration (Chong et al., 2017) (Figure 6).

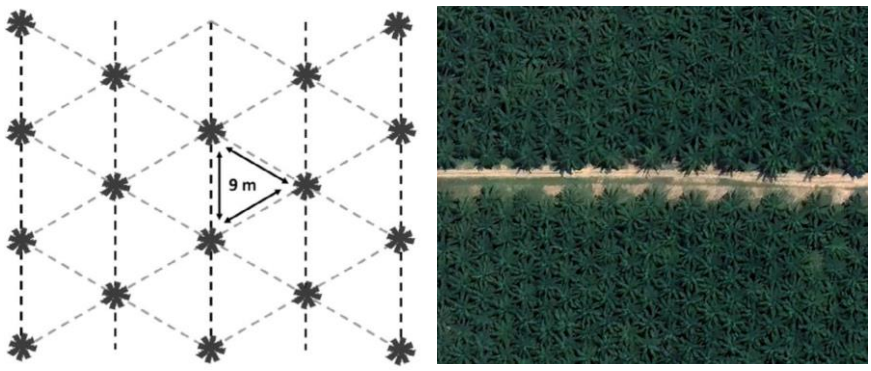

Image credit: Chong et al. (2017)

Image credit: Google Earth

Figure 6: The distinctive star-shaped crown and triangular planting pattern of the oil palm is easily identifiable in high spatial resolution Google Earth imagery.

To minimise potential misclassifications, any buildings or permanent water features visible within an oil palm plantation were digitised for later exclusion from the oil palm land cover mask.

In ArcGIS, the Google Earth KMZ file was converted to a layer file and then exported to shapefile format. Unwanted features (e.g., buildings, reservoirs) were excluded by copying the oil palm land cover shapefile in ArcGIS's table of contents and performing a 'select by location'. Features of the target layer that were completely within the source layer features were selected and exported to shapefile. The erase tool was used to remove the polygons representing unwanted features from the oil palm parcels.

The output was a mask of all oil palm land cover ≥ 5000 m^2 (0.5 ha) in area and ≤ 30 m in elevation in the study area (Figure 7). The mask comprises 1380 individual polygons and covers an area of 53.70 km^2 (5370.32 ha).

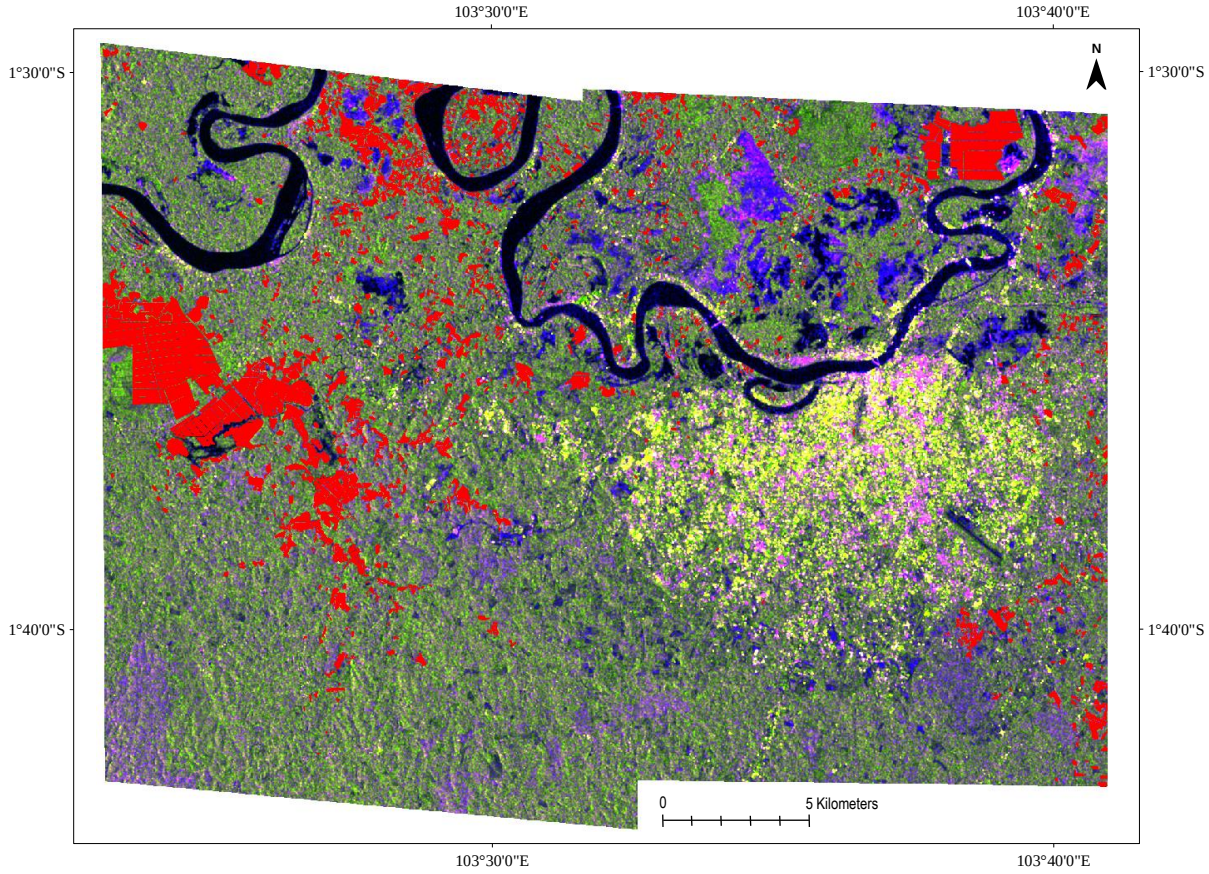

Figure 7: Oil palm land cover (red polygons) overlaying the standard colour composite of the study area on the flood date. The mask represents the extent of oil palm land cover that is ≥5000 m^2 (0.5 ha) in area and ≤30 m in elevation.

2.3.4. Extraction of training samples

Training samples were used to determine the backscatter characteristics of the different growth stages of oil palm in flood and non-flooded conditions. First the training classes were identified and then the training areas were selected.

Identification of training classes

Twelve training classes were identified by visually inspecting the area within the oil palm land cover mask in Google Earth. The classes represent the different growth stages of oil palm in either flooded or non-flooded conditions based on the presence/absence of standing water. The growth stages are based on Fitrianto et al. (2018) who described four classes (seeds, young, teen, mature) of oil palm in a plantation in Indonesia by adopting a canopy density model to estimate stand age based on a series of indices derived from Landsat data. The authors state that the four classes align with the classification of oil palm provided by the Plantation Education Agency of Indonesia, however this study was unable to confirm this. Data to verify a canopy density model or an estimate of stand age was not available for this study. Moreover, oil palm stands of the same age do not necessarily share the same phenology due to differences in the management, growth, and productivity of the stand. Consequently, this study adopted a qualitative approach to define the growth stages using phenology based on image characteristics (Table 3). Fitrianto et al. (2018) acknowledged that their mature class incorporated a particularly wide range of oil palm ages due to the difficulty in distinguishing younger mature palms (15–20 years old) from older mature palms (> 20 years old) using Landsat data. This study attempted to address this by including an additional class (adult) to differentiate a canopy that is partially closed or beginning to close from one that is completely closed. Examples of the classes as they appear in Google Earth are provided in Figure 8.

Table 3: Description of the oil palm growth stages.

Growth stage	Description
Unplanted	No palms visible. Identifiable as oil palm from the land preparation/management.
Seedling	Tiny round dots, recognisable as oil palm due to the planting pattern.
Young	Very small tree crowns and a higher ratio of visible ground cover than canopy/crown cover.
Teen	Small tree crowns with an approximately equal or lower ratio of visible ground cover than canopy/crown cover. Completely open canopy; fronds do not touch fronds on other tree crowns.
Adult	Canopy beginning to close. Some fronds touch fronds on other tree crowns.
Mature	Canopy closed. All tree crowns touch other tree crowns.

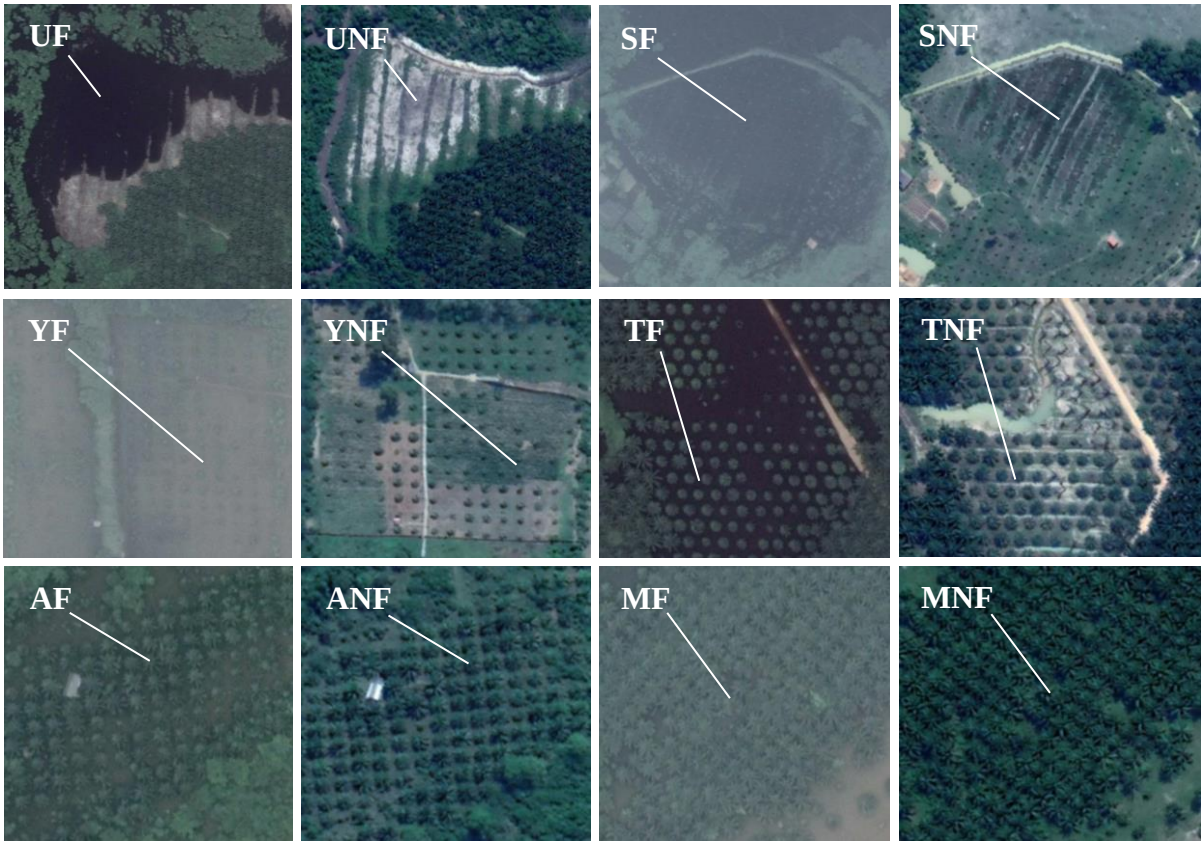

Figure 8: Examples of Google Earth imagery in the study area showing the growth stages of oil palm in flooded and non-flooded conditions. The acquisition date of the flooded imagery is 26 November 2016. The classes are abbreviated as follows: 'NF' = non-flooded; 'F' = flooded; 'U' = unplanted; 'S' = seedling; 'Y' = young; 'T' = teen; 'A' = adult; 'M' = mature.

Selection of training areas

Training areas were identified by visually interpreting the area within the oil palm land cover mask in Google Earth. Finding suitable training areas proved highly challenging as the presence of numerous smallholder plots meant multiple classes were present within a small area and the boundaries between the classes were fuzzy. Consequently, all suitable training areas were sampled. An area was considered suitable if it contained a representative example of a training class, i.e., only one class was present, the stand was uniform (no intercropping, missing trees, or degraded trees), and the presence/absence of standing water was unequivocal. The time slider feature in Google Earth's database of historical imagery facilitated a comparison of an area's appearance under flooded and non-flooded conditions. Polygons were manually digitised around training areas, taking care to exclude edge pixels if the training area was near the border of another class or near the border of the oil palm land cover mask. The KML file was converted to shapefile in ArcGIS and imported to SNAP for further analysis. In total 102 training areas were created (Figure 9). The characteristics of the training samples are shown in Table 4.

Table 4: Characteristics of the training samples.

Training class	**No. of training areas**	**No. of pixels**
Unplanted non-flooded	6	437
Unplanted flooded	2	734
Seedling non-flooded	10	706
Seedling flooded	7	665
Young non-flooded	10	893
Young flooded	8	917
Teen non-flooded	11	720
Teen flooded	8	435
Adult non-flooded	12	626
Adult flooded	7	388
Mature non-flooded	10	884
Mature flooded	11	974
Total	102	8,379

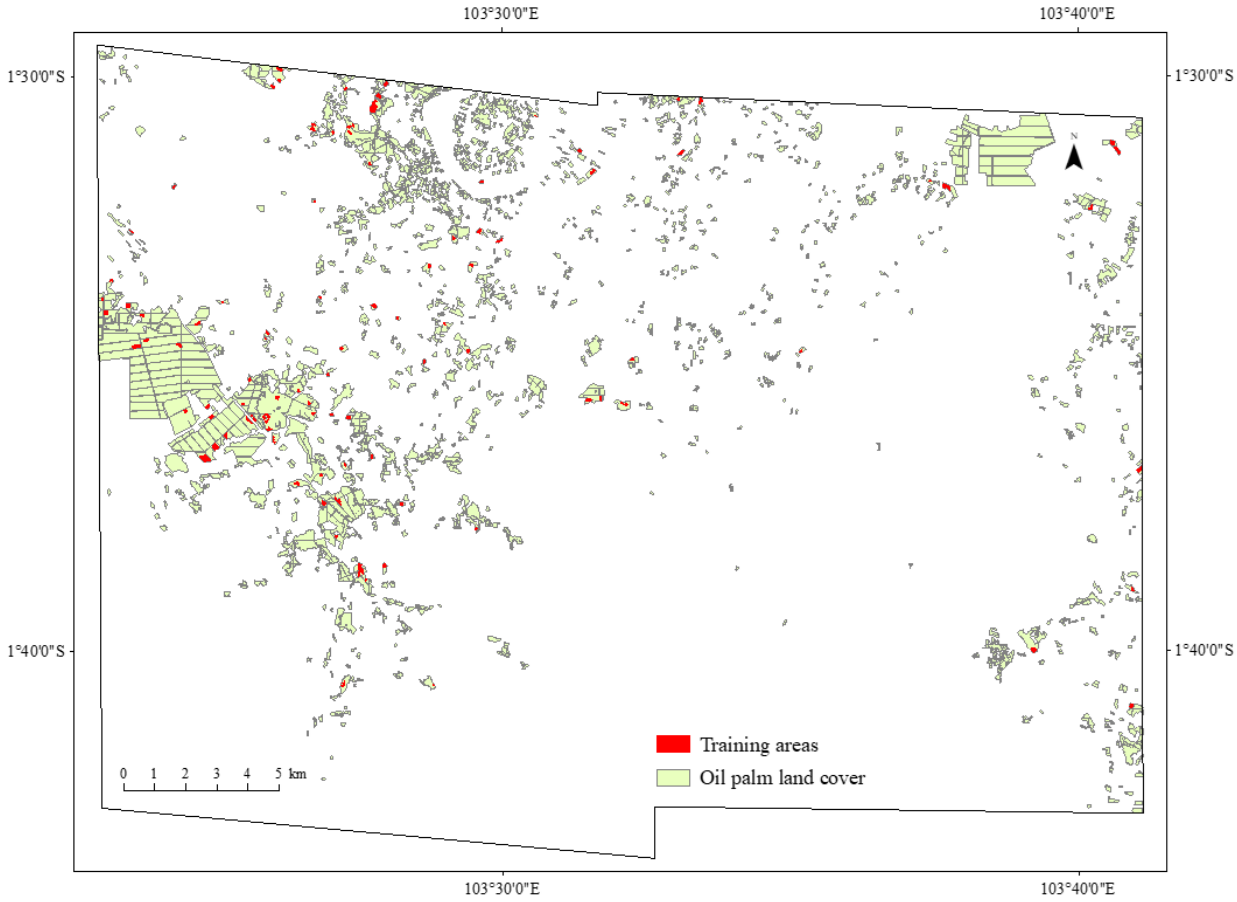

Figure 9: Distribution of the training areas (red polygons) in the study area. The oil palm land cover mask is shown for reference.

2.3.5. Analysis of backscatter characteristics

The output of the pre-processed Sentinel-1 data described in Section 2.3.2. provides the VV and VH backscatter coefficients on the flood date for the analysis of the backscatter characteristics of the oil palm classes. The pixel values of the backscatter coefficients in the VV and VH polarisations were exported from SNAP using the 'Export Mask Pixels' function. The training area shapefiles created in Section 2.3.4. were used to 'mask' the pixel values according to class to enable the pixel values for a single class to be exported. The data were pasted into a Microsoft Excel spreadsheet for further analysis. Frequency histograms of the backscatter coefficients were created in Excel to visually assess the backscatter signatures and the spectral separability of the oil palm classes.

2.3.6. Analysis of separability

A series of statistical tests were conducted in IBM's SPSS 27 to quantify the spectral separability of the classes. A visual assessment of the frequency histograms and SPSS's Normal Q-Q Plots of the backscatter in the VV and VH polarisations suggested that many of the classes (both non-flooded and flooded) had distributions that deviate from normal (the SPSS output of the Normal Q-Q Plots is presented in Appendix B, Figures B2–B3). Yet violating the normality assumption does not generally affect the Type I error rate or the statistical power of the F-test, especially when the sample sizes are large (Delacre et al., 2019). However, unequal variances can strongly influence the Type I error rate and the statistical power of the F-test, especially if the sample sizes are unequal (Tomarken & Serlin, 1986; Delacre et al., 2019).

The sample sizes used in this study were large, but unequal. To assess the equality of the variances, the Levene's test was carried out in SPSS. The Levene's test was based on means with a confidence interval of 95%. The variances in the backscatter coefficients among the non-flooded growth stages were not equal in the VV polarisation, $F(5, 4260) = 18.196$, $p = .000$, or the VH polarisation, $F(5, 4260) = 10.765$, $p = .000$. Similarly, the variances in the backscatter coefficients among the flooded growth stages were not equal in the VV polarisation, $F(5, 4107) = 145.139$, $p = .000$, or the VH polarisation, $F(5, 4107) = 330.342$, $p = .000$.

A Welch's t-test was conducted in SPSS to assess the difference between the mean backscatter coefficients of a single growth stage of oil palm in flooded and non-flooded conditions. Welch's t-test is the most appropriate statistical test to assess the difference between two means when the assumptions of normality and equal variance are violated, and when the samples sizes differ (Delacre et al., 2017).

Transformed Divergence, which is a widely used statistical test in remote sensing, was also undertaken to quantify the spectral separability between an individual growth stage of oil palm in flooded and non-flooded conditions. After first subsetting the layer stack in SNAP to form new products that contain the bands to be used as inputs, the products were exported as a GeoTIFF and imported to Hexagon Spatial's Erdas Imagine 2020. The following input combinations were entered into Erdas Imagine's Transformed

Divergence function: VV backscatter coefficients only, VH backscatter coefficients only, VV and VH backscatter coefficients combined. The shapefiles representing the training areas of the different classes were imported to the Erdas Imagine signature editor. The signature editor's 'evaluate/separability' tool evaluated the separablity of the signatures using the different band combinations as inputs and generated a report of Transformed Divergence scores. Although the Transformed Divergence test assumes the data exhibit a normal distribution, the Normal Q-Q Plots revealed that many of the distributions show only a small deviation from normality. The full cell arrays of the Transformed Divergence scores are provided in Appendix B, Tables B1–B2.

Use of derived bands to improve separability

Three additional bands (in σ0 [dB]) were derived from the VV and VH backscatter coefficients for the flood date using the 'band maths' function in SNAP: a ratio image (VV/VH), a difference image (VV-VH), and a normalised difference image (NDI) (NDI = [VV-VH] / [VV+VH]). Derived backscatter bands can improve the accuracy of image classifications compared to the VV and VH backscatter available in the Sentinel-1 product (Miettinen et al., 2015; Abdikan et al., 2016; Tsyganskaya et al., 2018a).

The pixel values of the backscatter coefficients in the derived bands were exported from SNAP using the 'Export Mask Pixels' function. The training area shapefiles created in Section 2.3.4. were used to 'mask' the pixel values according to class (e.g., 'seedling flooded') to enable the pixel values for a single class to be exported. The data were pasted into a Microsoft Excel spreadsheet for further analysis. Frequency histograms of the backscatter coefficients were created in Excel to visually assess the backscatter signatures of the derived bands and the separability of the oil palm classes. An example of the appearance of the backscatter in the derived bands on the flood date is provided in Figure 10.

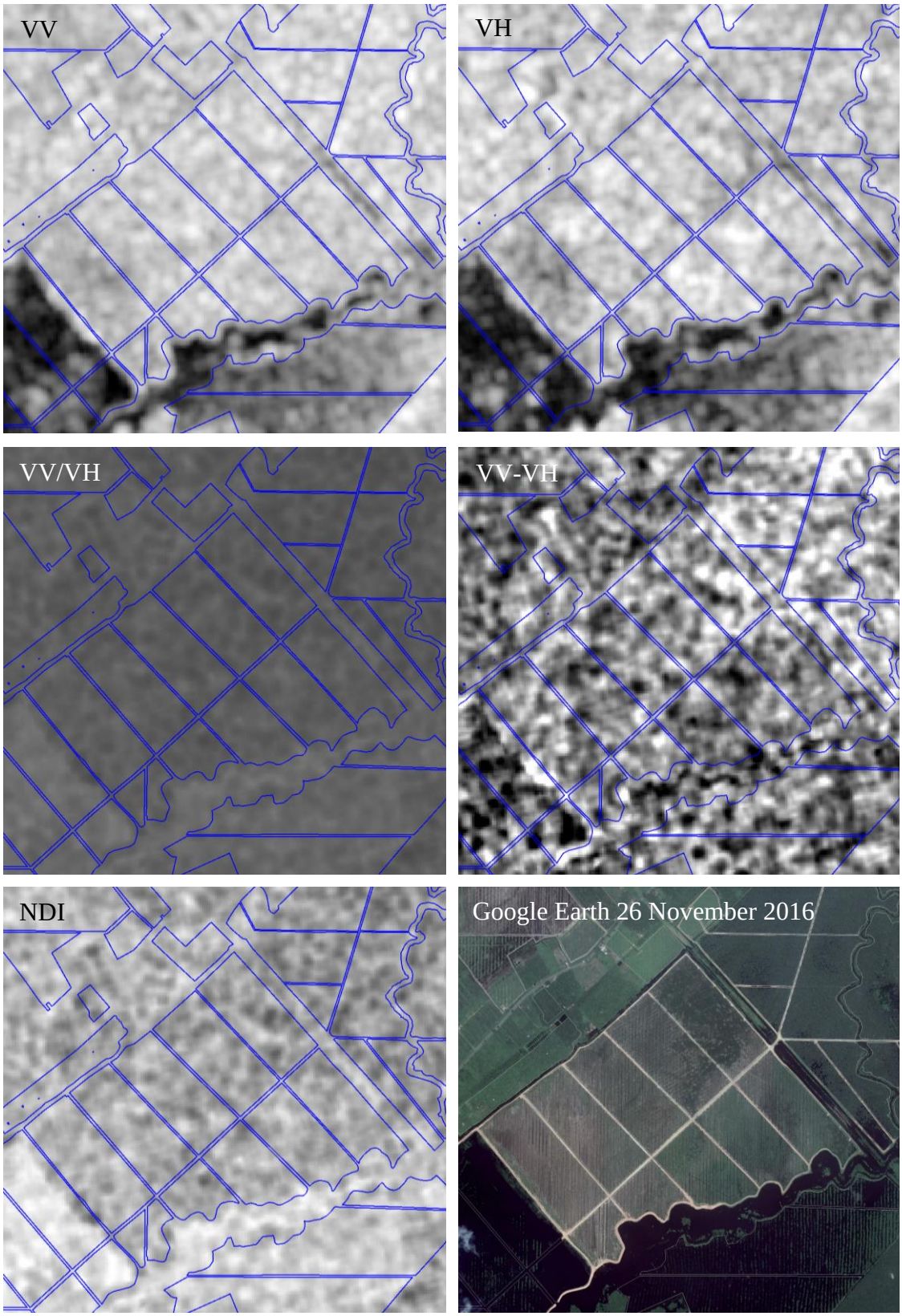

Figure 10: Detailed view of the study area on the flood date showing the appearance of the backscatter in the VV and VH polarisations (in dB) and in the three derived bands: VV/VH, VV-VH, and NDI. Oil palm parcels are outlined in blue.

Use of time series to improve separability

The output of the pre-processed Sentinel-1 data described in Section 2.3.2. provides the VV and VH backscatter coefficients for the time series analysis. The time series analysis was adapted from a methodology presented by Tsyganskaya et al. (2018a). Comparing changes in absolute backscatter values over time is not always feasible due to the influence of environmental factors (e.g., wind, rainfall, phenological stage) on the backscatter values (Tsyganskaya et al., 2018a). To permit comparison, the absolute backscatter value of each pixel in the flood date scene can be standardised over the time series using the following z-transformation (Tsyganskaya et al., 2018a) (Eq. 1):

$$Z = \frac{(x-\mu)}{\sigma} \quad (1)$$

where x is the backscatter value of a pixel on the flood date, and μ and σ are the mean and standard deviation, respectively, of the backscatter values of the same pixel over the time series (Tsyganskaya et al., 2018a).

The z-transformation is performed using the 'band maths' function in SNAP and the output is a z-score image. A z-score image was generated on the flood date for each polarisation (VV and VH). The pixel values of the two z-score images were exported from SNAP using the 'Export Mask Pixels' function. The training area shapefiles created in Section 2.3.4. were used to 'mask' the pixel values according to class (e.g., 'seedling flooded') to enable the pixel values for a single class to be exported. The data were pasted into a Microsoft Excel spreadsheet for further analysis. Frequency histograms of the z-scores were created in Excel to visually assess the standardised backscatter signatures and the separability of the oil palm classes.

3. RESULTS

This section first presents the backscatter characteristics of the oil palm classes on the flood date in the VV and VH polarisations, and then examines the separability of the classes. Finally, the potential to improve the separability of the classes using derived bands and a time series is explored.

3.1. Backscatter characteristics of the oil palm classes in the VV and VH polarisations on the flood date

The mean backscatter coefficient in the VV polarisation was -7.85 dB (σ = 1.19 dB) and -11.41 dB (σ = 4.62 dB) for the oil palm classes in non-flooded and flooded conditions, respectively (Figure 11).

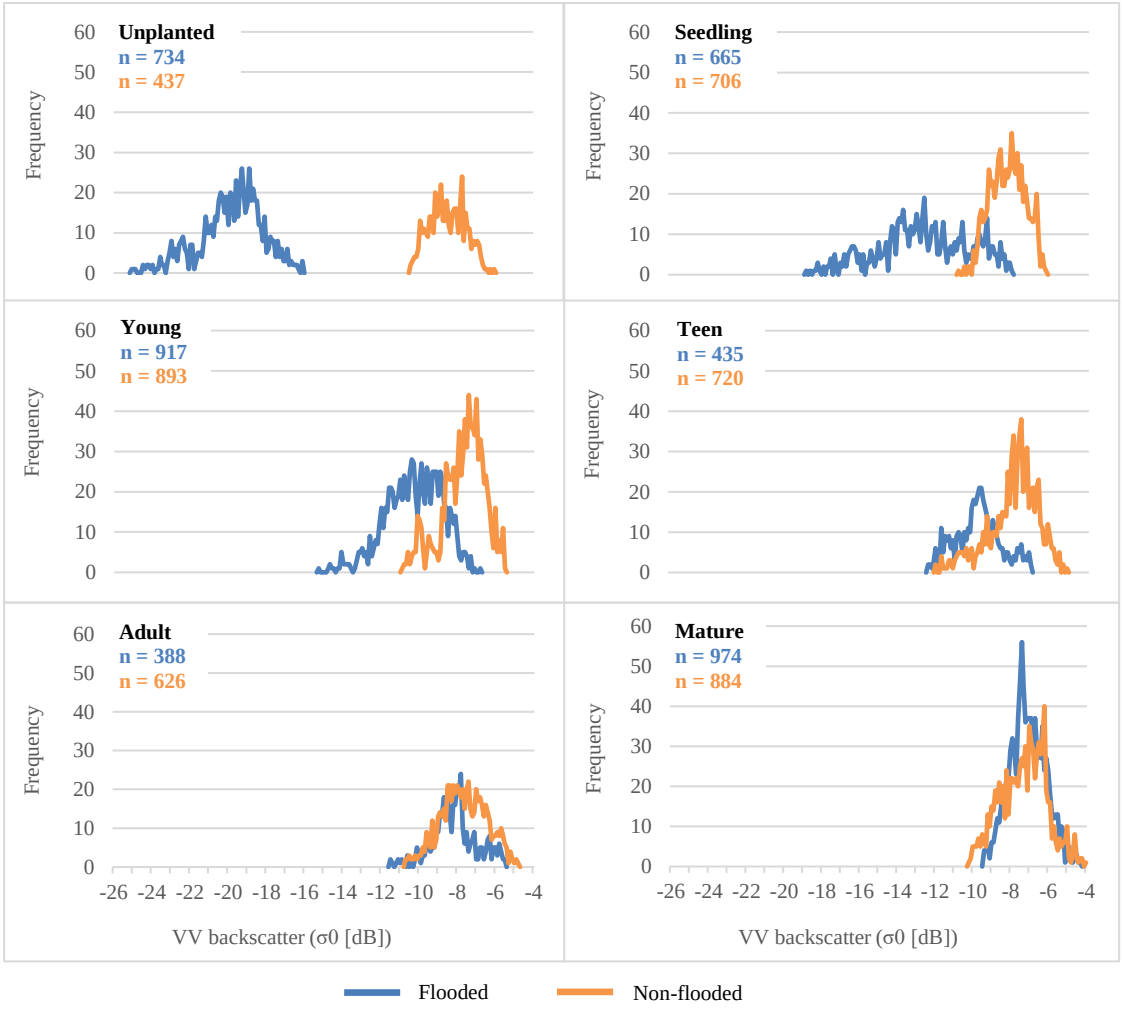

Figure 11: The VV backscatter coefficients on the flood date.

The unplanted flooded class exhibited very low backscatter and appeared dark in the VV image. In flooded conditions, increasing growth stage showed increasing VV backscatter, however, the marginal increase in backscatter diminished with each successive growth stage, and by the adult and mature growth stages the increase in backscatter was minimal. In non-flooded conditions the different growth stages exhibited similar backscatter responses revealing that the growth stage had little impact on C-band backscatter when flooding was absent. The backscatter coefficients of the seedling and young growth stages displayed a wider dynamic range in flooded conditions than in non-flooded conditions.

The mean backscatter coefficient in the VH polarisation was -14.32 dB (σ = 1.36 dB) and -18.16 dB (σ = 3.89 dB) for the oil palm classes in non-flooded and flooded conditions, respectively (Figure 12).

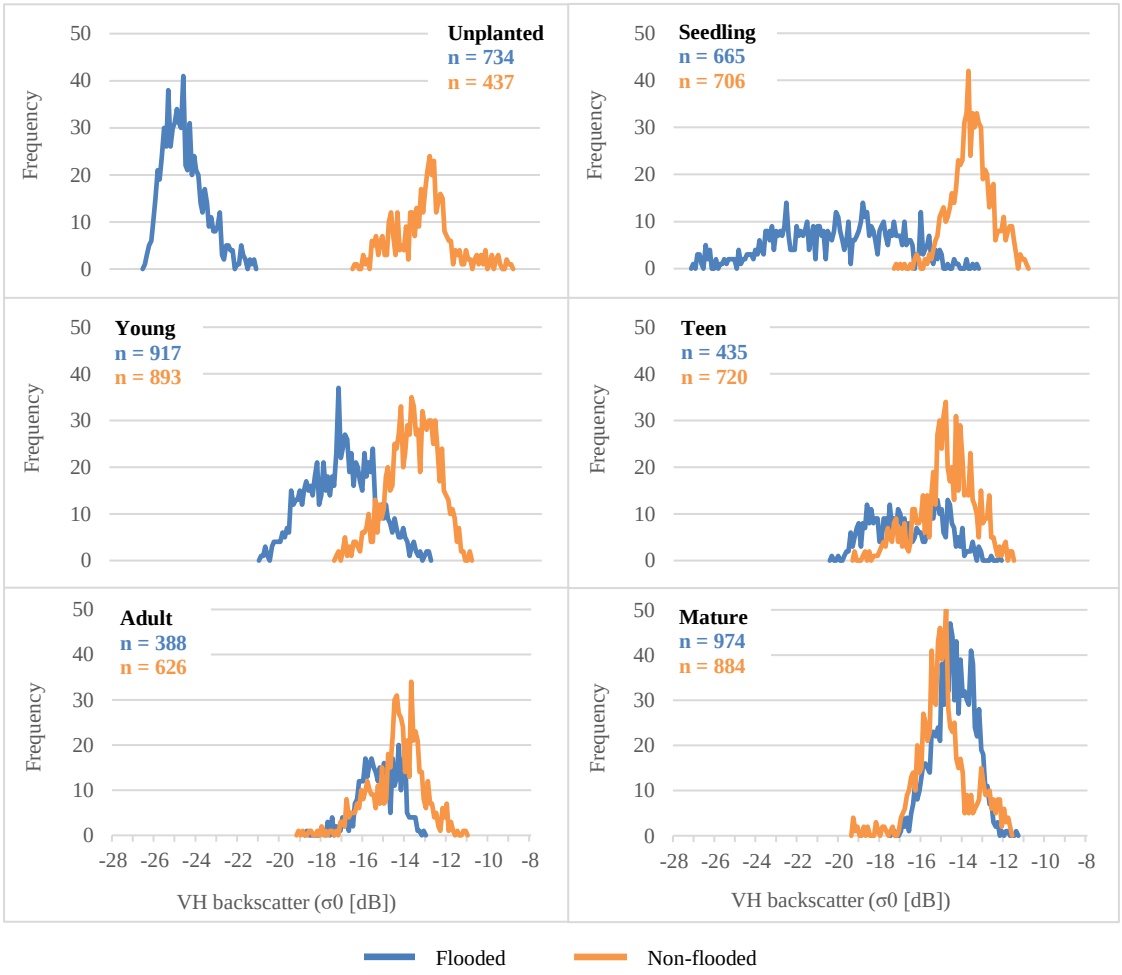

Figure 12: The VH backscatter coefficients on the flood date.

The backscatter response of all classes was lower in the VH polarisation than in the VV polarisation. The pattern of backscatter observed in the VH polarisation mirrors that described above for the VV polarisation. A summary of the backscatter characteristics (min., max., mean., std. dev.) is presented in Appendix B, Table B3.

3.2. Separability of the oil palm classes in the VV and VH polarisations on the flood date

The Welch's t-test assessed the difference in the backscatter response of an individual growth stage of oil palm when flooding was present compared to when flooding was absent. In both polarisations, and for all growth stages of oil palm, the Welch's t-test showed a significant difference between the mean backscatter coefficients of a single growth stage of oil palm in flooded and non-flooded conditions at the level of $\alpha = 0.05$ (Table 5).

Table 5: Welch's t-test comparing the means of the backscatter coefficients of the growth stages in flooded (F) and non-flooded (NF) conditions.

Growth stage (F v. NF)	Polarisation	*Welch's t*	df1	df2	*p*
Unplanted	VV	22515.868	1	1165.302	.000
Unplanted	VH	23209.376	1	708.584	.000
Seedling	VV	1992.902	1	836.794	.000
Seedling	VH	3106.327	1	816.890	.000
Young	VV	1812.635	1	1710.392	.000
Young	VH	2648.440	1	1699.367	.000
Teen	VV	598.497	1	965.514	.000
Teen	VH	333.398	1	771.877	.000
Adult	VV	37.739	1	837.133	.000
Adult	VH	135.726	1	966.672	.000
Mature	VV	13.475	1	1673.270	.000
Mature	VH	85.239	1	1649.212	.000

The Transformed Divergence test quantified the spectral separability among the oil palm classes using the input combinations: VV backscatter coefficients only, VH backscatter coefficients only, both VV and VH backscatter coefficients (VV and VH) (Table 6).

Table 6: Average separability of an individual growth stage of oil palm in flooded (F) and non-flooded (NF) conditions in VV polarisation, VH polarisation, and both polarisations together (VV and VH) using Transformed Divergence[3].

Growth stage (F v. NF)	Average separability (VV)	Average separability (VH)	Average separability (VV and VH)
Unplanted	2000	2000	2000
Seedling	1641	1864	1946
Young	785	1035	1139
Teen	425	318	521
Adult	30	134	156
Mature	25	74	106

[3] Transformed Divergence scores range from 0 (no separability) to 2000 (excellent separability). Scores above 1900 represent good separation while scores below 1700 signify poor separation (Jensen, 2005).

Compared to the VV polarisation, the VH polarisation generally achieved a slightly higher separability between a single growth stage of oil palm in flooded and non-flooded conditions, although the highest separation was achieved when the backscatter of both polarisations was used.

The unplanted growth stage displayed unique backscatter profiles in flooded and non-flooded conditions and exhibited very high separability in both polarisations. This was confirmed by the Transformed Divergence test, which found that these two classes had the highest possible separability (2000) in all polarisation combinations.

The backscatter profiles of the seedling growth stage in flooded and non-flooded conditions exhibited high separability in both polarisations, and this was confirmed by the Transformed Divergence test, which recorded good separability (1946) between these two classes when the backscatter of both polarisations was considered.

A partial overlap in the backscatter distributions of the young growth stage in flooded and non-flooded conditions existed in both polarisations, and the Transformed Divergence test reported poor separability between these two classes in all polarisation combinations.

There was considerable overlap in the backscatter distributions of the teen, adult, and mature growth stages in flooded and non-flooded conditions in both polarisations. In fact, by the adult growth stage, the backscatter profile in flooded conditions resembled that of non-flooded conditions. The Transformed Divergence test scores were extremely low in all polarisation combinations for the teen, adult, and mature growth stages.

To test whether fewer classes improved the separability, classes were grouped into a set of refined classes. The backscatter responses of the individual growth stages of oil palm in flooded and non-flooded conditions revealed that in both polarisations the C-band signal saturated by the adult growth stage. Consequently, the flooded classes were grouped into an 'open canopy' class (i.e., seedling, young, teen) and a 'closed canopy' class (i.e., adult, mature). Due to its unique backscatter profile, the unplanted flooded class remained as a separate class. The non-flooded classes were combined into a single group as the growth stage appears to have minimal impact on the backscatter response of the non-flooded classes.

Figure 13 shows the backscatter profiles of the refined oil palm classes while Table 7 presents the average separability of the refined classes. There was reasonable separability between open canopy and closed canopy oil palm in flooded conditions, with a ~3 dB and ~4 dB overlap in VV backscatter and VH backscatter, respectively. In contrast, the overlap between open canopy flooded oil palm and non-flooded oil palm was greater, with a ~4 dB and ~5 dB overlap in VV backscatter and VH backscatter, respectively. The backscatter distributions of closed canopy flooded oil palm and non-flooded oil palm overlapped completely. Although the refined classes enhanced the separability, they did not improve C-band's ability to detect the presence/absence of flooding in a discernible way and the separability remained insufficient to perform an image classification.

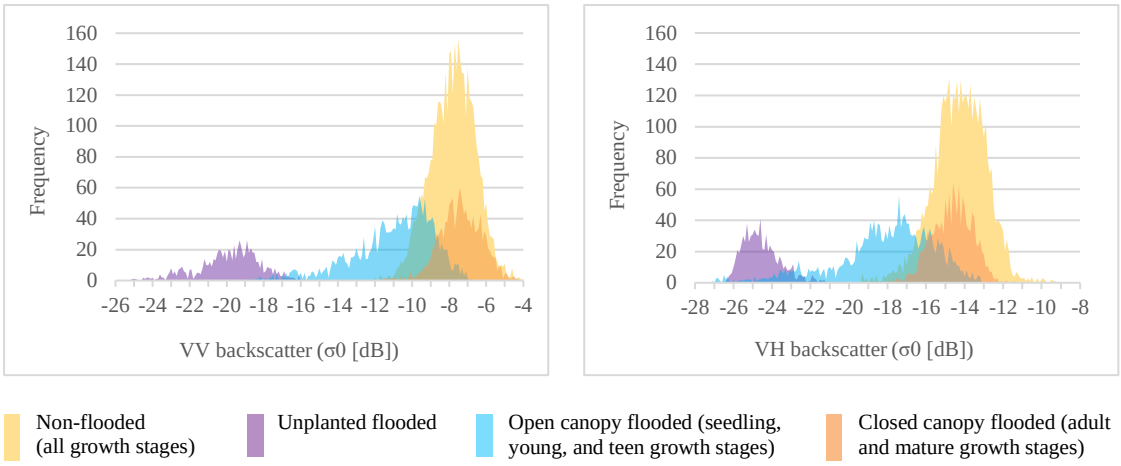

Figure 13: The VV and VH backscatter coefficients on the flood date for the refined classes.

Table 7: Average separability of the refined classes in VV polarisation, VH polarisation, and both polarisations together (VV and VH) using Transformed Divergence[4].

Class	Average separability (VV)	Average separability (VH)	Average separability (VV and VH)
Non-flooded[5]	1026	1069	1155
Unplanted flooded	1995	1989	1998
Open canopy flooded[6]	1448	1484	1574
Closed canopy flooded[7]	1116	1143	1181
Average of all classes	**1396**	**1421**	**1477**

[4] Transformed Divergence scores range from 0 (no separability) to 2000 (excellent separability). Scores above 1900 represent good separation while scores below 1700 signify poor separation (Jensen, 2005).
[5] The non-flooded class combines all growth stages (unplanted, seedling, young, teen, adult, mature).
[6] The open canopy flooded class combines the seedling, young, and teen growth stages.
[7] The closed canopy flooded class combines the adult and mature growth stages.

3.3. Use of derived bands to improve separability

The backscatter response in the derived bands (VV/VH, VV-VH, NDI) was considerably less useful than the backscatter response in the VV and VH polarisations (Figures 14–15). The unplanted growth stage showed some distinction between flooded and non-flooded conditions in the VV/VH and NDI bands, but the distinction was much weaker than the unique backscatter pattern shown in the VV and VH polarisations. The remaining classes did not reveal a distinctive backscatter pattern according to growth stage or ground condition in any of the derived bands.

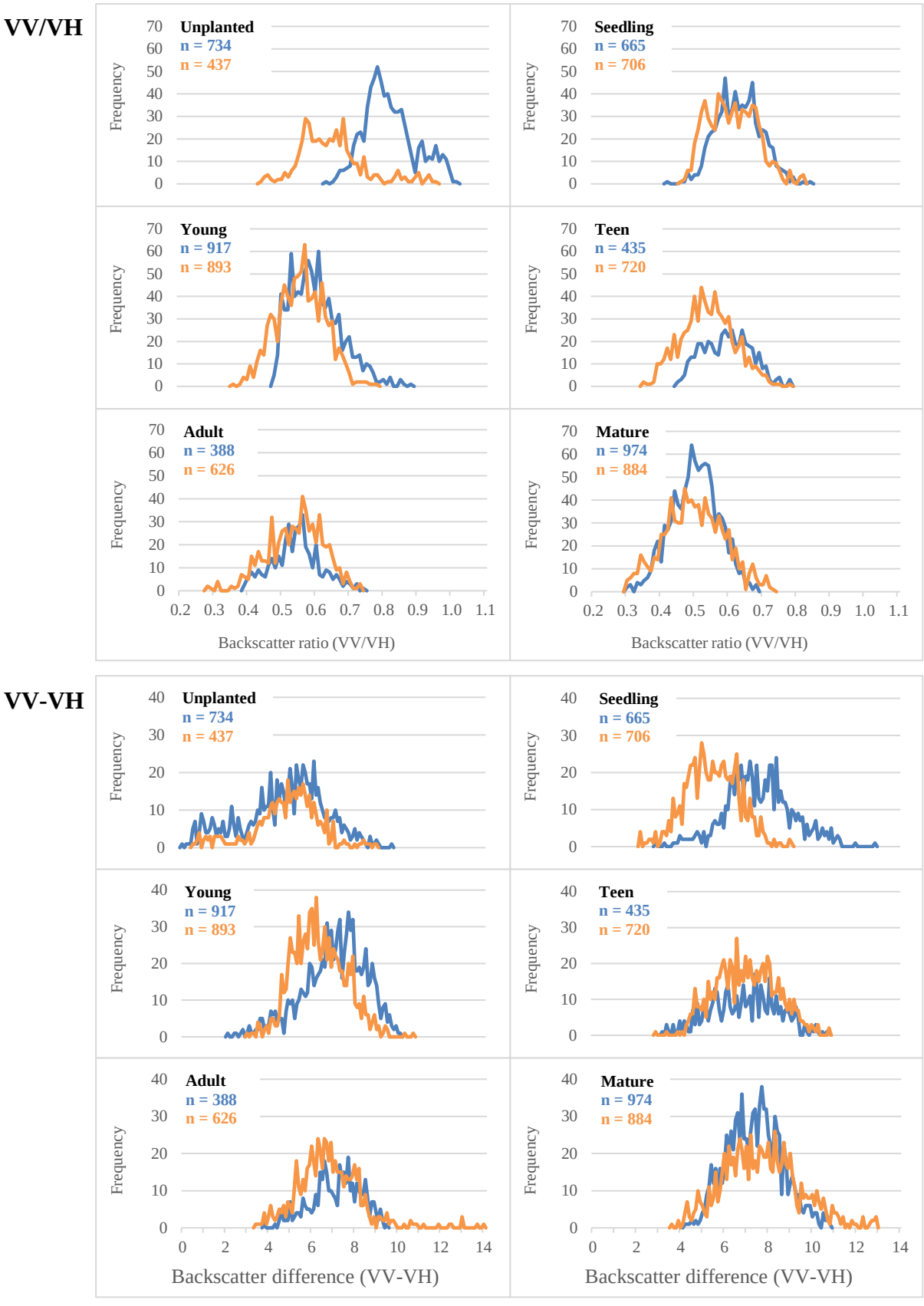

Figure 14: The VV/VH backscatter ratio and the VV-VH backscatter difference on the flood date.

NDI

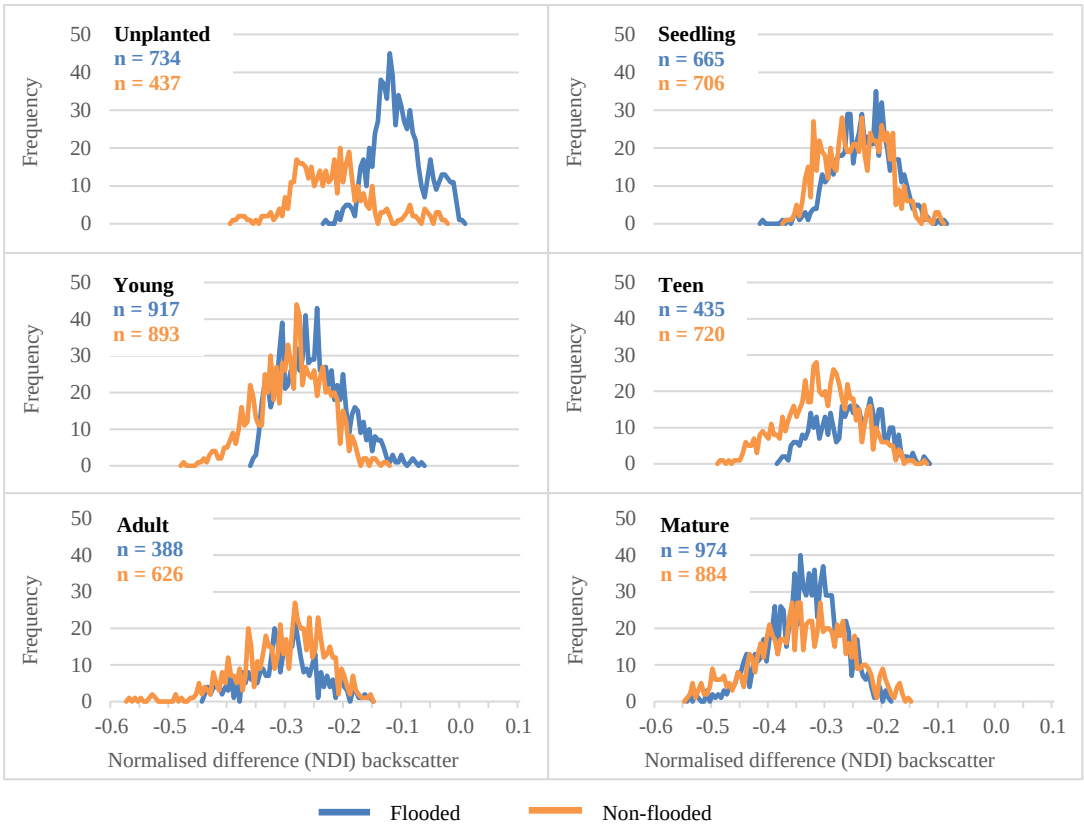

Figure 15: The normalised difference (NDI) of the backscatter on the flood date.

3.4. Use of time series to improve separability

The standardised backscatter (z-score) compared the backscatter response on the flood date to the backscatter response recorded on six other dates in the time series. For the unplanted growth stage in flooded conditions, the standardised backscatter in the VV and VH polarisations showed the same distinct pattern: the backscatter response was highly concentrated between 2.0 and 2.5 standard deviations below the mean (i.e., the mean of the backscatter values of the same pixel over the time series) (Figures 16–17). This is consistent with our expectations: assuming flooding was not present on the other six dates in the time series, the backscatter intensity of the unplanted growth stage on the flood date would be lower than the backscatter intensity averaged over the rest of the time series. The unplanted growth stage in flooded conditions is essentially an open water surface and the smooth surface acts as a specular reflector of microwave energy. Likewise, the standardised backscatter of the seedling and young growth stages in flooded conditions was heavily skewed towards standard deviations below the mean, although the values were more variable than those of the unplanted growth

stage in flooded conditions. Yet when compared to the backscatter profiles of the flood date, the standardised backscatter profiles of the unplanted, seedling, and young growth stages exhibited greater overlap in flooded and non-flooded conditions. Therefore, the time series approach did not improve the separability of the oil palm classes. As seen with the flood date backscatter response, the standardised backscatter eventually saturated and showed no sensitivity towards the presence/absence of flooding in the teen, adult, and mature growth stages.

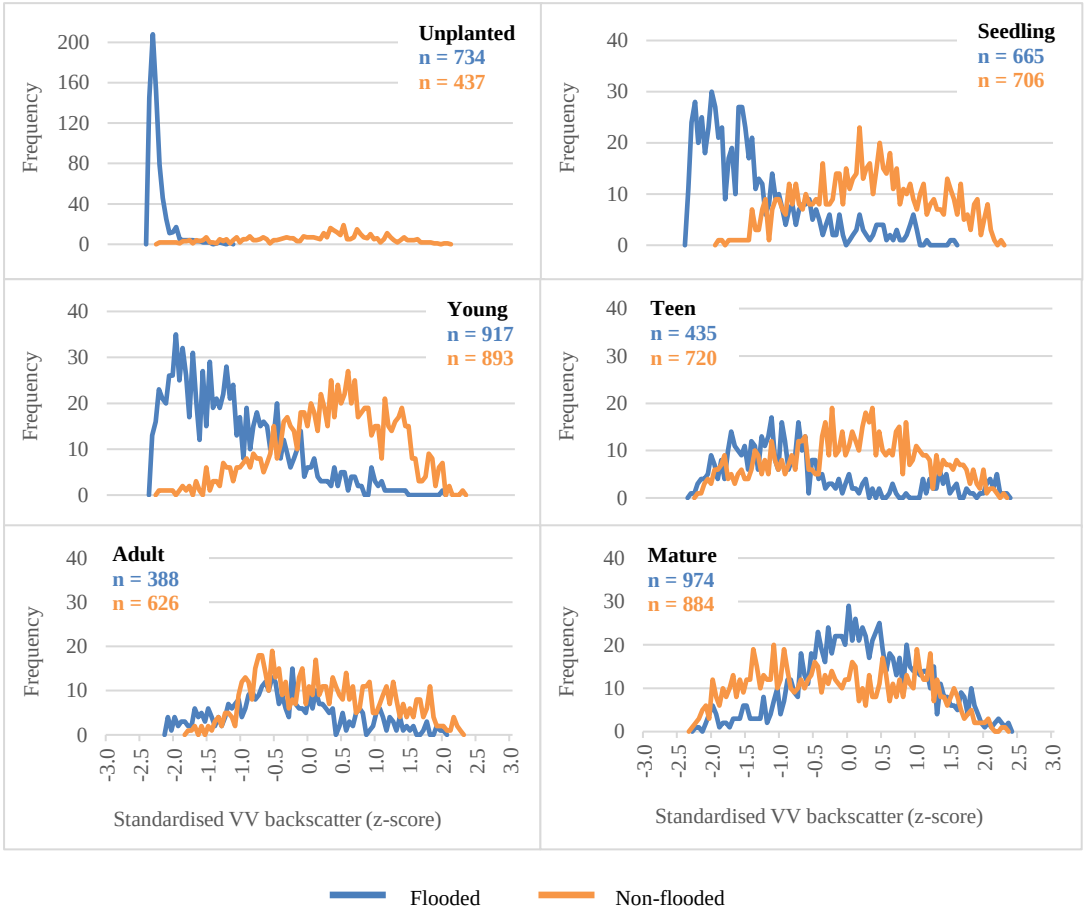

Figure 16: The standardised VV backscatter (z-score) on the flood date.

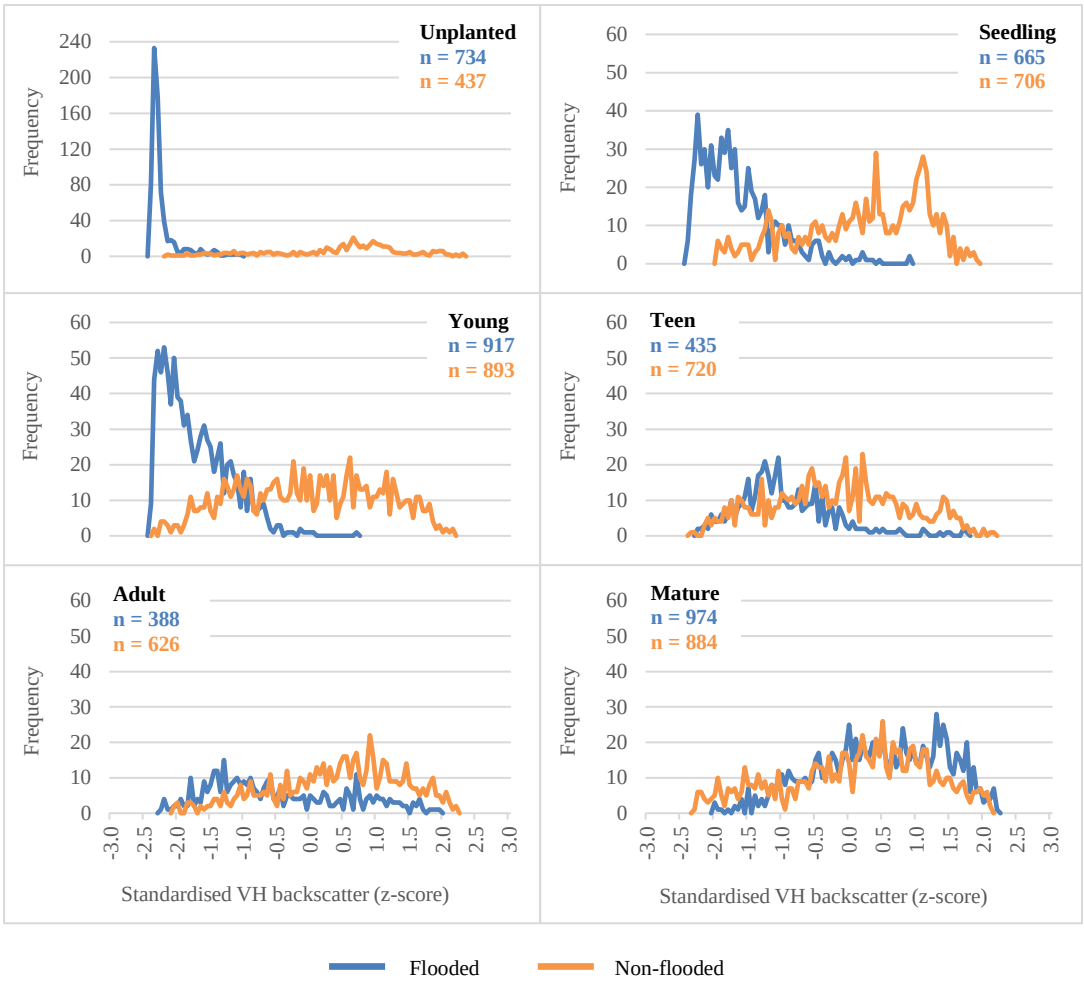

Figure 17: The standardised VH backscatter (z-score) on the flood date.

4. DISCUSSION

This study examines the capability of Sentinel-1 C-band VV and VH SAR data to detect the presence/absence of flooding in oil palm plantations. The oil palm is stratified into growth stages that represent the different phenological stages of the oil palm present in the study area based on the image characteristics of Google Earth imagery. Because the growth stage determines the structure, transmissivity, and surface roughness of the oil palm, it has a strong effect on the backscatter return. By accounting for the growth stage, a clearer understanding of the strengths and limitations of C-band data for the detection of flooding in oil palm is achieved compared to if differences in target characteristics are ignored. Similarly, if only closed canopy oil palm is examined, the presence of flooding in a plantation may be underestimated. In this study, classes are derived from the different growth stages of oil palm in flooded and non-flooded conditions, and the backscatter characteristics and spectral separability of the classes are explored. Here we discuss the key findings and the sensitivities of the method.

4.1. Backscatter characteristics and separability of the oil palm classes

There is a significant difference in the mean backscatter response of the individual growth stages of oil palm in flooded and non-flooded conditions in the VV and VH polarisations. This is true for all growth stages including the adult and mature growth stages, which showed a near total overlap in their distributions. This is due to the large sample sizes causing even slight differences in the means to be statistically significant.

The backscatter distributions of the classes overlap to such an extent that unique backscatter profiles for the classes are not identified, except for unplanted flooded oil palm. For all classes, the highest separability is achieved with dual-polarisation backscatter rather than single-polarisation backscatter, which is consistent with the literature (Abdikan et al., 2016; Pham-Duc et al., 2017; Tsyganskaya et al., 2018b).

The high separability of the unplanted flooded oil palm is expected as the sensor is essentially detecting standing open water. In both VV and VH polarisations, upon interaction with a calm water surface, the signal undergoes specular or forward scattering

away from the antenna. For all other classes, the ground surface and the presence of palms increases the interaction of the signal with the target, thereby increasing the proportion of the signal that is returned to the antenna. Consequently, the unplanted flooded class has a uniquely low backscatter return compared to the other classes.

The backscatter response of all classes of oil palm is higher in the VV polarisation than in the VH polarisation, which is expected. In forest applications, cross-polarised backscatter, which is associated with volume scattering, is generally lower than co-polarised backscatter, which is associated with surface scattering and double bounce scattering (Rosenqvist, 2018; Kellndorfer, 2019).

According to Rosenqvist (2018), the oil palm's dense canopy of large fronds prevents the C-band, and even the L-band, signal from penetrating the canopy. The C- and L-band signals exhibit similar backscatter in oil palm plantations, with the signal restricted to interactions with the top of the canopy where the large leaves and branches generate a strong direct co-polarisation scatter (Rosenqvist & Oguma, 1995; Rosenqvist, 2018). Consequently, the backscatter that is observed in the older growth stages is predominantly surface scattering from the oil palm canopy while the dominant scattering from low or sparse vegetation is direct surface scattering from the ground (Ranson & Sun, 2000). The impenetrability of the oil palm's dense canopy by the C-band signal means that volume scattering observed in this study is limited to vegetation that is low or sparse (Rosenqvist, 2018). C-band's limited ability to penetrate the oil palm's dense canopy means that the double bounce effect that creates a strong return signal and very bright backscatter in inundated forests is not observed in this study.

In the absence of flooding, the different growth stages have little impact on the backscatter response of the C-band signal. However, in flooded conditions, a clear pattern of increasing backscatter with palm growth exists in both polarisations. The mean VV and VH backscatter coefficients of the flooded classes increase with increasing growth stage, but the marginal increase in backscatter diminishes with each successive growth stage. The increase in VV and VH backscatter with growth stage in flooded conditions represents a transition from forward (specular) scattering in unplanted flooded oil palm to an increase in volume scattering and direct surface scattering as the juvenile palms grow. Eventually a saturation point is reached and the

VV and VH backscatter response of the adult and mature growth stages in flooded conditions resembles that of non-flooded conditions.

Saturation "indicates that additional contribution from a certain parameter, in this case biomass, does not result in a higher backscatter response" (Rosenqvist, 1996, p. 3223). While cross-polarisations like VH are sensitive to biomass and therefore sensitive to differences in palm growth, C-band's short wavelength and limited canopy penetration inhibits interactions with the physical parameters of the palms (Sinha et al., 2015) causing it to saturate sooner (at ~ 60–70 tons/ha) than bands with longer wavelengths (Nizalapur et al., 2010). The saturation of the C-band signal in oil palm plantations is reported in several studies (e.g., Rosenqvist & Oguma, 1995; Ballester-Berman & Rastoll-Gimenez, 2021; Darmawan et al., 2021).

Consequently, C-band backscatter on its own struggles to distinguish between different growth stages of oil palm (Descals et al., 2019; Xu et al., 2021). Often additional data (e.g., L-band backscatter, optical data, texture variables, vegetation indices) are needed to complement C-band data when attempting to distinguish between young and mature oil palm (Descals et al., 2019; Xu et al., 2021; Yamamoto et al., 2021).

In addition, the spectral variance of the backscatter profiles contributes to the poor separability of the classes. This is most notable in the seedling and young growth stages, which show a higher spectral variance in flooded conditions than in non-flooded conditions in the VV polarisation and, in particular, the VH polarisation.

VH polarisation has a wider backscatter variability in vegetated areas than VV polarisation (Twele et al., 2016) and in sparsely vegetated areas the low backscatter generated by cross-polarisations can lead to the misclassification of sparse vegetation as water (Manjusree et al., 2012; Twele et al., 2016). In addition, the large spread in backscatter coefficients for the flooded seedling class is influenced by the spacing of the oil palms (~ 9 m apart) relative to the spatial resolution of the SAR data (10 x 10 m). The signal detects the standing open water between the seedlings, resulting in low VV and VH backscatter. However, the interaction of the signal with the seedlings adds complexity to the backscatter return. Volume scattering is generated by C-band's ability to penetrate the seedling's branches and leaves. In addition, shorter

wavelengths like C-band may generate weak double bounce scattering in vegetation that is low or sparse (Martinis & Rieke, 2015).

In young flooded oil palm, the larger size of the palms compared to the seedlings means that the signal detects less standing water. Larger palms mean less open surface water to create specular or forward scattering and reduced penetration of the palm's crowns to detect water underneath. For this reason, this class does not exhibit the same low backscatter in the VV and VH polarisations as the unplanted and seedling flooded classes, but it still displays a wider spectral variance than the same growth stage in non-flooded conditions.

While the spectral variances of the different growth stages in non-flooded conditions are relatively stable, the spectral variance of the different growth stages in flooded conditions narrows as the growth stage increases. By the teen growth stage, the spectral variance of the growth stage in flooded and non-flooded classes is similar.

Although the backscatter response of flooded oil palm cannot be compared to other studies as, to the best of the author's knowledge, no other studies have reported the backscatter characteristics of oil palm in flooded conditions, it is possible to compare the spectral variance of non-flooded oil palm. For mature non-flooded oil palm, this study observed backscatter coefficients ranging from -10.27 dB to -4.09 dB in the VV polarisation and from -19.35 dB to -11.73 dB in the VH polarisation. This is a dynamic range of 6.2 dB and 7.6 dB in the VV and VH polarisations, respectively. In contrast, the backscatter coefficients of 'closed canopy' oil palm reported in Miettinen et al. (2015) ranged from approximately -6 dB to -8 dB in the VV polarisation and approximately -14.75 dB to -16.5 dB in the VH polarisation. This is a dynamic range of 2 dB and 1.75 dB in the VV and VH polarisations, respectively. Furthermore, across all growth stages examined by Rosenqvist and Oguma (1995), VV backscatter fell within a dynamic range of ~ 3 dB, with a saturation point around -6 dB. This suggests that the spectral variance of the non-flooded classes (as well as the flooded classes) is much wider than ideal due to the presence of residual speckle noise in the data (Ballester-Berman & Rastoll-Gimenez, 2021).

Nonetheless, is important to note that the backscatter response observed in this study is not transferable to other study settings (Mohd Najib et al., 2020; Ballester-Berman & Rastoll-Gimenez, 2021). The interactions between the sensor and the target are unique and arise from a particular combination of sensor characteristics and target characteristics (see Appendix A for a detailed overview of the scattering mechanisms observed in flooded vegetation). Studies based on ground truth measurements (e.g., Teng et al., 2015; Toh et al., 2019) report considerably different values for the oil palm's physical parameters across different ages. This is significant because the backscatter response of oil palms depends on their structure and planting density (Darmawan et al., 2021). Differences in management systems, planting patterns, planting density, plant age, and plant morphology will see differences in the backscatter response that studies observe (Ballester-Berman & Rastoll-Gimenez, 2021).

The backscatter profiles of the oil palm classes in the derived bands are less distinctive than the backscatter profiles in the VV and VH polarisations. In the time series, both the VV and VH standardised backscatter (z-scores) reach total saturation by the adult growth stage, which mirrors the point of saturation observed on the flood date. The VV and VH standardised backscatter is sensitive to the presence/absence of flooding in the unplanted, seedling, and young growth stages, but it does not improve the distinctiveness of the classes compared to the backscatter of the flood date. Therefore, the backscatter of the derived bands, and the standardised backscatter of the time series, do not improve the separability of the oil palm classes compared to the use of single date (flood scene) VV and VH backscatter.

In sum, C-band's inability to penetrate the dense oil palm canopy means that the double bounce effect that is characteristic of flooded forests is not observed, therefore it is not possible to detect the presence/absence of standing water except in very young oil palm. In older oil palm, C-band is unable to detect any difference between the backscatter response in flooded and non-flooded conditions. C-band's tendency to saturate early means it is not sensitive to biomass and struggles to differentiate among the different growth stages of oil palm. This is true for all growth stages in non-flooded conditions and for older growth stages in flooded conditions. The presence of flooding improves the ability to identify different growth stages of oil palm, but to a limited extent. While flooded seedling oil palm, and to a lesser extent flooded young

oil palm, may be distinguished from the same growth stage in non-flooded conditions, the wide spectral variance of these classes means their backscatter profiles overlap considerably with other classes. This is because the younger growth stages in flooded conditions generate a complex backscatter return caused by the size of the target relative to the spatial resolution of the data, which produces substantial variability in the backscatter coefficients. What is more, the backscatter spread of all the classes is wide due to the presence of residual speckle noise in the data.

4.2. The sensitivities of the method

The sensitivities of the method to detect the presence/absence of flooding in oil palm stands are determined by the limitations of the data and the strengths and weaknesses of the method.

4.2.1. Limitations of the data

Sentinel-1 SAR data

The limitations of C-band's relatively short wavelength are mentioned previously.

The lack of HH polarisation for the study area is unfortunate as HH is the preferred polarisation for the detection of flooded vegetation (Martinis & Rieke, 2015; Tsyganskaya et al., 2018b) and flood extent (Manjusree et al., 2012; Twele et al., 2016). While both VV and HH polarisations measure surface scattering, the latter detects differences in surface scattering. The vertical polarised wave is more attenuated than the horizontally polarised wave, therefore HH polarisation achieves superior canopy penetration and a stronger reflection when striking the water surface than VV polarisation (Tsyganskaya et al., 2018b). Consequently, HH polarisation contributes more double bounce scattering than VV polarisation (Tsyganskaya et al., 2018b). Similarly, the lack of HV polarisation means less sensitivity towards volume scattering and differences in biomass.

For the detection of flooded forests, incidence angles $< 35°$ are generally more effective than incidence angles $> 35°$ (Hess et al., 1990; Wang et al., 1995; Townsend,

2001). The near- and far-range incidence angles of the C-band data covering the study area are 36.2° and 38.5°, respectively. This small range in incidence angles, combined with the radiometric calibration performed during pre-processing, means that differences in incidence angles will have a negligible effect on the backscatter coefficients. Given the impenetrability of the oil palm canopy to even L-band data, it's doubtful that C-band data with a steeper incidence angle would have markedly improved the transmissivity of the oil palm canopy.

Reference data

In the absence of ground truth data, this study relies extensively on Google Earth imagery to provide reference data for the creation of the oil palm land cover mask and to inform the location of training areas. Manual visual interpretation is time-consuming and monotonous, and errors may occur if operator fatigue sets in. Although every effort is made to ensure an assigned class is unequivocal, it is possible that an incorrect class is assigned to some training areas. This is especially true for the older growth stages where the canopy coverage makes the ground cover less visible and identifying the presence/absence of standing water is less certain than for the younger growth stages. Furthermore, other than the presence/absence of standing water, the spatial resolution of the Google Earth imagery is insufficient for determining the ground surface or ground condition of the oil palm stands, which is important for differentiating growth stages of oil palm, as discussed in the next section.

A three-day time lag exists between the acquisition of the reference data and the flood scene. In the three days that elapsed between the acquisition of the Sentinel-1 scene and the Google Earth scene, just 9.8 mm of rainfall was recorded at the SKMJ weather station in the study area. Consequently, a slight recession in the amount of standing water may have occurred between the acquisition dates of the Sentinel-1 scene and the Google Earth scene, in which case the Google Earth scene would represent a slightly conservative source of reference data. Consequently, if an area appears flooded in the Google Earth scene it is a reasonable assumption that the area is flooded in the Sentinel-1 scene, but if an area appears non-flooded in the Google Earth scene, it is possible that flooding is present in the Sentinel-1 scene but has receded before the acquisition of the Google Earth scene. If a recession in flooding did occur between the

acquisition dates, and if any of the training areas for the non-flooded classes overlap with these areas, it would mean some flooded pixels were present in the training samples of the non-flooded classes.

4.2.2. Weaknesses of the method

The advantages of applying SAR data to the detection of flooded vegetation and flooded forests are outlined in the Introduction. This section focuses on the weaknesses of the method, which largely relate to challenges in the study setting. Some of the challenges are specific to the study area and others are relevant to oil palm environments more generally.

The oil palm's management system has a significant impact on the backscatter response. Oon et al. (2019) used both C-band and L-band data to examine the backscatter intensity of smallholder and industrial plantations. They found that smallholdings exhibited a significantly higher average backscatter intensity than industrial plantations in C-band VV, C-band VH, and L-band HV. They suggested this was due to the multiple tree species that were present in the smallholdings (Oon et al., 2019). They also found that smallholdings in their study area were well-drained with more extensive flood-control waterways than the industrial plantations (Oon et al., 2019). Although Oon et al. (2019) reported a difference in C-band backscatter intensity between oil palm management systems, the findings of Descals et al. (2019) did not corroborate this.

Industrial plantations are characterised by a monoculture management system, a uniform stand age, and a planted area > 50 ha (Oon et al., 2019). In contrast, the management system of smallholdings may be monoculture or polyculture (where the oil palm is intercropped with banana, rubber, cassava, pineapple, and other crops), and the stand age may be uniform or variable (Oon et al., 2019). In addition, smallholdings may feature irregular planting patterns with multiple row orientations occurring within the same parcel, unhealthy trees with stunted growth, and numerous missing trees that reveal large patches of bare soil or vegetation (Oon et al., 2019). Consequently, the ground cover of smallholdings is highly heterogeneous (Gutiérrez-Vélez & DeFries, 2013). These characteristics are a feature of the smallholdings in this study, which

created a problem of fuzzy class boundaries during the extraction of the training samples. Although training samples are not collected from these heterogeneous areas, the number of potential training areas is reduced. Moreover, the diversity of the target features may interfere with the backscatter response and increase the likelihood of errors if an image classification is performed.

In this study, no distinction is made between smallholdings and industrial holdings during the collection of the training samples due to the difficulty in obtaining a sufficient number of training samples for each class. Had a distinction been made, it would contribute valuable information towards understanding the potential differences in the backscatter response from different management systems.

The total backscatter produced from a vegetated surface consists not only of backscatter from the vegetated surface, but also backscatter from the ground cover (some of which is attenuated by the vegetation) and backscatter from ground-vegetation interactions (Vreugdenhil et al., 2018). According to Izzawati (2002), the ground condition varies widely in oil palm plantations, and may consist of swamp, undergrowth, or plantation debris. Furthermore, X-, C-, and L-band are all sensitive to the condition of the ground surface in oil palm plantations and any attempt to differentiate the growth stage of oil palm will be hindered without prior knowledge of the ground conditions (Izzawati, 2002). Other than the presence/absence of standing water, the training samples used in this study do not account for differences in the ground surface so the impact of ground condition on the backscatter observed in this study is unknown.

The pre-processed SAR data used in this study contained residual speckle noise, which contributes to the spread in the backscatter distributions of the classes. Again, the smallholdings presented a challenge for the reduction of speckle. The application of a speckle filter with a window size larger than 5x5 is not feasible as the small size of the smallholder parcels, and the mixed classes within the parcels, would incorporate the backscatter intensity of pixels from other oil palm classes, and from other land cover classes, into the target pixel. Other approaches to reduce speckle, such as averaging multiple SAR images from the same orbit track and applying a multitemporal speckle filter, take advantage of the oil palm's relatively stable phenology throughout the year

(Lazecky et al., 2018). However, this approach is not appropriate for this study as the backscatter intensity on the flood date cannot be averaged with the backscatter intensity of other (non-flooded) dates. Object-based image classification is known to reduce speckle noise as pixels with similar backscatter values are grouped into objects (Tsyganskaya et al., 2018b). However, the fuzzy boundaries of the oil palm classes in the smallholdings makes the creation of reference image objects, which are used during the validation of the segmentation process, challenging and unreliable.

4.2.3. Recommendations for future research

The outcomes of this study strongly lend themselves to further research:

The nature of the smallholder plantations in this study restricted the ability to reduce speckle noise sufficiently. Future studies that exclude smallholdings could test whether a larger speckle filter window or an alternative speckle reduction method can reduce the speckle noise, which would reduce the spectral variance of the classes.

Notwithstanding, research on smallholdings is under-developed. The backscatter intensities of smallholdings and industrial holdings should be differentiated to determine whether a difference in backscatter intensity exists between management systems. This knowledge may improve the separability of flooded and non-flooded oil palm as well as different growth stages of oil palm.

The impact of row orientation on backscatter intensity warrants investigation. This study notes that oil palm is planted in a variety of row orientations, not only in smallholdings, but in industrial plantations also. Row orientations vary both within plantations and between plantations, and the impact on the backscatter response is unknown.

The reliability of reference data could be improved by using actual ground truth data to avoid errors that may arise in the visual interpretation process of optical imagery. This would also provide an opportunity for the condition of the ground surface to be accounted for in the backscatter response. However, this would require field work that coincided with an actual inundation event and there are practical implications for conducting field work in such conditions. Gaining access to a flooded plantation at an

optimal time may be prevented by logistical challenges, such as poor weather, flooded overland routes, and damage to infrastructure. Furthermore, gaining permission to access a plantation, even when flooding is absent, is often challenging.

Incorporating additional data (e.g., L-band backscatter intensity, optical data, texture variables, vegetation indices) to supplement C-band backscatter intensity may improve the detection of flooded oil palm. When combined with C-band backscatter, these data have improved the detection of oil palm land cover, oil palm age, and the type of management system. It is highly likely that their inclusion would improve the detection of flooding in oil palm plantations compared to C-band backscatter alone. In addition, new free and open source SAR data coming online in 2024, such as the NISAR (NASA/Indian Space Research Organization SAR) dual frequency (L- and S-band [λ=12 cm]) fully polarimetric data, and ESA's Biomass mission (P-band) fully polarimetric data, provides additional opportunities to map the extent of flooding in oil palm plantations.

P-band's long wavelength is capable of penetrating even dense forest canopies, and it is expected to be highly effective at identifying the presence/absence of standing water underneath all growth stages of oil palm, including older (closed canopy) growth stages. Furthermore, P-band is sensitive to biomass and should be effective at differentiating the growth stages of oil palm even in non-flooded conditions, which C-band cannot achieve. However, young palms may be completely transparent to P-band, potentially making P-band less suitable for differentiating among the young (open canopy) growth stages of oil palm. In studies where detecting the different growth stages of oil palm is important, supplementing P-band data with shorter wavelength data, such as L-band, may be necessary. However, it may be possible to utilise only P-band backscatter if the desired aim is to map the extent of flooding in an oil palm environment without considering the growth stage of the oil palm.

5. CONCLUSIONS

The backscatter response of all classes was lower in the VH polarisation than in the VV polarisation as the oil palm generated more surface scattering than volume scattering. However, the pattern of the backscatter response was the same in both polarisations.

The unplanted flooded class exhibited very low backscatter and displayed a unique backscatter profile that represented open surface water. In flooded conditions, the backscatter in both polarisations increased with increasing growth stage, however the marginal increase in backscatter diminished with each successive growth stage, and by the adult and mature growth stages the increase in backscatter was minimal. The backscatter coefficients of the seedling and young growth stages displayed a wider dynamic range in flooded conditions than in non-flooded conditions as they formed a mixed target that generated a complex return signal. The backscatter response of the non-flooded classes was similar revealing that the growth stage had little impact on C-band backscatter when flooding was absent. There was a wide spread in the backscatter coefficients of all the classes due to residual speckle noise in the data.

The greatest separation was achieved for a single growth stage of oil palm in flooded and non-flooded conditions when the backscatter of both polarisations was used. The separability of the backscatter distributions in flooded and non-flooded conditions began with high separability in the unplanted and seedling growth stages and rapidly declined with increasing growth stage. By the adult growth stage there was total overlap in the backscatter distributions and no separability between flooded and non-flooded conditions.

The highest separability in the backscatter profiles of the different oil palm growth stages in flooded and non-flooded conditions was achieved by the VV and VH backscatter on the flood date. The backscatter of the derived bands and the standardised backscatter of the timeseries did not improve the separability.

Sentinel-1 C-band VV and VH data is highly effective at identifying flooding in unplanted areas of oil palm plantations and in oil palm seedlings, and it is moderately effective at identifying flooding in young oil palm. It is unable to detect flooding in teen, adult, or mature oil palm.

This study contributed to the following under-developed research areas in the field of remote sensing: the study of inundation in oil palm stands, the study of smallholder plantations, and the study of juvenile/open canopy oil palm. To the best of the author's knowledge, this is the first study to report the backscatter characteristics of flooded oil palm.

6. REFERENCES

Abdikan, S., Sanli, S. B., Ustuner, M., & Calò, F. (2016). Land Cover Mapping Using Sentinel-1 SAR Data. *The International Archives of the Photogrammetry, Remote Sensing and Spatial Information Sciences, Volume XLI-B7, 2016 XXIII ISPRS Congress*. Prague, Czech Republic, 12–19 July 2016.

Abram, N., Xofis, P., Tzanopoulos, J., MacMillan, D., & Ancrenaz, M. (2014). Synergies for Improving Oil Palm Production and Forest Conservation in Floodplain Landscapes. *PLoS ONE, 9*(6), e95388. doi:10.1371/journal.pone.0095388

Abubakar, A., Ishak, M. Y., & Makmom, A. A. (2021). Impacts of and adaptation to climate change on the oil palm in Malaysia: A systematic review. *Environmental Science and Pollution Research, 28*(39), 54339−54361. doi.org/10.1007/s11356-021-15890-3

Adrianto, H. A., Spracklen, D. V., Arnold, S. R., Sitanggang, I. S., & Syaufina, L. (2019). Forest and Land Fires are Mainly Associated with Deforestation in Riau Province, Indonesia. *Remote Sensing, 12*(1), 3, doi:10.3390/rs12010003

Ahamad, M. S. S., Ali, R., Zakaria, N., Ghani, A., & Chang, C. K. (2011). Flood loss assessment of the 2003 Muda river flood. *3rd International Conference on Managing Rivers in the 21st Century: Sustainable Solutions for Global Crisis of Flooding, Pollution and Water Scarcity*. Penang, Malaysia, 6−9 December 2009.

Ballester-Berman, J. D., & Rastoll-Gimenez, M. (2021). Sensitivity Analysis of Sentinel-1 Backscatter to Oil Palm Plantations at Pluriannual Scale: A Case Study in Gabon, Africa. *Remote Sensing, 13*, 2075. doi.org/10.3390/rs13112075

BNPB (*Badan Nasional Penanggulangan Bencana*). (2021). *Data Informasi Bencana Indonesia* (DIBI)/ Indonesia Disaster Data Information. Retrieved December 10, 2021, from http://dibi.bnpb.go.id/

Brown, I. (2004). *The territories of Indonesia*. London: Routledge.

Carlson, K. M., Curran, L. M., Asner, G. P., Pittman, A. M., Trigg, S. N. & Marion Adeney, J. (2013). Carbon emissions from forest conversion by Kalimantan oil palm plantations. *Nature Clim. Change, 3*(3), 283−287. doi:10.1038/NCLIMATE1702

Carolita, I., Darmawan, S., Permana, R., Dirgahayu, D., Wiratmoko, D., Kartika, T., & Arifin, S. (2019). Comparison of Optic Landsat-8 and SAR Sentinel-1 in Oil Palm Monitoring, Case Study: Asahan, North Sumatera, Indonesia. *IOP Conf. Series: Earth and Environmental Science, 280*, 012015. doi:10.1088/1755-1315/280/1/012015

Chain Reaction Research (CRR) (2021). *Indonesian Moratoria: Loopholes, Lack of Sanctions Fail to Stop Palm Oil-Linked Deforestation*. Retrieved May 30, 2022, from https://chainreactionresearch.com/report/indonesian-moratoria-palm-oil-deforestation/

Cheng, Y., Yu, L., Cracknell, A. P., & Gong, P. (2016). Oil palm mapping using Landsat and PALSAR: A case study in Malaysia. *International Journal of Remote Sensing, 37*(22), 5431−5442. doi.org/10.1080/01431161.2016.1241448

Chong, K. L., Kanniah, K. D., Pohl, C., & Tan, K. P. (2017). A review of remote sensing applications for oil palm studies. *Geo-spatial Information Science, 20*(2), 184−200. doi.org/10.1080/10095020.2017.1337317

Clement, M. A., Kilsby, C. G., & Moore, P. (2017). Multi-temporal synthetic aperture radar flood mapping using change detection. *Journal of Flood Risk Management*. doi:10.1111/jfr3.12303

Comeau, L., Hergoualc'h, K., Smith, J., & Verchot, L. (2013). *Conversion of intact peat swamp forest to oil palm plantation: Effects on soil CO2 fluxes in Jambi, Sumatra*. Working Paper 110. Bogor, Indonesia: CIFOR.

Corley, R. H. V. (2009). How much palm oil do we need? *Environmental Science & Policy, 12*(2), 134−139. doi:10.1016/j.envsci.2008.10.011

De Alban, J. D. T., Connette, G. M., Oswald, P., & Webb, E. L. (2018). Combined Landsat and L-band SAR data improves land cover classification and change detection in dynamic tropical landscapes. *Remote Sensing, 10*(2), 306. doi:10.3390/rs10020306

Delacre, M., Lakens, D., & Leys, C. (2017). Why Psychologists Should by Default Use Welch's t-test Instead of Student's t-test. *International Review of Social Psychology, 30*(1), 92–101. doi.org/10.5334/irsp.82

Delacre, M., Leys, C., Mora, Y. L., & Lakens, D. (2019). Taking parametric assumptions seriously: Arguments for the use of Welch's F-test instead of the classical F-test in one-way ANOVA. *International Review of Social Psychology, 32*(1), 13, 1–12. doi.org/10.5334/irsp.198

Descals, A., Szantoi, Z., Meijaard, E., Rindanata, G., & Wich, S. (2019). Oil Palm (*Elaeis guineensis*) Mapping with Details: Smallholder versus Industrial Plantations and their Extent in Riau, Sumatra. *Remote Sensing, 11*, 2590. doi:10.3390/rs11212590

Dislich, C., Keyel, A. C., Salecker, J., Kisel, Y., Meyer, K. M., Auliya, M., Barnes, A. D., Corre, M. D., Darras, K., & Faust, H. (2017). A review of the ecosystem functions in oil palm plantations, using forests as a reference system. *Biological Reviews, 92,* 1539−1569. doi:10.1111/brv.12295

DJP (*Direktorat Jenderal Perkebunan*) (2021). *Statistik Perkebunan Unggulan Nasional* 2019–2021/ Statistical of National Leading Estate Crops Commodity 2019–2021. Retrieved May 24, 2022, from https://ditjenbun.pertanian.go.id/pojok-media/publikasi/

Edwards, R. B., Falcon, W. P., Hadiwidjaja, G., Higgins, M. M., Naylor, R. L., & Sumarto, S. (2020). *Fight Fire with Finance: A Randomized Field Experiment to Curtail Land-Clearing Fire in Indonesia.* TNP2K Working Paper 55-e/2020. Retrieved May 31, 2022, from http://tnp2k.go.id/download/17936WP55%20FightfireR2.pdf

Filipponi, F. (2019). Sentinel-1 GRD Preprocessing Workflow. *Proceedings, 18*, 11. doi:10.3390/ECRS-3-06201

Fitrianto, A. C., Darmawan, A., Tokimatsu, K., & Sufwandika, M. (2018). Estimating the age of oil palm trees using remote sensing technique. *IOP Conf. Series: Earth and Environmental Science, 148,* 012020. doi:10.1088/1755-1315/148/1/012020

Gaveau, D. L. A., Locatelli, B., Salim, M. A., Husnayaen, Manurung, T. Descals, A., Angelsen, A., Meijaard, E., & Sheil, D. (2022) Slowing deforestation in Indonesia follows declining oil palm expansion and lower oil prices. *PLOS ONE 17*(3): e0266178. https://doi.org/10.1371/journal.pone.0266178

Gunarso, P., Hartoyo, M., Agus, F., & Killeen, T. (2013). Oil palm and land use change in Indonesia, Malaysia and Papua New Guinea. *Reports from the Technical Panels of the 2nd greenhouse gas working Group of the Roundtable on Sustainable Palm Oil (RSPO)*.

Gutiérrez-Vélez, V. H., & DeFries, R. (2013). Annual multi-resolution detection of land cover conversion to oil palm in the Peruvian Amazon. *Remote Sensing of Environment, 129*, 154−167. doi.org/10.1016/j.rse.2012.10.033

Hai, T. C., Ng, A., Prudente, C., Pang, C., & Yee, J. T. C. (2001). Balancing the need for sustainable oil palm development and conservation: The Lower Kinabatangan floodplains experience. *ISP National Seminar, 2001: Strategic Directions for the Sustainability of the Oil Palm Industry*. Kota Kinabalu, Sabah, Malaysia, 11−12 June 2001.

Heitmann, E. O., Ji, S., Nie, J., & Breecker, D. O. (2017). Orbitally-paced variations of water availability in the SE Asian Monsoon region following the Miocene Climate Transition. *Earth and Planetary Science Letters*. Advance online publication. doi.org/10.1016/j.epsl.2017.06.006

Henson, I., Harun, M., & Chang, K. (2008). Some observations on the effects of high water tables and flooding on oil palm, and a preliminary model of oil palm water balance and use in the presence of a high water table. *Oil Palm Bulletin, 56,* 14−22.

Hess, L. L., Melack, J. M., & Simonett, D. S. (1990). Radar detection of flooding beneath the forest canopy: A review. *International Journal of Remote Sensing*, *11*(7), 1313−1325.

Hooijer, A., Vernimmen, R., Visser, M., & Mawdsley, N. (2015*). Flooding projections from elevation and subsidence models for oil palm plantations in the Rajang Delta peatlands, Sarawak, Malaysia* (Deltares report 1207384). Retrieved May 24, 2022, from https://www.deltares.nl/app/uploads/2015/06/ Rajang-Delta-Peatland-Subsidence-Flooding-Deltares-2015.pdf

Izzawati. (2002). *The use of a radar backscatter model to assess the sensitivity of multi-frequency, -polarisation and -angle SAR data for detecting the growth stage of oil palm plantations* [Doctoral dissertation, University College London]. UCL Discovery. https://discovery.ucl.ac.uk/id/eprint/10106424/1/The_use_of_a_radar_ backscatter.pdf

Jelsma, I., Schoneveld, G. C., Zoomers, A., & van Westen, A. C. M. (2017). Unpacking Indonesia's independent oil palm smallholders: An actor-disaggregated approach to identifying environmental and social performance challenges. *Land Use Policy, 69,* 281−297. doi.org/10.1016/j.landusepol.2017.08.012

Jensen, J. R. (2005). *Introductory Digital Image Processing: A Remote Sensing Perspective* (3rd ed.). Upper Saddle River, NJ, USA: Pearson Prentice Hall.

Joshi, N., Baumann, M., Ehammer, A., Fensholt, R., Grogan, K., Hostert, P., … & Waske, B. (2016). A Review of the Application of Optical and Radar Remote Sensing Data Fusion to Land Use Mapping and Monitoring. *Remote Sensing, 8*(1), 70. doi:10.3390/rs8010070

Junk, W. J., Bayley, P. B., & Sparks, R. E. (1989). The flood pulse concept in river-floodplain systems. *Canadian Special Publication of Fisheries and Aquatic Sciences, 106*, 110−127.

Kasischke, E. S., Smith, K. B., Bourgeau-Chavez, L. L., Romanowicz, E. A., Brunzell, S., & Richardson, C. J. (2003). Effects of seasonal hydrologic patterns in south Florida wetlands on radar backscatter measured from ERS-2 SAR imagery. *Remote sensing of environment, 88*(4), 423−441. doi:10.1016/j.rse.2003.08.016

Kee, Y. W., Shariff, A. R. M., Sood, A. M., & Nordin, L. (2018). Application of SAR data for oil palm tree discrimination. *IOP Conf. Series: Earth and Environmental Science, 169*, 012065. doi:10.1088/1755-1315/169/1/012065

Kelley, L. C., & Prabowo, A. (2019). Flooding and land use change in Southeast Sulawesi, Indonesia. *Land, 8*(9), 139, doi:10.3390/land8090139

Kellndorfer, J. (2019). Using SAR Data for Mapping Deforestation and Forest Degradation. In: A. I. Flores-Anderson, K. E. Herndon, R. B. Thapa & E. Cherrington (Eds.), *The Synthetic Aperture Radar (SAR) Handbook: Comprehensive Methodologies for Forest Monitoring and Biomass Estimation* (pp. 65−79). NASA. doi:10.25966/68c9-gw82

Koh, L. P., Miettinen, J., Liew, S. C., & Ghazoul, J. (2011). Remotely sensed evidence of tropical peatland conversion to oil palm. *Proceedings of the National Academy of Sciences, 108*(12), 5127−5132. www.pnas.org/cgi/doi/10.1073/pnas.1018776108

Koh, L. P., & Wilcove, D. S. (2008). Is oil palm agriculture really destroying tropical biodiversity? *Conservation Letters, 1*(2), 60−64. doi:10.1111/j.1755-263X.2008.00011.x

Kwoun, O. I., & Lu, Z. (2009). Multi-temporal RADARSAT-1 and ERS backscattering signatures of coastal wetlands in southeastern Louisiana. *Photogrammetric Engineering & Remote Sensing, 75*(5), 607−617.

Lang, M. W., Townsend, P. A., & Kasischke, E. S. (2008). Influence of incidence angle on detecting flooded forests using C-HH synthetic aperture radar data. *Remote sensing of environment, 112*(10), 3898−3907. doi:10.1016/j.rse.2008.06.013

Laurin, G. V., Liesenberg, V., Chen, Q., Guerriero, L., Del Frate, F., Bartolini, A., Coomes, D., Wilebore, B., Lindsell, J., & Valentini, R. (2013). Optical and SAR sensor synergies for forest and land cover mapping in a tropical site in West Africa. *International Journal of Applied Earth Observation and Geoinformation, 21*, 7−16. doi:10.1016/j.jag.2012.08.002

Lazecky, M., Lhota, S., Penaz, T., & Klushina, D. (2018). Application of Sentinel-1 satellite to identify oil palm plantations in Balikpapan Bay. *IOP Conf. Series: Earth and Environmental Science, 169*, 012064. doi:10.1088/1755-1315/169/1/012064

Lee, J. S. (1980). Digital image enhancement and noise filtering by use of local statistics. *IEEE Transactions on Pattern Analysis and Machine Intelligence, 2*, 165–168.

Lee, J.-S., Jurkevich, L., Dewaele, P., Wambacq, P., & Oosterlinck, A. (1994). Speckle filtering of synthetic aperture radar images: A review. *Remote Sensing Reviews, 8*(4), 313−340.

Lee, W. K., & Ong, B. K. (2006). The unseen flood: Waterlogging in large oil palm plantations. *Jurutera*, January, 28−31.

Lee, J. S. H., Wich, S., Widayati, A., & Koh, L. P. (2016). Detecting industrial oil palm plantations on Landsat images with Google Earth Engine. *Remote Sensing Applications: Society and Environment, 4*, 219−224. doi.org/10.1016/j.rsase.2016.11.003

Li, L., Dong, J., Njeudeng Tenku, S., & Xiao, X. (2015). Mapping oil palm plantations in Cameroon using PALSAR 50-m Orthorectified Mosaic images. *Remote Sensing, 7*(2), 1206−1224. doi:10.3390/rs70201206

Loo, Y. Y., Billa, L., & Singh, A. (2015). Effect of climate change on seasonal monsoon in Asia and its impact on the variability of monsoon rainfall in Southeast Asia. *Geoscience Frontiers, 6*(6), 817−823. doi.org/10.1016/j.gsf.2014.02.009

Malaysian Palm Oil Council (MPOC). (2020). *Annual Report 2020*. Retrieved May 6, 2022, from https://mpoc.org.my/annual-report-2020/

Manjusree, P., Kumar, L. P., Bhatt, C. M., Rao, G. S., & Bhanumurthy, V. (2012). Optimization of threshold ranges for rapid flood inundation mapping by evaluating backscatter profiles of high incidence angle SAR images. *International Journal of Disaster Risk Science, 3*(2), 113−122. doi:10.1007/s13753-012-0011-5

Mantel, S., Wösten, H., & Verhagen, J. (2007). *Biophysical land suitability for oil palm in Kalimantan, Indonesia*. Report 2007/01. ISRIC - World Soil Information, Altera, Plant Research International, Wageningen University and Research.

Marti, S. (2008). *Losing ground: The human rights impacts of oil palm plantation expansion in Indonesia*. Friends of the Earth, LifeMosaic & SawitWatch.

Martinis, S., Clandillon, S., Plank, S., Twele, A., Huber, C., Caspard, M., Maxant, J., Cao, W., Haouet, S., & Fuchs, E.-M. (2017). *ASAPTERRA-Advancing SAR and Optical Methods for Rapid Mapping.* Retrieved August 16, 2017, from http://elib.dlr.de/110776/1/ASAPTERRA_FinalReport_2017.pdf

Martinis, S., & Rieke, C. (2015). Backscatter analysis using multi-temporal and multi-frequency SAR data in the context of flood mapping at River Saale, Germany. *Remote Sensing, 7*(6), 7732−7752. doi:10.3390/rs70607732

Merten, J., Stiegler, C., Hennings, N., Purnama, E. S., Röll, A., Agusta, H., … Faust, H. (2020). Flooding and land use change in Jambi Province, Sumatra: Integrating local knowledge and scientific inquiry. *Ecology and Society, 25*(3), 14. doi.org/10.5751/ES-11678-250314

Meyer, F. (2019). Spaceborne Synthetic Aperture Radar: Principles, Data Access, and Basic Processing Techniques. In: A. I. Flores-Anderson, K. E. Herndon, R. B. Thapa & E. Cherrington (Eds.), *The Synthetic Aperture Radar (SAR) Handbook: Comprehensive Methodologies for Forest Monitoring and Biomass Estimation* (pp. 21−43). NASA. doi:10.25966/ez4f-mg98

Miettinen, J., Hooijer, A., Shi, C., Tollenaar, D., Vernimmen, R., Liew, S. C., Malins, C., & Page, S. E. (2012a). Extent of industrial plantations on Southeast Asian peatlands in 2010 with analysis of historical expansion and future projections. *GCB Bioenergy, 4*(6), 908−918. doi:10.1111/j.1757-1707.2012.01172.x

Miettinen, J., Hooijer, A., Tollenaar, D., Page, S., Malins, C., Vernimmen, R., Shi, C., & Liew, S. C. (2012b). *Historical analysis and projection of oil palm plantation expansion on peatland in Southeast Asia*. ICCT White Paper No. 17. Washington, DC: The International Council on Clean Transportation.

Miettinen, J., & Liew, S. C. (2011). Separability of insular Southeast Asian woody plantation species in the 50 m resolution ALOS PALSAR mosaic product. *Remote Sensing Letters, 2*(4), 299−307. doi.org/10.1080/01431161.2010.520345

Miettinen, J., Liew, S. C., & Kwoh, L. K. (2015). Usability of Sentinel-1 Dual Polarization C-Band Data for Plantation Detection in Insular Southeast Asia. *36th Asian Conference on Remote Sensing (ACRS2015): Fostering Resilient Growth in Asia*. Manila, Philippines, October, 2015.

Miettinen, J., Shi, C., & Liew, S. C. (2016). Land cover distribution in the peatlands of Peninsular Malaysia, Sumatra and Borneo in 2015 with changes since 1990. *Global Ecology and Conservation, 6,* 67−78. doi.org/10.1016/j.gecco.2016.02.004

Mohd Najib N. E., Kanniah, K. D., Cracknell, A.P., & Yu, L. (2020). Synergy of Active and Passive Remote Sensing Data for Effective Mapping of Oil Palm Plantation in Malaysia. *Forests, 11*(8), 858. doi.org/10.3390/f11080858

Morel, A. C., Saatchi, S. S., Malhi, Y., Berry, N. J., Banin, L., Burslem, D., Nilus, R., & Ong, R. C. (2011). Estimating aboveground biomass in forest and oil palm plantation in Sabah, Malaysian Borneo using ALOS PALSAR data. *Forest Ecology and Management, 262*(9), 1786−1798. doi:10.1016/j.foreco.2011.07.008

Muhammad, S. A., Ab Kadir, M. O., Rodhi, A. M., & Hassan, H. M. (2017). Variations of $\delta^{13}C$ and $\delta^{15}N$ in oil palm tree organs: An insight into C and N distribution. *J Oil Palm Res, 29*(2), 242−250.

Murphy, D. J. (2014). The future of oil palm as a major global crop: Opportunities and challenges. *Journal of Oil Palm Research, 26*(1), 1−24.

Nawir, A. A., Gunarso, P., Santoso, H., Julmansyah & Hakim, M. R. (2016). *Experiences, lessons and future directions for forest landscape restoration in Indonesia.* Bangkok, Thailand: FAO and RECOFTC.

Nizalapur, V., Jha, C. S., & Madugundu, R. (2010). Estimation of above ground biomass in Indian tropical forested area using multi-frequency DLR-ESAR data. *International Journal of Geomatics and Geosciences, 1*(2), 167–178.

Nomura, K., Mitchard, E. T., Patenaude, G., Bastide, J., Oswald, P., & Nwe, T. (2019). Oil palm concessions in southern Myanmar consist mostly of unconverted forest. *Scientific Reports, 9*(1), 1−9. doi.org/10.1038/s41598-019-48443-3

Noojipady, P., Morton, D. C., Schroeder, W., Carlson, K. M., Huang, C., Gibbs, H. K., … & Prince, S. D. (2017). Managing fire risk during drought: the influence of certification and El Niño on fire-driven forest conversion for oil palm in Southeast Asia. *Earth System Dynamics, 8*(3), 749−771, doi:10.5194/esd-2017-2

Noor, F. M. M., Gassner, A., Terheggen, A., & Dobie, P. (2017). Beyond sustainability criteria and principles in palm oil production: Addressing consumer concerns through insetting. *Ecology and Society, 22*(2). doi.org/10.5751/ES-09172-220205

Nurdiana, A., Setiawan, Y., Pawitan, H., Prasetyo, L. B., & Permatasari, P. A. (2016). Land changes monitoring using MODIS time-series imagery in peat lands areas, Muaro Jambi, Jambi Province, Indonesia. *Procedia Environmental Sciences, 33*, 443−449. doi:10.1016/j.proenv.2016.03.095

Oon, A., Ngo, K. D., Azhar, R., Ashton-Butt, A., Lechner, A. M., & Azhar, B. (2019). Assessment of ALOS-2 PALSAR-2L-band and Sentinel-1 C-band SAR backscatter for discriminating between large-scale oil palm plantations and smallholdings on tropical peatlands. *Remote Sensing Applications: Society and Environment, 13*, 183–190. doi.org/10.1016/j.rsase.2018.11.002

Osaki, M., Nursyamsi, D., Noor, M., Wahyunto & Segah, H. (2016). Peatland in Indonesia. In: M. Osaki & N. Tsuji (Eds.), *Tropical Peatland Ecosystems* (pp. 49−58). Tokyo: Springer Japan. doi:10.1007/978-4-431-55681-7_3

Page, S., Hoscilo, A., Langner, A., Tansey, K., Siegert, F., Limin, S., & Rieley, J. (2009). Chapter 9: Tropical peatland fires in Southeast Asia. In: M. A. Cochrane (Ed.), *Tropical fire ecology: Climate change, land use, and ecosystems dynamics* (pp. 263−287). Berlin, Heidelberg: Springer.

Page, S. E., Morrison, R., Malins, C., Hooijer, A., Rieley, J. O., & Jauhiainen, J. (2011). *Review of peat surface greenhouse gas emissions from oil palm plantations in Southeast Asia*. ICCT White Paper No. 15. Washington, DC: The International Council on Clean Transportation.

Phalan, B., Bertzky, M., Butchart, S. H. M., Donald, P. F., Scharlemann, J. P. W., Stattersfield, A. J., & Balmford, A. (2013). Crop Expansion and Conservation Priorities in Tropical Countries. *PLOS ONE, 8*(1), e51759. doi:10.1371/journal.pone.0051759

Pham-Duc, B., Prigent, C., & Aires, F. (2017). Surface Water Monitoring within Cambodia and the Vietnamese Mekong Delta over a Year, with Sentinel-1 SAR Observations. *Water, 9*(6), 366. doi:10.3390/w9060366

Pirker, J., Mosnier, A., Kraxner, F., Havlík, P., & Obersteiner, M. (2016). What are the limits to oil palm expansion? *Global Environmental Change, 40*, 73−81. doi.org/10.1016/j.gloenvcha.2016.06.007

Pittman, A. M., Carlson, K., Curran, L., & Ponette-Gonzalez, A. (2013). NASA satellite data used to study the impact of oil palm expansion across Indonesian Borneo. *The Earth Observer, 25*(5), 12−15.

Plank, S., Jüssi, M., Martinis, S., & Twele, A. (2017). Mapping of flooded vegetation by means of polarimetric Sentinel-1 and ALOS-2/PALSAR-2 imagery. *International Journal of Remote Sensing, 38(*13), 3831−3850. doi.org/10.1080/01431161.2017.1306143

Pohl, C., Chong, K. L., & van Genderen, J. (2015). Multisensor approach to oil palm plantation monitoring using data fusion and GIS. *36th Asian Conference on Remote Sensing (ACRS2015): Fostering Resilient Growth in Asia*. Manila, Philippines, October, 2015.

Pohl, C., & Loong, C. K. (2016). In-situ data collection for oil palm tree height determination using synthetic aperture radar. *IOP Conf. Series: Earth and Environmental Science, 34*, 012027. doi:10.1088/1755-1315/34/1/012027

Poortinga, A., Tenneson, K., Shapiro, A., Nquyen, Q., San Aung, K., Chishtie, F., & Saah, D. (2019). Mapping plantations in Myanmar by fusing Landsat-8, Sentinel-2 and Sentinel-1 data along with systematic error quantification. *Remote Sensing, 11*(7), 831. doi:10.3390/rs11070831

Rakwatin, P., Longépé, N., Isoguchi, O., Shimada, M., Uryu, Y., & Takeuchi, W. (2012). Using multiscale texture information from ALOS PALSAR to map tropical forest. *International journal of remote sensing, 33*(24), 7727−7746. doi:10.1080/01431161.2012.701349

Ranson, K. J., & Sun, G. (2000). Effects of environmental conditions on boreal forest classification and biomass estimates with SAR. *IEEE Transactions on Geoscience and Remote Sensing, 38*(3), 1242−1252.

Rosenqvist, Å. (1996). Evaluation of JERS-1, ERS-1 and Almaz SAR backscatter for rubber and oil palm stands in West Malaysia. *Remote Sensing, 17*(16), 3219−3231.

Rosenqvist, Å. (2018). *A Layman's Interpretation Guide to L-band and C-band Synthetic Aperture Radar Data*. Retrieved March 13, 2022, from https://ceos.org/ard/files/Laymans_SAR_Interpretation_Guide_2.0.pdf

Rosenqvist, Å., & Oguma, H. (1995). Phenological characteristics of cultivated vegetation covers in JERS-1 and ERS-1 synthetic aperture radar data- Preliminary results. In *International Symposium on Vegetation Monitoring* (pp. 194−198). Chiba, Japan.

Roundtable on Sustainable Palm Oil (RSPO) (2018). *Smallholders Hub*. Retrieved October 1, 2018, from https://rspo.org/

Roundtable on Sustainable Palm Oil (RSPO) (2017). *The challenges of growing oil palm on peatlands*. Retrieved May 30, 2022, from https://rspo.org/news-and-events/news/the-challenges-of-growing-oil-palm-on-peatlands

Roundtable on Sustainable Palm Oil (RSPO) (2019). *The Independent Smallholder Standard*. Retrieved September 23, 2022, from https://rspo.org/resources/smallholders-documents/smallholders-key-documents/rspo-ish-standard-2019

Santos, C., & Messina, J. P. (2008). Multi-sensor data fusion for modeling African palm in the Ecuadorian Amazon. *Photogrammetric Engineering & Remote Sensing, 74*(6), 711−723.

Saragih, B. (2017). Oil palm smallholders in Indonesia: Origin, development strategy and contribution to the national economy. *Presented at the World Plantation Conference*, Jakarta, 18–20 October 2017.

Schlaffer, S., Matgen, P., Hollaus, M., & Wagner, W. (2015). Flood detection from multi-temporal SAR data using harmonic analysis and change detection. *International Journal of Applied Earth Observation and Geoinformation, 38*, 15−24. doi.org/10.1016/j.jag.2014.12.001

Schoneveld, G. C., Ekowati, D., Andrianto, A., & Van Der Haar, S. (2019). Modeling peat-and forestland conversion by oil palm smallholders in Indonesian Borneo. *Environmental Research Letters, 14*(1), 014006, doi.org/10.1088/1748-9326/ab487

Serco Italia SPA. (2018). *Flood Monitoring with Sentinel-1 Using S-1 Toolbox - January 2015, Malawi (version 1.2).* Retrieved March 13, 2022, from https://rus-copernicus.eu/portal/wp-content/uploads/library/education/training/HAZA01_ FloodMapping_Malawi_Tutorial.pdf

Singh, P., & Shree, R. (2016). Analysis and effects of speckle noise in SAR images. In *Advances in Computing, Communication, & Automation (ICACCA) (Fall), International Conference on* (pp. 1−5). IEEE.

Sinha, S., Jeganathan, C., Sharma, L. K., & Nathawat, M. S. (2015). A review of radar remote sensing for biomass estimation. *International Journal of Environmental Science and Technology*, *12*(5), 1779−1792. doi: 10.1007/s13762-015-0750-0

Sumarga, E., Hein, L., Hooijer, A., & Vernimmen, R. (2016). Hydrological and economic effects of oil palm cultivation in Indonesian peatlands. *Ecology and Society, 21*(2), 52. doi.org/10.5751/ES-08490-210252

Tan, K. P., Kanniah, K. D., & Cracknell, A. P. (2013) Use of UK-DMC 2 and ALOS PALSAR for studying the age of oil palm trees in southern peninsular Malaysia. *International Journal of Remote Sensing, 34*(20), 7424–7446. doi.org/10.1080/01431161.2013.822601

Tarigan, S. D. (2016). Land cover change and its impact on flooding frequency of Batanghari Watershed, Jambi Province, Indonesia. *Procedia Environmental Sciences, 33*, 386−392. doi:10.1016/j.proenv.2016.03.089

Tarigan, S., Wiegand, K., & Slamet, B. (2018). Minimum forest cover required for sustainable water flow regulation of a watershed: A case study in Jambi Province, Indonesia. *Hydrology and Earth System Sciences, 22*(1), 581−594. doi.org/10.5194/hess-22-581-2018

Teng, K. C., Koay, J. Y., Tey, S. H., Lim, K. S., Ewe, H. T., & Chuah, H. T. (2015). A Dense Medium Microwave Backscattering Model for the Remote Sensing of Oil Palm. *IEEE Transactions on Geoscience and Remote Sensing, 53*(6), doi:10.1109/TGRS.2014.2372796

Tomarken, A. J., & Serlin, R. C. (1986). Comparison of ANOVA Alternatives Under Variance Heterogeneity and Specific Noncentrality Structures. *Psychological Bulletin, 99*(1), 90−99. doi:10.1037/0033-2909.99.1.90

Torbick, N., Ledoux, L., Salas, W., & Zhao, M. (2016). Regional Mapping of Plantation Extent Using Multisensor Imagery. *Remote Sensing, 8*(3), 236. doi:10.3390/rs8030236

Townsend, P. A. (2001). Mapping seasonal flooding in forested wetlands using multi-temporal Radarsat SAR. *Photogrammetric Engineering and Remote Sensing, 67*(7), 857−864.

Tsyganskaya, V., Martinis, S., Marzahn, P., & Ludwig, R. (2018a). Detection of Temporary Flooded Vegetation Using Sentinel-1 Time Series Data. *Remote Sensing, 10*(8), 1286. doi.org/10.3390/rs10081286

Tsyganskaya, V., Martinis, S., Marzahn, P., & Ludwig, R. (2018b). SAR-based detection of flooded vegetation – a review of characteristics and approaches. *International Journal of Remote Sensing, 39*(8), 2255−2293. doi.org/10.1080/01431161.2017.1420938

Twele, A., Cao, W., Plank, S., & Martinis, S. (2016). Sentinel-1-based flood mapping: A fully automated processing chain. *International Journal of Remote Sensing, 37*(13), 2990−3004. doi:10.1080/01431161.2016.1192304

United States Department of Agriculture (USDA) (2015). *Malaysia: 2014/15 Palm oil production affected by flooding*. Retrieved July 22, 2017, from https://pecad.fas.usda.gov/

United States Department of Agriculture (USDA) (2012). *Malaysia: Stagnating Palm Oil Yields Impede Growth*. Retrieved July 22, 2017, from https://pecad.fas.usda.gov/

United States Department of Agriculture (USDA) (2022). *Oilseeds: World markets and trade*. Retrieved May 6, 2022, from https://apps.fas.usda.gov/psdonline/circulars/oilseeds.pdf

Vijay, V., Pimm, S. L., Jenkins, C. N., & Smith, S. J. (2016). The Impacts of Oil Palm on Recent Deforestation and Biodiversity Loss. *PLOS ONE, 11*(7), e0159668. doi:10.1371/journal.pone.0159668

Wang, Y., Hess, L. L., Filoso, S., & Melack, J. M. (1995). Understanding the radar backscattering from flooded and nonflooded Amazonian forests: Results from canopy backscatter modeling. *Remote Sensing of Environment, 54*(3), 324−332.

Warren, M., Hergoualc'h, K., Kauffman, J. B., Murdiyarso, D., & Kolka, R. (2017). An appraisal of Indonesia's immense peat carbon stock using national peatland maps: Uncertainties and potential losses from conversion. *Carbon Balance and Management, 12*(1), 12. doi:10.1186/s13021-017-0080-2

Wilusz, D. C., Zaitchik, B. F., Anderson, M. C., Hain, C. R., Yilmaz, M. T., & Mladenova, I. E. (2017). Monthly flooded area classification using low resolution SAR imagery in the Sudd wetland from 2007 to 2011. *Remote Sensing of Environment, 194*, 205−218. doi.org/10.1016/j.rse.2017.03.005

Woittiez, L. S., van Wijk, M. T., Slingerland, M., van Noordwijk, M., & Giller, K. E. (2017). Yield gaps in oil palm: A quantitative review of contributing factors. *European Journal of Agronomy, 83*, 57−77. doi.org/10.1016/j.eja.2016.11.002

Wösten, H., Hooijer, A., Siderius, C., Rais, D. S., Idris, A., & Rieley, J. (2006a). Tropical peatland water management modelling of the Air Hitam Laut catchment in Indonesia. *International Journal of River Basin Management, 4*(4), 233−244. doi:10.1080/15715124.2006.9635293

Wösten, J., Van Den Berg, J., Van Eijk, P., Gevers, G., Giesen, W., Hooijer, A., Idris, A., Leenman, P., Rais, D. S., & Siderius, C. (2006b). Interrelationships between hydrology and ecology in fire degraded tropical peat swamp forests. *Water Resources Development, 22*(1), 157−174. doi:10.1080/07900620500405973

Xu, K., Qian, J., Hu, Z., Duan, Z., Chen, C., Liu, J., … & Xing, X. (2021). A New Machine Learning Approach in Detecting the Oil Palm Plantations Using Remote Sensing Data. *Remote Sensing, 13*(2), 236. doi.org/10.3390/rs13020236

Yamamoto, E. M. S., Sayama, T., Yamamoto, K., & Apip (2021). Mapping of Mature and Young Oil Palm Distributions in a Humid Tropical River Basin for Flood Vulnerability Assessment. *IOP Conf. Series: Earth and Environmental Science, 789*(1). 012034. doi:10.1088/1755-1315/789/1/012034

Yayusman, L. F., & Nagasawa, R. (2015). ALOS-Sensor data integration for the detection of smallholder's oil palm plantation in Southern Sumatra, Indonesia. *Journal of the Japanese Agricultural Systems Society, 31(*2), 27−40.

APPENDICES

Appendix A

A.1. Scattering mechanisms of flooded vegetation

This section provides an overview of the backscatter mechanisms that are common to flooded vegetation, and the characteristics of the sensor and the target that govern them.

A.1.1. Backscatter mechanisms

In an SAR image, dark areas are produced by a low backscatter return (the signal is reflected away from the antenna) while bright areas represent a high backscatter return (the signal is reflected towards the antenna). Natural scenes generate three main types of backscatter: surface, volume, and double bounce (Meyer, 2019).

Surface scattering comprises direct, forward (specular), and diffuse scattering. In direct scattering, a surface that is orientated perpendicular to the SAR antenna reflects the SAR signal directly back to the antenna (Rosenqvist, 2018). Forward or specular scattering occurs when a surface that appears smooth relative to the signal's wavelength (such as calm water, or at longer wavelengths, smooth bare soil) reflects the signal away from the antenna (Rosenqvist, 2018). Diffuse scattering occurs when a surface that appears rough relative to the wavelength (such as choppy water or a ploughed field) scatters the signal in different directions, including towards the antenna (Rosenqvist, 2018).

Volume scattering occurs when the signal bounces multiple times within a 3-dimensional structure, such as a plant canopy, before a portion is reflected towards the antenna (Rosenqvist, 2018).

Double bounce scattering occurs when a corner reflector is created from the perpendicular orientation of a vertical target (such plant stems and tree trunks) and a flat ground or water surface. When the specular reflection off water interacts with

emerging tree trunks it generates a strong corner reflector and a particularly high return signal (Clement et al., 2017).

Open surface water is easily distinguishable in SAR imagery as it is a specular reflector of microwave energy, thus it generates low backscatter and appears dark in the image (Schlaffer et al., 2015). The backscatter from dry land increases with soil moisture and is generally higher than that of open surface water while the backscatter from flooded vegetation is higher still due to the double bounce effect (Wilusz et al., 2017).

However, the pattern of increasing backscatter from open surface water to dry land to flooded vegetation is not always observed due to several factors that influence the backscatter return (Wilusz et al., 2017). Sensor characteristics (i.e., wavelength, polarisation, incidence angle) and environmental factors (e.g., plant type, plant phenology, soil moisture) exert a strong influence on the SAR signal and complicate the interpretation of SAR imagery (Tsyganskaya et al., 2018b).

A.1.2. Sensor characteristics

Wavelength

The wavelength of the SAR signal governs its sensitivity to different targets. Objects that are the same size or larger than the wavelength of the signal are generally visible, while objects that are considerably smaller than the wavelength of the signal are generally invisible (although small objects may still contribute to signal attenuation) (Rosenqvist, 2018). At longer wavelengths, small objects like leaves and twigs appear transparent enabling the signal to penetrate deeper into the canopy and interact with larger objects, such as the trunk and branches, and potentially the ground surface or water surface also (Rosenqvist, 2018).

For this reason, L-band (λ=23.6 cm) is highly effective at detecting water underneath forested canopies as it generates a stronger double bounce effect than C-band (λ=5.6 cm) and X-band (λ=3.1 cm) (Martinis et al., 2017; Plank et al., 2017). Shorter wavelengths exhibit greater canopy attenuation, volume scattering and surface

scattering from the canopy, which reduces the backscatter ratio between flooded and non-flooded forests (Martinis et al., 2017).

Yet the relationship between a signal's wavelength and its sensitivity to different targets is moderated by certain target characteristics. For example, C-band and even X-band can be used for mapping flooded vegetation depending on the type, density, and structure of the canopy, such as in sparse forests and in leaf-off conditions (Martinis et al., 2017; Plank et al., 2017). In fact, in sparsely vegetated areas, C-band may outperform L-band in detecting flooded vegetation by achieving a higher return signal (Tsyganskaya et al., 2018b). Sparse vegetation may be too transparent to L-band to achieve an interaction between the signal and the water surface and vegetation (Tsyganskaya et al., 2018b). (See Section A.1.3. for additional information on target characteristics.)

Polarisation

Polarisation is "the orientation of the plane of oscillation of a propagating signal" (Meyer, 2019, p. 27). Most SAR sensors today transmit and receive at horizontal and/or vertical linear polarisation (Meyer, 2019). Co-polarised sensors operate in HH (horizontal transmit, horizontal receive) or VV (vertical transmit, vertical receive) polarisation, while cross-polarised sensors operate in HV (horizontal transmit, vertical receive) or VH (vertical transmit, horizontal receive) polarisation (Meyer, 2019). Modern sensors tend to operate in dual-polarisation mode (HH and VV; HH and HV; VV and VH) or quad-polarisation mode (HH, VV, HV, VH) (Tsyganskaya et al., 2018b).

The polarisation influences the interaction of the signal with the target. The polarisations are sensitive to different scattering mechanisms and the backscatter does not occur equally in the different polarisations (Meyer, 2019). In general, the relative scattering strength of the polarisations is as follows (Meyer, 2019):

Surface scattering:	$S_{VV} > S_{HH} > S_{HV}$ or S_{VH}
Volume scattering:	Main source of S_{HV} and S_{VH}
Double bounce scattering:	$S_{HH} > S_{VV} > S_{HV}$ or S_{VH}

where 'S' is the scattering power (Meyer, 2019).

Of the surface scattering sub-types, direct scattering appears bright in the co-polarised channels, forward (specular) scattering appears dark in both co- and cross-polarised channels, while the amount of backscatter received from diffuse scattering increases in the co-polarised channels as surface roughness increases (Rosenqvist, 2018). In volume scattering, the random orientation of the scattering surfaces within a 3-dimensional structure means the polarisation of the return signal is random and the backscatter is received equally in co- and cross-polarisations (Rosenqvist, 2018). When a signal is reflected from a vertical target the direction of the polarisation remains unchanged, therefore in double bounce scattering the return signal is co-polarised (Rosenqvist, 2018). Consequently, co-polarised backscatter is associated with measuring surface scattering and double bounce scattering, while cross-polarised backscatter is associated with measuring volume scattering (Tsyganskaya et al., 2018b; Kellndorfer, 2019).

An increase in polarisation complexity generates different scattering mechanisms that help discriminate among vegetation types and environmental conditions, but it comes at a loss in spatial resolution (Tsyganskaya et al., 2018b). Co-polarisations are generally more effective at detecting flooded forests than cross-polarisations as cross-polarisations generate very low backscatter (Martinis et al., 2017), and in sparsely vegetated areas cross-polarisations can lead to the misclassification of sparse vegetation as water (Manjusree et al., 2012; Twele et al., 2016). HH is widely considered more effective than VV for detecting flooded forests as HH is more sensitive to the double bounce effect (Tsyganskaya et al., 2018b). Compared to VV, HH penetrates further into the canopy and generates a stronger reflection from a water surface (Tsyganskaya et al., 2018b). However, as the backscatter coefficients of the different polarisations contribute different information, the detection of flooded vegetation is usually enhanced when a combination of co- and cross-polarisation backscatter is used (Abdikan et al., 2016; Pham-Duc et al., 2017; Tsyganskaya et al., 2018b).

Incidence angle

The incidence angle is “the angle between the radar signal and an imaginary line perpendicular to the Earth's surface” (Lang et al., 2008, p. 3898). The incidence angle of the SAR signal varies by sensor and may range from 10° (steep) to 65° (shallow)

(Tsyganskaya et al., 2018b). Incidence angle exerts a strong influence on backscatter (Kellndorfer, 2019). Shallower incidence angles increase the interaction between the signal and the crown layer in a forest canopy, producing more volume scattering (Martinis et al., 2017; Tsyganskaya et al., 2018b). At steeper incidence angles the signal has a shorter pathway through the crown layer, which increases the transmissivity of the canopy and the double bounce effect (Martinis and Rieke, 2015; Tsyganskaya et al., 2018b). However, this pattern is not universally observed and the influence of incidence angle on backscatter depends on the density and structure of the forest as this determines the amount of attenuation and volume scattering by the canopy (Hess et al., 1990; Townsend, 2001; Lang et al., 2008).

In sum, assuming all other sensor characteristics are equal, the ratio of backscatter between forests in flooded and non-flooded conditions is higher for longer wavelengths (L-band) than shorter wavelengths (C- and X-band), higher for co-polarisations than cross-polarisations, higher for HH polarisation than VV polarisation, and higher for small incidence angles than large incidence angles (Wang et al., 1995). Nonetheless, L-band HH data can be difficult and/or expensive to acquire. Of the currently active SAR systems that record L-band (ALOS-2) and C-band data (Sentinel-1 and Radarsat-2) for commercial applications, only Sentinel-1 is a free and open data source. Although Sentinel-1 HH and HV data are available for polar regions, only VV and VH data are available for most observation zones.

A.1.3. Target characteristics

Since the characteristics of an SAR sensor are usually stable, variations in backscatter over time stem from changes in the target characteristics, particularly moisture content, surface roughness, and structure (Kellndorfer, 2019).

Oil palms possess an umbrella-like crown of large fronds that radiate out from the top of a single straight trunk (Rosenqvist & Oguma, 1995; Rosenqvist, 1996) (**Error! Reference source not found.**). The fronds reach a width of 2 m and a length of 5–8 m, and comprise an oblong stem made up of numerous long slender pinnate leaflets (Rosenqvist, 1996). A single frond has a leaf area of 6–7 m2 totalling 150–200 m2 per palm (Rosenqvist, 1996). Oil palms grow to a total height of 12–16 m and as the palm

grows, old fronds are removed leaving behind a very rough scale-like trunk (Rosenqvist, 1996). The ground cover consists of grass, legumes and, in older stands, mounds of dead fronds (Rosenqvist, 1996). The planting density is 120–150 palms per hectare in commercial plantations (Woittiez et al., 2017). Palms are felled and replanted once productivity declines at around 20–25 years of age (Rosenqvist, 1996).

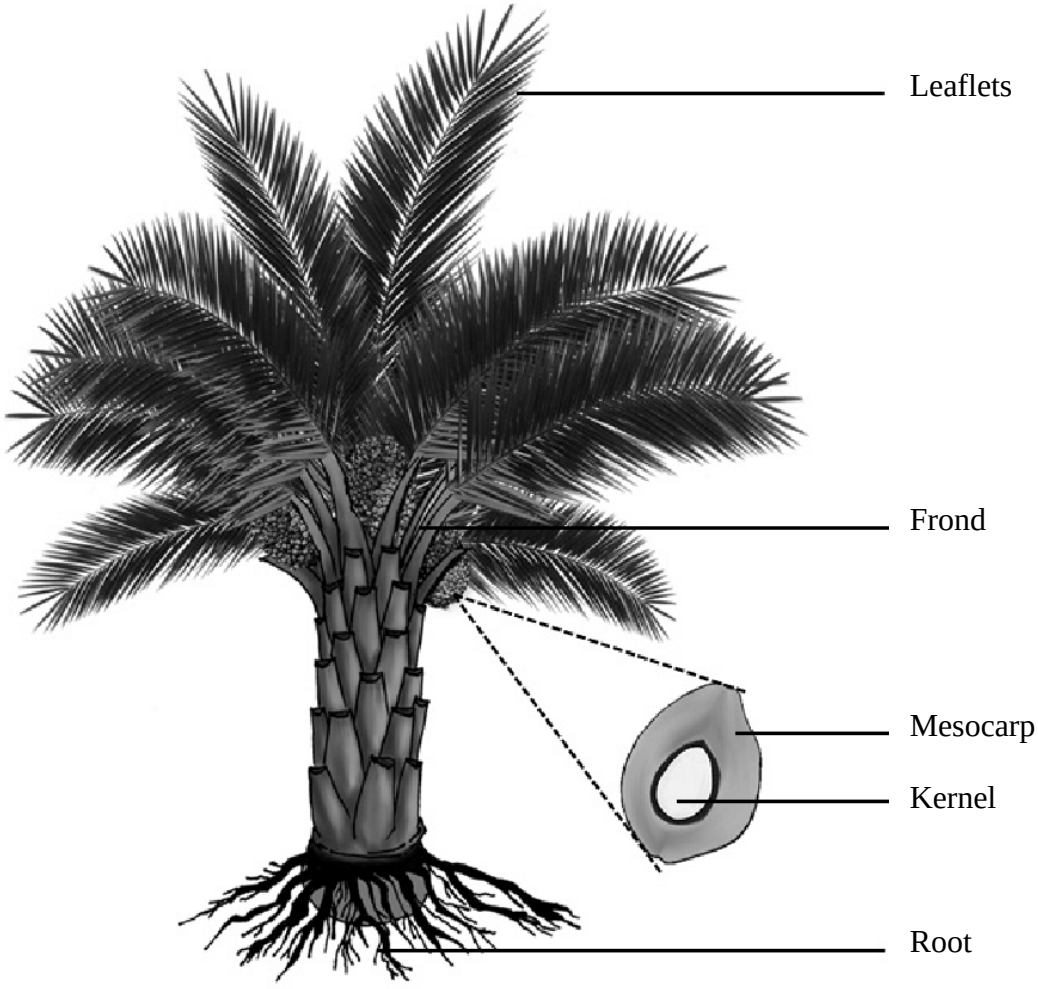

Image credit: Muhammad et al. (2017)

Figure A1: Anatomy of an oil palm tree.

The SAR signal is highly sensitive to moisture, including soil moisture, vegetation moisture, standing open water, and standing water under canopies (Kellndorfer, 2019). The dielectric constant is a measure of material's electric properties. It governs the interaction between the signal and a target material, including how much of the signal scatters at the surface, penetrates the material, or is absorbed by the material (Meyer, 2019). With respect to microwave energy, the dielectric constant of most natural

materials on Earth in dry conditions is between 3 and 8, while water has a dielectric constant of 80. Changes in the water content of a material causes significant changes in the dielectric constant. An increase in the moisture content of soil or vegetation results in reduced penetration and a stronger backscatter return. In general, moist objects appear bright while dry objects appear dark. (Open surface water is an exception: it appears dark because the smooth surface acts as a specular reflector of microwave energy. When the surface is roughened by wind or movement, open water surfaces generate a stronger return signal and appear brighter in SAR imagery, particularly at shorter wavelengths [Kellndorfer, 2019]).

As soil moisture increases in non-flooded forests, the backscatter ratio between forests under flooded and non-flooded conditions decreases (Wang et al., 1995). Backscatter increases with increasing soil moisture regardless of the biomass level so long as transmissivity of the biomass is possible (i.e., the saturation point has not been reached) (Kasischke et al., 2003; Tsyganskaya et al., 2018b). If soil moisture is low, the interaction of the signal with the vegetation and the ground surface generates multiple scatterings, which attenuate the signal and decrease the return signal to the antenna (Kwoun & Lu, 2009). Conversely, if soil moisture is high, the backscatter return is increased as the high dielectric constant of water diminishes the transmission of the signal (Kwoun & Lu, 2009).

Surface roughness is associated with a higher backscatter return as rough surfaces exhibit diffuse scattering and return some of the signal to the antenna. In contrast, smooth surfaces produce forward scattering and reflect the signal away from the antenna. Forest canopies are rough surfaces that appear moderately bright (grey) in SAR imagery. The ‘roughness’ of a surface is relative, and the same surface can generate different backscatter depending on the wavelength and the incidence angle. If two surfaces have an equivalent surface roughness, the surface with the lower moisture content will appear darker.

The importance of the vegetation biomass is discussed in the Introduction section. The biomass of the crown and trunk, coupled with the vertical structure (trunk, branches, leaves) and horizontal structure (planting pattern, planting density) of the vegetation, determines the size, orientation, and distribution of the scattering surfaces within a forest canopy (Oon et al., 2019).

Appendix B

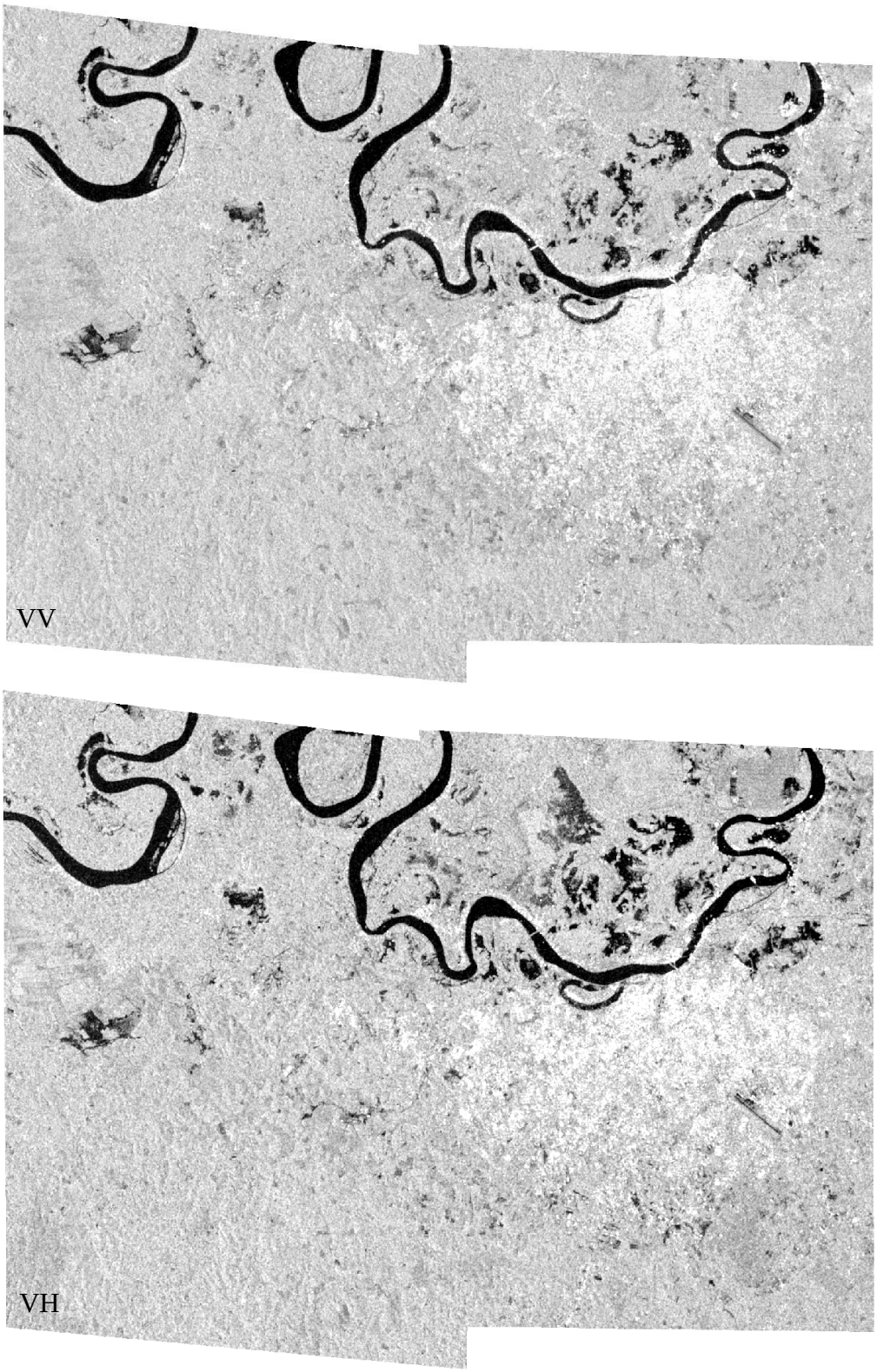

Figure B1: Sentinel-1 C-band VV and VH backscatter (in dB) recorded in the study area on the flood date.

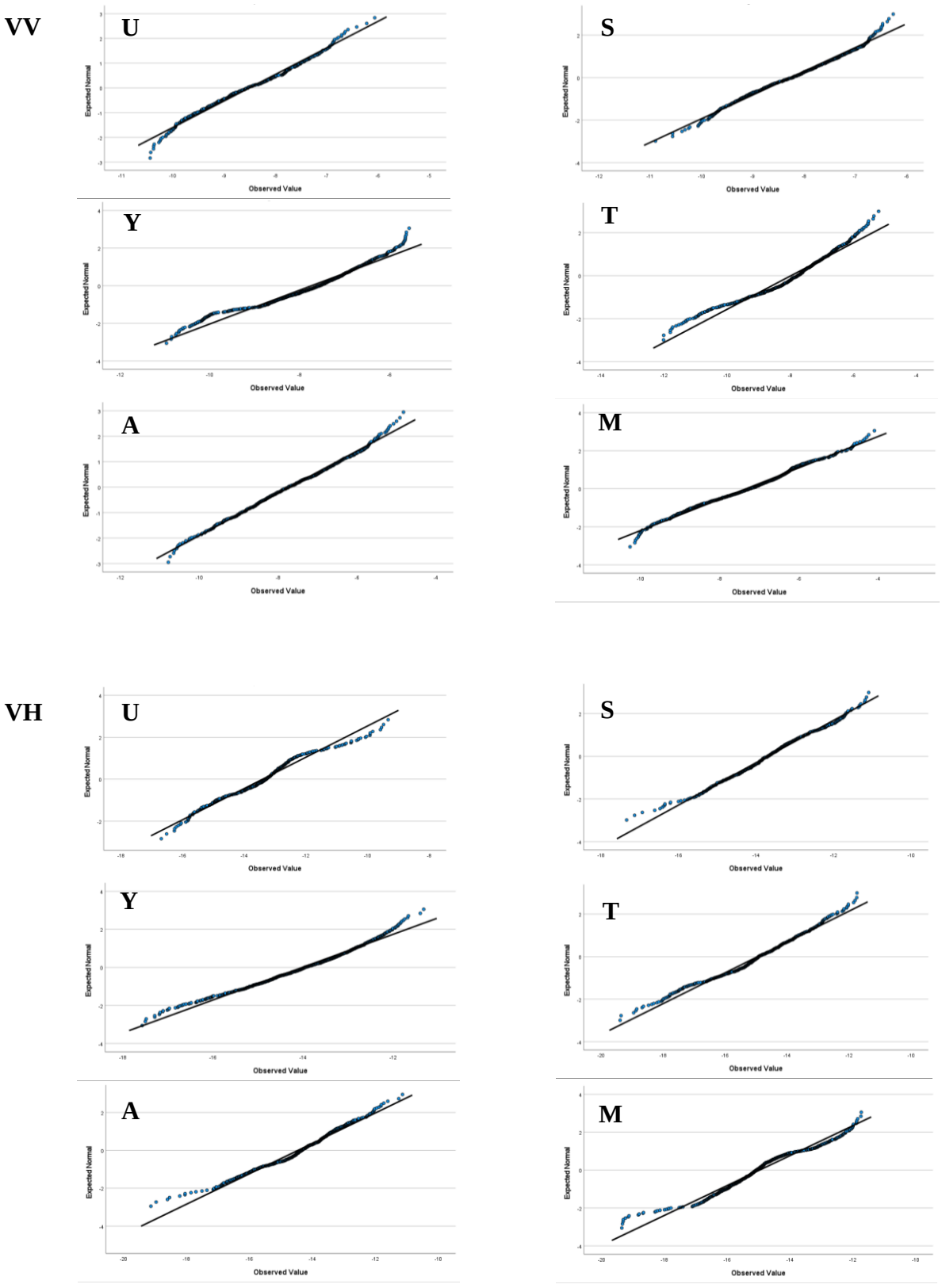

Figure B2: SPSS output of the Normal Q-Q Plot of VV and VH backscatter for the non-flooded classes: unplanted (U), seedling (S), young (Y), teen (T), adult (A), mature (M).

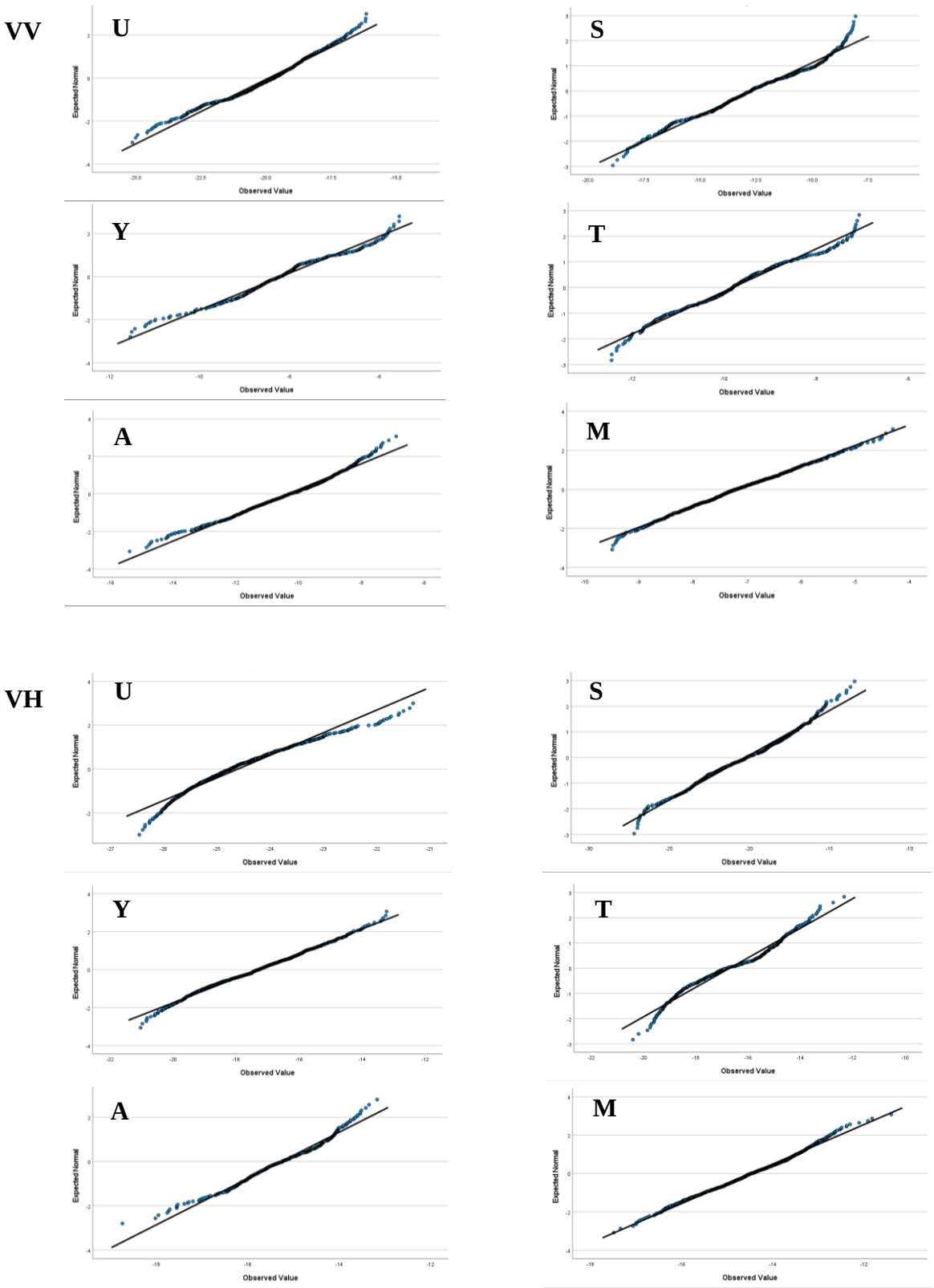

Figure B3: SPSS output of the Normal Q-Q Plot of VV and VH backscatter for the flooded classes: unplanted (U), seedling (S), young (Y), teen (T), adult (A), mature (M).

Table B1: Transformed Divergence scores quantifying the spectral separability between classes[8] in VV polarisation and VH polarisation.

VV

	UNF	**UF**	**SNF**	**SF**	**YNF**	**YF**	**TNF**	**TF**	**ANF**	**AF**	**MNF**	**MF**
UNF	0	2000	15	1532	140	589	108	313	156	64	312	419
UF	2000	0	2000	1684	2000	1977	2000	1997	2000	2000	2000	2000
SNF	15	2000	0	1641	86	739	83	444	105	52	239	315
SF	1532	1684	1641	0	1528	395	1284	801	1461	1279	1528	1776
YNF	140	2000	86	1528	0	785	17	583	2	32	38	83
YF	589	1977	739	395	785	0	580	69	747	530	898	1178
TNF	108	2000	83	1284	17	580	0	425	13	6	64	152
TF	313	1997	444	801	583	69	425	0	568	359	748	980
ANF	156	2000	105	1461	2	747	13	568	0	30	27	79
AF	64	2000	52	1279	32	530	6	359	30	0	106	206
MNF	312	2000	239	1528	38	898	64	748	27	106	0	25
MF	419	2000	315	1776	83	1178	152	980	79	206	25	0

VH

	UNF	**UF**	**SNF**	**SF**	**YNF**	**YF**	**TNF**	**TF**	**ANF**	**AF**	**MNF**	**MF**
UNF	0	2000	47	1691	60	1127	271	869	154	549	318	259
UF	2000	0	2000	1714	2000	1982	2000	1990	2000	2000	2000	2000
SNF	47	2000	0	1864	19	1263	256	1006	112	458	285	141
SF	1691	1714	1864	0	1741	542	1370	604	1583	1638	1438	1815
YNF	60	2000	19	1741	0	1035	134	773	38	304	156	70
YF	1127	1982	1263	542	1035	0	530	32	773	595	542	987
TNF	271	2000	256	1370	134	530	0	318	31	60	3	78
TF	869	1990	1006	604	773	32	318	0	526	386	330	726
ANF	154	2000	112	1583	38	773	31	526	0	134	41	27
AF	549	2000	458	1638	304	595	60	386	134	0	36	127
MNF	318	2000	285	1438	156	542	3	330	41	36	0	74
MF	259	2000	141	1815	70	987	78	726	27	127	74	0

[8] The classes are abbreviated as follows: ‘NF’ = non-flooded; ‘F’ = flooded; ‘U’ = unplanted; ‘S’ = seedling; ‘Y’ = young; ‘T’ = teen; ‘A’ = adult; ‘M’ = mature.

Table B2: Transformed Divergence scores quantifying the spectral separability between classes[9] in both polarisations together (VV and VH).

	UNF	**UF**	**SNF**	**SF**	**YNF**	**YF**	**TNF**	**TF**	**ANF**	**AF**	**MNF**	**MF**
UNF	0	2000	71	1877	297	1274	466	936	367	739	653	736
UF	2000	0	2000	1950	2000	1999	2000	2000	2000	2000	2000	2000
SNF	71	2000	0	1946	143	1399	383	1090	255	580	566	527
SF	1877	1950	1946	0	1815	584	1559	898	1782	1712	1828	1948
YNF	297	2000	143	1815	0	1139	154	897	69	320	312	221
YF	1274	1999	1399	584	1139	0	719	88	1022	740	1100	1413
TNF	466	2000	383	1559	154	719	0	521	40	65	104	199
TF	936	2000	1090	898	897	88	521	0	779	553	896	1199
ANF	367	2000	255	1782	69	1022	40	779	0	156	91	110
AF	739	2000	580	1712	320	740	65	553	156	0	179	263
MNF	653	2000	566	1828	312	1100	104	896	91	179	0	106
MF	736	2000	527	1948	221	1413	199	1199	110	263	106	0

[9] The classes are abbreviated as follows: ‘NF’ = non-flooded; ‘F’ = flooded; ‘U’ = unplanted; ‘S’ = seedling; ‘Y’ = young; ‘T’ = teen; ‘A’ = adult; ‘M’ = mature.

Table B3: Backscatter characteristics of the oil palm classes in VV polarisation and VH polarisation (in dB).

VV	Class	Min.	Max.	Mean	Std. Dev.
	Unplanted flooded	-25.13	-16.15	-19.90	1.66
	Unplanted non-flooded	-10.44	-6.06	-8.51	0.93
	Seedling flooded	-18.89	-8.06	-12.68	2.40
	Seedling non-flooded	-10.90	-6.26	-8.26	0.90
	Young flooded	-15.39	-6.88	-10.33	1.46
	Young non-flooded	-10.97	-5.56	-7.74	1.11
	Teen flooded	-12.44	-7.05	-9.81	1.21
	Teen non-flooded	-12.01	-5.19	-7.97	1.30
	Adult flooded	-11.54	-5.54	-8.18	1.17
	Adult non-flooded	-10.78	-4.82	-7.71	1.20
	Mature flooded	-9.49	-4.30	-7.15	0.95
	Mature non-flooded	-10.27	-4.09	-7.33	1.21

VH	Class	Min.	Max.	Mean	Std. Dev.
	Unplanted flooded	-26.46	-21.31	-24.61	0.97
	Unplanted non-flooded	-16.69	-9.33	-13.40	1.34
	Seedling flooded	-27.18	-13.42	-20.24	2.87
	Seedling non-flooded	-17.34	-11.09	-13.69	1.01
	Young flooded	-21.03	-13.22	-17.30	1.54
	Young non-flooded	-17.57	-11.32	-14.01	1.16
	Teen flooded	-20.41	-12.33	-16.71	1.71
	Teen non-flooded	-19.38	-11.74	-14.95	1.38
	Adult flooded	-18.74	-13.17	-15.26	0.96
	Adult non-flooded	-19.13	-11.13	-14.45	1.25
	Mature flooded	-17.49	-11.40	-14.48	0.97
	Mature non-flooded	-19.35	-11.73	-14.96	1.27

Series from Lund University

Department of Physical Geography and Ecosystem Science

Master Thesis in Geographical Information Science

1. *Anthony Lawther:* The application of GIS-based binary logistic regression for slope failure susceptibility mapping in the Western Grampian Mountains, Scotland (2008).
2. *Rickard Hansen:* Daily mobility in Grenoble Metropolitan Region, France. Applied GIS methods in time geographical research (2008).
3. *Emil Bayramov:* Environmental monitoring of bio-restoration activities using GIS and Remote Sensing (2009).
4. *Rafael Villarreal Pacheco:* Applications of Geographic Information Systems as an analytical and visualization tool for mass real estate valuation: a case study of Fontibon District, Bogota, Columbia (2009).
5. *Siri Oestreich Waage:* a case study of route solving for oversized transport: The use of GIS functionalities in transport of transformers, as part of maintaining a reliable power infrastructure (2010).
6. *Edgar Pimiento:* Shallow landslide susceptibility – Modelling and validation (2010).
7. *Martina Schäfer:* Near real-time mapping of floodwater mosquito breeding sites using aerial photographs (2010).
8. *August Pieter van Waarden-Nagel:* Land use evaluation to assess the outcome of the programme of rehabilitation measures for the river Rhine in the Netherlands (2010).
9. *Samira Muhammad:* Development and implementation of air quality data mart for Ontario, Canada: A case study of air quality in Ontario using OLAP tool. (2010).
10. *Fredros Oketch Okumu*: Using remotely sensed data to explore spatial and temporal relationships between photosynthetic productivity of vegetation and malaria transmission intensities in selected parts of Africa (2011).
11. *Svajunas Plunge:* Advanced decision support methods for solving diffuse water pollution problems (2011).
12. *Jonathan Higgins:* Monitoring urban growth in greater Lagos: A case study using GIS to monitor the urban growth of Lagos 1990 - 2008 and produce future growth prospects for the city (2011).

13. *Mårten Karlberg:* Mobile Map Client API: Design and Implementation for Android (2011).
14. *Jeanette McBride:* Mapping Chicago area urban tree canopy using color infrared imagery (2011).
15. *Andrew Farina:* Exploring the relationship between land surface temperature and vegetation abundance for urban heat island mitigation in Seville, Spain (2011).
16. *David Kanyari*: Nairobi City Journey Planner: An online and a Mobile Application (2011).
17. *Laura V. Drews:* Multi-criteria GIS analysis for siting of small wind power plants - A case study from Berlin (2012).
18. *Qaisar Nadeem:* Best living neighborhood in the city - A GIS based multi criteria evaluation of ArRiyadh City (2012).
19. *Ahmed Mohamed El Saeid Mustafa:* Development of a photo voltaic building rooftop integration analysis tool for GIS for Dokki District, Cairo, Egypt (2012).
20. *Daniel Patrick Taylor*: Eastern Oyster Aquaculture: Estuarine Remediation via Site Suitability and Spatially Explicit Carrying Capacity Modeling in Virginia's Chesapeake Bay (2013).
21. *Angeleta Oveta Wilson:* A Participatory GIS approach to *unearthing* Manchester's Cultural Heritage '*gold mine'* (2013).
22. *Ola Svensson:* Visibility and Tholos Tombs in the Messenian Landscape: A Comparative Case Study of the Pylian Hinterlands and the Soulima Valley (2013).
23. *Monika Ogden:* Land use impact on water quality in two river systems in South Africa (2013).
24. *Stefan Rova:* A GIS based approach assessing phosphorus load impact on Lake Flaten in Salem, Sweden (2013).
25. *Yann Buhot:* Analysis of the history of landscape changes over a period of 200 years. How can we predict past landscape pattern scenario and the impact on habitat diversity? (2013).
26. *Christina Fotiou:* Evaluating habitat suitability and spectral heterogeneity models to predict weed species presence (2014).
27. *Inese Linuza:* Accuracy Assessment in Glacier Change Analysis (2014).
28. *Agnieszka Griffin:* Domestic energy consumption and social living standards: a GIS analysis within the Greater London Authority area (2014).

29. *Brynja Guðmundsdóttir:* Detection of potential arable land with remote sensing and GIS - A Case Study for Kjósarhreppur (2014).

30. *Oleksandr Nekrasov:* Processing of MODIS Vegetation Indices for analysis of agricultural droughts in the southern Ukraine between the years 2000-2012 (2014).

31. *Sarah Tressel:* Recommendations for a polar Earth science portal in the context of Arctic Spatial Data Infrastructure (2014).

32. *Caroline Gevaert:* Combining Hyperspectral UAV and Multispectral Formosat-2 Imagery for Precision Agriculture Applications (2014).

33. *Salem Jamal-Uddeen:* Using GeoTools to implement the multi-criteria evaluation analysis - weighted linear combination model (2014).

34. *Samanah Seyedi-Shandiz:* Schematic representation of geographical railway network at the Swedish Transport Administration (2014).

35. *Kazi Masel Ullah:* Urban Land-use planning using Geographical Information System and analytical hierarchy process: case study Dhaka City (2014).

36. *Alexia Chang-Wailing Spitteler:* Development of a web application based on MCDA and GIS for the decision support of river and floodplain rehabilitation projects (2014).

37. *Alessandro De Martino:* Geographic accessibility analysis and evaluation of potential changes to the public transportation system in the City of Milan (2014).

38. *Alireza Mollasalehi:* GIS Based Modelling for Fuel Reduction Using Controlled Burn in Australia. Case Study: Logan City, QLD (2015).

39. *Negin A. Sanati:* Chronic Kidney Disease Mortality in Costa Rica; Geographical Distribution, Spatial Analysis and Non-traditional Risk Factors (2015).

40. *Karen McIntyre:* Benthic mapping of the Bluefields Bay fish sanctuary, Jamaica (2015).

41. *Kees van Duijvendijk:* Feasibility of a low-cost weather sensor network for agricultural purposes: A preliminary assessment (2015).

42. *Sebastian Andersson Hylander:* Evaluation of cultural ecosystem services using GIS (2015).

43. *Deborah Bowyer:* Measuring Urban Growth, Urban Form and Accessibility as Indicators of Urban Sprawl in Hamilton, New Zealand (2015).

44. *Stefan Arvidsson:* Relationship between tree species composition and phenology extracted from satellite data in Swedish forests (2015).

45. *Damián Giménez Cruz*: GIS-based optimal localisation of beekeeping in rural Kenya (2016).

46. *Alejandra Narváez Vallejo:* Can the introduction of the topographic indices in LPJ-GUESS improve the spatial representation of environmental variables? (2016).

47. *Anna Lundgren:* Development of a method for mapping the highest coastline in Sweden using breaklines extracted from high resolution digital elevation models (2016).

48. *Oluwatomi Esther Adejoro:* Does location also matter? A spatial analysis of social achievements of young South Australians (2016).

49. *Hristo Dobrev Tomov:* Automated temporal NDVI analysis over the Middle East for the period 1982 - 2010 (2016).

50. *Vincent Muller:* Impact of Security Context on Mobile Clinic Activities A GIS Multi Criteria Evaluation based on an MSF Humanitarian Mission in Cameroon (2016).

51. *Gezahagn Negash Seboka:* Spatial Assessment of NDVI as an Indicator of Desertification in Ethiopia using Remote Sensing and GIS (2016).

52. *Holly Buhler:* Evaluation of Interfacility Medical Transport Journey Times in Southeastern British Columbia. (2016).

53. *Lars Ole Grottenberg*: Assessing the ability to share spatial data between emergency management organisations in the High North (2016).

54. *Sean Grant:* The Right Tree in the Right Place: Using GIS to Maximize the Net Benefits from Urban Forests (2016).

55. *Irshad Jamal:* Multi-Criteria GIS Analysis for School Site Selection in Gorno-Badakhshan Autonomous Oblast, Tajikistan (2016).

56. *Fulgencio Sanmartín:* Wisdom-volkano: A novel tool based on open GIS and time-series visualization to analyse and share volcanic data (2016).

57. *Nezha Acil:* Remote sensing-based monitoring of snow cover dynamics and its influence on vegetation growth in the Middle Atlas Mountains (2016).

58. *Julia Hjalmarsson:* A Weighty Issue: Estimation of Fire Size with Geographically Weighted Logistic Regression (2016).

59. *Mathewos Tamiru Amato:* Using multi-criteria evaluation and GIS for chronic food and nutrition insecurity indicators analysis in Ethiopia (2016).

60. *Karim Alaa El Din Mohamed Soliman El Attar:* Bicycling Suitability in Downtown, Cairo, Egypt (2016).

61. *Gilbert Akol Echelai:* Asset Management: Integrating GIS as a Decision Support Tool in Meter Management in National Water and Sewerage Corporation (2016).

62. *Terje Slinning:* Analytic comparison of multibeam echo soundings (2016).

63. *Gréta Hlín Sveinsdóttir:* GIS-based MCDA for decision support: A framework for wind farm siting in Iceland (2017).

64. *Jonas Sjögren:* Consequences of a flood in Kristianstad, Sweden: A GIS-based analysis of impacts on important societal functions (2017).

65. *Nadine Raska:* 3D geologic subsurface modelling within the Mackenzie Plain, Northwest Territories, Canada (2017).

66. *Panagiotis Symeonidis*: Study of spatial and temporal variation of atmospheric optical parameters and their relation with PM 2.5 concentration over Europe using GIS technologies (2017).

67. *Michaela Bobeck:* A GIS-based Multi-Criteria Decision Analysis of Wind Farm Site Suitability in New South Wales, Australia, from a Sustainable Development Perspective (2017).

68. *Raghdaa Eissa*: Developing a GIS Model for the Assessment of Outdoor Recreational Facilities in New Cities Case Study: Tenth of Ramadan City, Egypt (2017).

69. *Zahra Khais Shahid*: Biofuel plantations and isoprene emissions in Svea and Götaland (2017).

70. *Mirza Amir Liaquat Baig*: Using geographical information systems in epidemiology: Mapping and analyzing occurrence of diarrhea in urban - residential area of Islamabad, Pakistan (2017).

71. *Joakim Jörwall*: Quantitative model of Present and Future well-being in the EU-28: A spatial Multi-Criteria Evaluation of socioeconomic and climatic comfort factors (2017).

72. *Elin Haettner*: Energy Poverty in the Dublin Region: Modelling Geographies of Risk (2017).

73. *Harry Eriksson*: Geochemistry of stream plants and its statistical relations to soil- and bedrock geology, slope directions and till geochemistry. A GIS-analysis of small catchments in northern Sweden (2017).

74. *Daniel Gardevärn:* PPGIS and Public meetings – An evaluation of public participation methods for urban planning (2017).

75. *Kim Friberg:* Sensitivity Analysis and Calibration of Multi Energy Balance Land Surface Model Parameters (2017).

76. *Viktor Svanerud:* Taking the bus to the park? A study of accessibility to green areas in Gothenburg through different modes of transport (2017).

77. *Lisa-Gaye Greene*: Deadly Designs: The Impact of Road Design on Road Crash Patterns along Jamaica's North Coast Highway (2017).

78. *Katarina Jemec Parker*: Spatial and temporal analysis of fecal indicator bacteria concentrations in beach water in San Diego, California (2017).

79. *Angela Kabiru*: An Exploratory Study of Middle Stone Age and Later Stone Age Site Locations in Kenya's Central Rift Valley Using Landscape Analysis: A GIS Approach (2017).

80. *Kristean Björkmann*: Subjective Well-Being and Environment: A GIS-Based Analysis (2018).

81. *Williams Erhunmonmen Ojo*: Measuring spatial accessibility to healthcare for people living with HIV-AIDS in southern Nigeria (2018).

82. *Daniel Assefa*: Developing Data Extraction and Dynamic Data Visualization (Styling) Modules for Web GIS Risk Assessment System (WGRAS). (2018).

83. *Adela Nistora*: Inundation scenarios in a changing climate: assessing potential impacts of sea-level rise on the coast of South-East England (2018).

84. *Marc Seliger*: Thirsty landscapes - Investigating growing irrigation water consumption and potential conservation measures within Utah's largest master-planned community: Daybreak (2018).

85. *Luka Jovičić*: Spatial Data Harmonisation in Regional Context in Accordance with INSPIRE Implementing Rules (2018).

86. *Christina Kourdounouli*: Analysis of Urban Ecosystem Condition Indicators for the Large Urban Zones and City Cores in EU (2018).

87. *Jeremy Azzopardi*: Effect of distance measures and feature representations on distance-based accessibility measures (2018).

88. *Patrick Kabatha*: An open source web GIS tool for analysis and visualization of elephant GPS telemetry data, alongside environmental and anthropogenic variables (2018).

89. *Richard Alphonce Giliba*: Effects of Climate Change on Potential Geographical Distribution of Prunus africana (African cherry) in the Eastern Arc Mountain Forests of Tanzania (2018).

90. *Eiður Kristinn Eiðsson*: Transformation and linking of authoritative multi-scale geodata for the Semantic Web: A case study of Swedish national building data sets (2018).

91. *Niamh Harty*: HOP!: a PGIS and citizen science approach to monitoring the condition of upland paths (2018).

92. *José Estuardo Jara Alvear*: Solar photovoltaic potential to complement hydropower in Ecuador: A GIS-based framework of analysis (2018).

93. *Brendan O'Neill*: Multicriteria Site Suitability for Algal Biofuel Production Facilities (2018).

94. *Roman Spataru*: Spatial-temporal GIS analysis in public health – a case study of polio disease (2018).

95. *Alicja Miodońska*: Assessing evolution of ice caps in Suðurland, Iceland, in years 1986 - 2014, using multispectral satellite imagery (2019).

96. *Dennis Lindell Schettini*: A Spatial Analysis of Homicide Crime's Distribution and Association with Deprivation in Stockholm Between 2010-2017 (2019).

97. *Damiano Vesentini*: The Po Delta Biosphere Reserve: Management challenges and priorities deriving from anthropogenic pressure and sea level rise (2019).

98. *Emilie Arnesten*: Impacts of future sea level rise and high water on roads, railways and environmental objects: a GIS analysis of the potential effects of increasing sea levels and highest projected high water in Scania, Sweden (2019).

99. *Syed Muhammad Amir Raza*: Comparison of geospatial support in RDF stores: Evaluation for ICOS Carbon Portal metadata (2019).

100. *Hemin Tofiq*: Investigating the accuracy of Digital Elevation Models from UAV images in areas with low contrast: A sandy beach as a case study (2019).

101. *Evangelos Vafeiadis*: Exploring the distribution of accessibility by public transport using spatial analysis. A case study for retail concentrations and public hospitals in Athens (2019).

102. *Milan Sekulic*: Multi-Criteria GIS modelling for optimal alignment of roadway by-passes in the Tlokweng Planning Area, Botswana (2019).

103. *Ingrid Piirisaar*: A multi-criteria GIS analysis for siting of utility-scale photovoltaic solar plants in county Kilkenny, Ireland (2019).

104. *Nigel Fox*: Plant phenology and climate change: possible effect on the onset of various wild plant species' first flowering day in the UK (2019).

105. *Gunnar Hesch*: Linking conflict events and cropland development in Afghanistan, 2001 to 2011, using MODIS land cover data and Uppsala Conflict Data Programme (2019).

106. *Elijah Njoku*: Analysis of spatial-temporal pattern of Land Surface Temperature (LST) due to NDVI and elevation in Ilorin, Nigeria (2019).

107. *Katalin Bunyevácz*: Development of a GIS methodology to evaluate informal urban green areas for inclusion in a community governance program (2019).

108. *Paul dos Santos*: Automating synthetic trip data generation for an agent-based simulation of urban mobility (2019).

109. *Robert O' Dwyer*: Land cover changes in Southern Sweden from the mid-Holocene to present day: Insights for ecosystem service assessments (2019).

110. *Daniel Klingmyr*: Global scale patterns and trends in tropospheric NO2 concentrations (2019).

111. *Marwa Farouk Elkabbany*: Sea Level Rise Vulnerability Assessment for Abu Dhabi, United Arab Emirates (2019).

112. *Jip Jan van Zoonen*: Aspects of Error Quantification and Evaluation in Digital Elevation Models for Glacier Surfaces (2020).

113. *Georgios Efthymiou*: The use of bicycles in a mid-sized city – benefits and obstacles identified using a questionnaire and GIS (2020).

114. *Haruna Olayiwola Jimoh*: Assessment of Urban Sprawl in MOWE/IBAFO Axis of Ogun State using GIS Capabilities (2020).

115. *Nikolaos Barmpas Zachariadis*: Development of an iOS, Augmented Reality for disaster management (2020).

116. *Ida Storm*: ICOS Atmospheric Stations: Spatial Characterization of CO2 Footprint Areas and Evaluating the Uncertainties of Modelled CO2 Concentrations (2020).

117. *Alon Zuta*: Evaluation of water stress mapping methods in vineyards using airborne thermal imaging (2020).

118. *Marcus Eriksson*: Evaluating structural landscape development in the municipality Upplands-Bro, using landscape metrics indices (2020).

119. *Ane Rahbek Vierø*: Connectivity for Cyclists? A Network Analysis of Copenhagen's Bike Lanes (2020).

120. *Cecilia Baggini*: Changes in habitat suitability for three declining Anatidae species in saltmarshes on the Mersey estuary, North-West England (2020).

121. *Bakrad Balabanian*: Transportation and Its Effect on Student Performance (2020).

122. *Ali Al Farid*: Knowledge and Data Driven Approaches for Hydrocarbon Microseepage Characterizations: An Application of Satellite Remote Sensing (2020).

123. *Bartlomiej Kolodziejczyk*: Distribution Modelling of Gene Drive-Modified Mosquitoes and Their Effects on Wild Populations (2020).

124. *Alexis Cazorla*: Decreasing organic nitrogen concentrations in European water bodies - links to organic carbon trends and land cover (2020).

125. *Kharid Mwakoba*: Remote sensing analysis of land cover/use conditions of community-based wildlife conservation areas in Tanzania (2021).

126. *Chinatsu Endo*: Remote Sensing Based Pre-Season Yellow Rust Early Warning in Oromia, Ethiopia (2021).

127. *Berit Mohr*: Using remote sensing and land abandonment as a proxy for long-term human out-migration. A Case Study: Al-Hassakeh Governorate, Syria (2021).

128. *Kanchana Nirmali Bandaranayake*: Considering future precipitation in delineation locations for water storage systems - Case study Sri Lanka (2021).

129. *Emma Bylund*: Dynamics of net primary production and food availability in the aftermath of the 2004 and 2007 desert locust outbreaks in Niger and Yemen (2021).

130. *Shawn Pace*: Urban infrastructure inundation risk from permanent sea-level rise scenarios in London (UK), Bangkok (Thailand) and Mumbai (India): A comparative analysis (2021).

131. *Oskar Evert Johansson*: The hydrodynamic impacts of Estuarine Oyster reefs, and the application of drone technology to this study (2021).

132. *Pritam Kumarsingh*: A Case Study to develop and test GIS/SDSS methods to assess the production capacity of a Cocoa Site in Trinidad and Tobago (2021).

133. *Muhammad Imran Khan*: Property Tax Mapping and Assessment using GIS (2021).

134. *Domna Kanari*: Mining geosocial data from Flickr to explore tourism patterns: The case study of Athens (2021).

135. *Mona Tykesson Klubien*: Livestock-MRSA in Danish pig farms (2021).

136. *Ove Njøten*: Comparing radar satellites. Use of Sentinel-1 leads to an increase in oil spill alerts in Norwegian waters (2021).

137. *Panagiotis Patrinos*: Change of heating fuel consumption patterns produced by the economic crisis in Greece (2021).

138. *Lukasz Langowski*: Assessing the suitability of using Sentinel-1A SAR multi-temporal imagery to detect fallow periods between rice crops (2021).

139. *Jonas Tillman*: Perception accuracy and user acceptance of legend designs for opacity data mapping in GIS (2022).

140. *Gabriela Olekszyk*: ALS (Airborne LIDAR) accuracy: Can potential low data quality of ground points be modelled/detected? Case study of 2016 LIDAR capture over Auckland, New Zealand (2022).

141. *Luke Aspland*: Weights of Evidence Predictive Modelling in Archaeology (2022).

142. *Luís Fareleira Gomes*: The influence of climate, population density, tree species and land cover on fire pattern in mainland Portugal (2022).

143. *Andreas Eriksson*: Mapping Fire Salamander (Salamandra salamandra) Habitat Suitability in Baden-Württemberg with Multi-Temporal Sentinel-1 and Sentinel-2 Imagery (2022).

144. *Lisbet Hougaard Baklid*: Geographical expansion rate of a brown bear population in Fennoscandia and the factors explaining the directional variations (2022).

145. *Victoria Persson*: Mussels in deep water with climate change: Spatial distribution of mussel (Mytilus galloprovincialis) growth offshore in the French Mediterranean with respect to climate change scenario RCP 8.5 Long Term and Integrated Multi-Trophic Aquaculture (IMTA) using Dynamic Energy Budget (DEB) modelling (2022).

146. *Benjamin Bernard Fabien Gérard Borgeais*: Implementing a multi-criteria GIS analysis and predictive modelling to locate Upper Palaeolithic decorated caves in the Périgord noir, France (2022).

147. *Bernat Dorado-Guerrero*: Assessing the impact of post-fire restoration interventions using spectral vegetation indices: A case study in El Bruc, Spain (2022).

148. *Ignatius Gabriel Aloysius Maria Perera*: The Influence of Natural Radon Occurrence on the Severity of the COVID-19 Pandemic in Germany: A Spatial Analysis (2022).

149. *Mark Overton*: An Analysis of Spatially-enabled Mobile Decision Support Systems in a Collaborative Decision-Making Environment (2022).

150. *Viggo Lunde*: Analysing methods for visualizing time-series datasets in open-source web mapping (2022).

151. *Johan Viscarra Hansson*: Distribution Analysis of Impatiens glandulifera in Kronoberg County and a Pest Risk Map for Alvesta Municipality (2022).

152. *Vincenzo Poppiti*: GIS and Tourism: Developing strategies for new touristic flows after the Covid-19 pandemic (2022).

153. *Henrik Hagelin*: Wildfire growth modelling in Sweden - A suitability assessment of available data (2023).

154. *Gabriel Romeo Ferriols Pavico*: Where there is road, there is fire (influence): An exploratory study on the influence of roads in the spatial patterns of Swedish wildfires of 2018 (2023).

155. *Colin Robert Potter*: Using a GIS to enable an economic, land use and energy output comparison between small wind powered turbines and large-scale wind farms: the case of Oslo, Norway (2023).

156. *Krystyna Muszel*: Impact of Sea Surface Temperature and Salinity on Phytoplankton blooms phenology in the North Sea (2023).

157. *Tobias Rydlinge*: Urban tree canopy mapping - an open source deep learning approach (2023).

158. *Albert Wellendorf*: Multi-scale Bark Beetle Predictions Using Machine Learning (2023).

159. *Manolis Papadakis*: Use of Satellite Remote Sensing for Detecting Archaeological Features: An Example from Ancient Corinth, Greece (2023).

160. *Konstantinos Sourlamtas*: Developing a Geographical Information System for a water and sewer network, for monitoring, identification and leak repair - Case study: Municipal Water Company of Naoussa, Greece (2023).

161. *Xiaoming Wang*: Identification of restoration hotspots in landscape-scale green infrastructure planning based on model-predicted connectivity forest (2023).

162. *Sarah Sienaert*: Usability of Sentinel-1 C-band VV and VH SAR data for the detection of flooded oil palm (2023).